

CHARACTERIZING THE REDUCTION OF  $\text{Ni}_x\text{Mg}_{1-x}\text{Al}_2\text{O}_4$

BY

BRENDEN E. HILL

A THESIS

SUBMITTED TO THE FACULTY OF

ALFRED UNIVERSITY

IN PARTIAL FULFILLMENT OF THE REQUIREMENTS  
FOR THE DEGREE OF

DOCTOR OF PHILOSOPHY

IN

CERAMICS

ALFRED, NEW YORK

APRIL, 2012

Alfred University theses are copyright protected and may be used for education or personal research only. Reproduction or distribution in any format is prohibited without written permission from the author.

CHARACTERIZING THE REDUCTION OF  $\text{Ni}_x\text{Mg}_{1-x}\text{Al}_2\text{O}_4$

BY

BRENDEN E. HILL

B.S. ALFRED UNIVERSITY (2008)

SIGNATURE OF AUTHOR \_\_\_\_\_

APPROVED BY \_\_\_\_\_ (Signature on File)  
SCOTT T. MISTURE, ADVISOR

\_\_\_\_\_  
(Signature on File)  
STEVEN M. PILGRIM, ADVISORY COMMITTEE

\_\_\_\_\_  
(Signature on File)  
MATTHEW M. HALL, ADVISORY COMMITTEE

\_\_\_\_\_  
(Signature on File)  
NATHAN P. MELLOTT, ADVISORY COMMITTEE

\_\_\_\_\_  
(Signature on File)  
CHAIR, ORAL THESIS DEFENSE

ACCEPTED BY \_\_\_\_\_ (Signature on File)  
DOREEN D. EDWARDS, DEAN  
KAZUO INAMORI SCHOOL OF ENGINEERING

ACCEPTED BY \_\_\_\_\_ (Signature on File)  
NANCY J. EVANGELISTA, ASSOCIATE PROVOST  
FOR GRADUATE AND PROFESSIONAL PROGRAMS  
ALFRED UNIVERSITY

## ACKNOWLEDGMENTS

First I have to thank my parents, Mike and Jeanne Hill, who taught me the importance of creativity, education, and hard work. Second, I have to thank my wife, without whose support and encouragement, I never would have started my Ph.D, much less finished it. She earned her Master's degree while supporting me, working a full time job, and carrying my beautiful daughter. Next I have to thank Izzy, who wasn't around for most of my Ph.D, but she is a constant reminder of why I worked so hard. It was so hard to leave her every morning, but there can't be a better reward after a long day of writing than seeing her excited to see me.

Next, I want to thank the graduate students of Alfred University, who form a wonderful community, both academically and socially. I have to single out for thanks Michelene Hall, Eric Nichols, Mark Naylor, Matt Brophy, and Victoria Blair. They all provided much needed help in the particulars of techniques and equipment, but more importantly in how to think about and present research.

I also need to thank the technical specialists at Alfred, Swavek Zdieszynski, Terry Guild, and Fran Williams, all of whom have done an impeccable job at keeping the instruments I needed to do my research working, and taught me how to use them as well. I also want to thank my committee members, Steven Pilgrim, Matt Hall, and Nathan Mellott, whose questions led to a much better final product than I would have produced without them.

I also need to thank Dr. Vadim Guliants, Dr. Jane Howe, Dr. Ashfia Huq, Dr. Andreas Jentys, and Dr. Sven Vogel for their expertise in performing measurements outside Alfred University.

Acknowledgements for the use of the Hitachi TEM and LV-SEM follow: This research was supported in part by Oak Ridge National Laboratory's SHaRE User Facility, which is sponsored by the Scientific User Facilities Division, Office of Basic Energy Sciences, U.S. Department of Energy. Part of this research was conducted at the Center for Nanophase Materials Sciences, which is sponsored at Oak Ridge National Laboratory by the Division of Scientific User Facilities, U.S. Department of Energy.

Finally I want to thank my advisor, Scott Misture. He allowed me great freedom in determining the direction of my project, and that freedom made the results that I achieved very gratifying. At the same time, he consistently pushed me to work toward a deeper understanding.

Alfred has been a great home to me; nearly all of my friends have been made in Alfred, and I am extremely happy to have spent my last eight years here.

# TABLE OF CONTENTS

	<b>Page</b>
Acknowledgments .....	iii
Table of Contents.....	iv
List of Tables.....	vi
List of Figures.....	vii
Abstract .....	xiii
<b>INTRODUCTION.....</b>	<b>1</b>
A. The Importance of Spinel.....	1
B. Properties of Spinel.....	1
C. Spinel Structure.....	2
D. NiAl <sub>2</sub> O <sub>4</sub> - MgAl <sub>2</sub> O <sub>4</sub> .....	6
E. Non-Stoichiometric Spinel.....	7
F. Reduction Process.....	8
G. Nucleation, Growth, Diffusion.....	11
H. Addition of Zirconia .....	12
I. Metastable Phases Based on the Spinel Structure .....	12
J. Transition Aluminas.....	15
K. Connection Between Metastable Spinel and the Transition Aluminas.....	16
L. Nickel Crystallite Shape.....	16
<b>EXPERIMENTAL PROCEDURE.....</b>	<b>17</b>
A. Spinel Synthesis.....	17
B. Closed System Reduction .....	17
C. Isothermal TGA/DTA.....	19
D. Nonisothermal TGA/DTA .....	21
E. Helium Pycnometry .....	22
F. Room Temperature X-ray Diffraction.....	23
G. High Temperature X-ray Diffraction in Flowing 4% H <sub>2</sub> /N <sub>2</sub> .....	23
H. Rietveld Refinement with TOPAS .....	24
1. Ni <sub>x</sub> Mg <sub>1-x</sub> Al <sub>2</sub> O <sub>4</sub> Model .....	25
2. Nickel Metal Model .....	30
3. Zirconia Models.....	31

I.	Standard Voltage Scanning Electron Microscopy .....	32
J.	Low Voltage Scanning Electron Microscopy .....	32
K.	TEM.....	32
L.	Powder Cross Sections.....	33
<b>RESULTS AND DISCUSSION .....</b>		<b>34</b>
A.	Rietveld Refinement of X-ray Diffraction Data .....	34
B.	High Temperature X-ray Diffraction – $\text{Ni}_x\text{Mg}_{1-x}\text{Al}_2\text{O}_4$ .....	59
C.	High Temperature X-ray Diffraction – $\text{NiAl}_2\text{O}_4$ + Additives .....	64
D.	Isothermal TGA/DTA .....	68
E.	Nonisothermal TGA/DTA Experiments Motivation .....	71
F.	Nonisothermal TGA Experiments.....	73
G.	Verification of Refined Nickel Phase Fraction by TGA.....	76
H.	Spinel Density .....	77
I.	X-Ray Diffraction of TGA-Reduced Samples .....	82
J.	$(\text{Ni,Mg})\text{O}\cdot x\text{Al}_2\text{O}_3$ Phase Stability .....	87
K.	Spinel Surfaces .....	91
L.	Nickel Crystallite Size, Shape and Distribution .....	105
1.	Nickel Particle Distribution.....	105
2.	Refined and Observed Nickel Crystallite Sizes, and Crystallite Shape .....	108
3.	Needle-Like Particles in the Interior of Grains .....	110
M.	Suggestions for Assessing Extent of Reduction .....	115
<b>SUMMARY AND CONCLUSIONS .....</b>		<b>117</b>
<b>FUTURE WORK .....</b>		<b>119</b>
<b>REFERENCES.....</b>		<b>121</b>
<b>APPENDIX 1 – REFINED STRUCTURAL PARAMETERS .....</b>		<b>126</b>
<b>APPENDIX 2 - REMNANT SPINEL COMPOSITIONS USED IN FIGURE 59 ..</b>		<b>134</b>

## LIST OF TABLES

	<b>Page</b>
Table I. Structural Parameters of the Solid Solution Endmembers.....	6
Table II. Structural Parameters of the Metastable Nickel Spinel Phases .....	14
Table III. Dwell Times Used for Each Reduction Temperature .....	18
Table IV. Occupancy Constraints Used in the Refinement of $\text{Ni}_x\text{Mg}_{1-x}\text{Al}_2\text{O}_4$ .....	29
Table V. Starting Structural Parameters Used in the $\text{ZrO}_2$ Models .....	32
Table VI. Closed System Reduction Observed Phase Stability .....	36
Table VII. Comparison of Observed and Refined Nickel Crystallite Sizes .....	110
Table VIII. Reduction Temperatures as a Fraction of the Homologous Melting Temperature of $\text{NiAl}_2\text{O}_4$ .....	110

## LIST OF FIGURES

	<b>Page</b>
Figure 1. Spinel unit cell viewed along the [010] and [100] .....	3
Figure 2. Perspective image of the spinel structure showing the edge-sharing nature of the octahedral sites and the isolated nature of the tetrahedral .....	4
Figure 3. Heating programs used in the nonisothermal TGA measurements. He was flowing until the end of the dwell, 20 ml/min 4% H <sub>2</sub> /Ar. ....	22
Figure 4. Illustration of the allowed combinations of nickel and aluminum per formula unit for each spinel composition. ....	27
Figure 5. Illustration of the allowed combinations of nickel and magnesium per formula unit for each spinel composition. ....	28
Figure 6. Room temperature XRD patterns from NiAl <sub>2</sub> O <sub>4</sub> + 2.5 wt% ZrO <sub>2</sub> reduced at temperatures 650 °C to 1100 °C in 300 Torr H <sub>2</sub> . ....	31
Figure 7. Refined lattice parameters for Ni <sub>x</sub> Mg <sub>1-x</sub> Al <sub>2</sub> O <sub>4</sub> . Error bars of one standard deviation are smaller than the data marker.....	34
Figure 8. Room temperature X-ray diffraction patterns showing the (311) reflection of NiAl <sub>2</sub> O <sub>4</sub> after reduction at 850. ....	35
Figure 9. Room temperature X-ray diffraction patterns showing the nickel (111) and the (311) reflection of Ni <sub>0.75</sub> Mg <sub>0.25</sub> Al <sub>2</sub> O <sub>4</sub> .....	36
Figure 10. Goodness of fit for the Rietveld refinements of the closed system reduced spinels.....	37
Figure 11. Refinement of NiAl <sub>2</sub> O <sub>4</sub> + 2.5 wt% ZrO <sub>2</sub> reduced at 750 °C for 29 hours in 300 Torr H <sub>2</sub> , showing a high quality fit. ....	38
Figure 12. Refinement of NiAl <sub>2</sub> O <sub>4</sub> + 2.5 wt% ZrO <sub>2</sub> reduced at 900 °C for 12 hours in 300 Torr H <sub>2</sub> . ....	38
Figure 13. Refinement of Ni <sub>0.75</sub> Mg <sub>0.25</sub> Al <sub>2</sub> O <sub>4</sub> + 2.5 wt% ZrO <sub>2</sub> reduced at 900 °C for 12 hours in 300 Torr H <sub>2</sub> .....	39

Figure 14. Refinement of $\text{Ni}_{0.75}\text{Mg}_{0.25}\text{Al}_2\text{O}_4 + 2.5 \text{ wt\% ZrO}_2$ reduced at 900 °C for 12 hours in 300 Torr $\text{H}_2$ .	39
Figure 15. Refined total site occupancy of the octahedral and tetrahedral site for the closed system reduced $\text{NiAl}_2\text{O}_4 + 2.5 \text{ wt\% ZrO}_2$ .	40
Figure 16. As-synthesized spinel lattice parameters and comparison to an empirical fit for an array of binary spinel compositions by Sickafus	41
Figure 17. Refined nickel metal weight percent reduced from each composition as a function of reduction temperature.	42
Figure 18. Secondary electron image of $\text{NiAl}_2\text{O}_4 + 2.5 \text{ wt\% ZrO}_2$ , reduced at 650 °C in 300 Torr $\text{H}_2$ for 94 hours. 50 kX original magnification.	43
Figure 19. Secondary electron image of $\text{NiAl}_2\text{O}_4 + 2.5 \text{ wt\% ZrO}_2$ , reduced at 700 °C in 300 Torr $\text{H}_2$ for 71 hours. 50 kX original magnification.	44
Figure 20. Observed spinel lattice parameter versus the temperature of reduction. Error bars of one standard deviation are smaller than the data marker.	46
Figure 21. Observed spinel lattice parameters as a function of refined nickel metal weight percent. Error bars are smaller than the data markers.	47
Figure 22. Oxygen parameter in the spinel as a function of the refined weight percent nickel metal	48
Figure 23. Refined weight percent nickel metal versus the combined octahedral and tetrahedral nickel spinel refined site occupancies	49
Figure 24. Microstrain in nickel metal as a function of the refined weight percent of nickel metal.	50
Figure 25. Microstrain in the spinel as a function of the refined weight percent of nickel metal.	51
Figure 26. Value of the tan- dependent hat function convolution used in fitting the nickel metal reflections, as a function of reduction temperature	52
Figure 27. Value of the tan- dependent hat function convolution used in fitting the nickel metal reflections, as a function of the refined weight percent.	53

Figure 28. Refined hat function convolution of nickel metal during HTXRD in flowing N <sub>2</sub> of NiAl <sub>2</sub> O <sub>4</sub> + 2.5 wt% ZrO <sub>2</sub> reduced at 1000 °C.....	54
Figure 29. Refined weight percents of nickel and spinel during the HTXRD measurement in flowing N <sub>2</sub> of NiAl <sub>2</sub> O <sub>4</sub> + 2.5 wt% ZrO <sub>2</sub> .....	55
Figure 30. Ni L and Al K EELS maps from a needle-like nickel particle from the interior of a spinel grain in NiAl <sub>2</sub> O <sub>4</sub> + 2.5 wt% ZrO <sub>2</sub> .....	56
Figure 31. Refined Baddeleyite and tetragonal ZrO <sub>2</sub> weight percents in the reduced spinel composites. Error bars show one standard deviation.....	57
Figure 32. HTXRD of NiAl <sub>2</sub> O <sub>4</sub> + 2.5 wt% ZrO <sub>2</sub> in flowing 4% H <sub>2</sub> /N <sub>2</sub> . Room temperature to 1300 °C. Co-K <sub>α</sub> radiation.....	60
Figure 33. HTXRD of Ni <sub>0.75</sub> Mg <sub>0.25</sub> Al <sub>2</sub> O <sub>4</sub> + 2.5 wt% ZrO <sub>2</sub> in flowing 4% H <sub>2</sub> /N <sub>2</sub> . Room temperature to 1300 °C.....	61
Figure 34. HTXRD of Ni <sub>0.5</sub> Mg <sub>0.5</sub> Al <sub>2</sub> O <sub>4</sub> + 2.5 wt% ZrO <sub>2</sub> in flowing 4% H <sub>2</sub> /N <sub>2</sub> . Room temperature to 1300 °C.....	62
Figure 35. HTXRD of Ni <sub>0.25</sub> Mg <sub>0.75</sub> Al <sub>2</sub> O <sub>4</sub> + 2.5 wt% ZrO <sub>2</sub> in flowing 4% H <sub>2</sub> /N <sub>2</sub> . Room temperature to 1300 °C.....	63
Figure 36. HTXRD of NiAl <sub>2</sub> O <sub>4</sub> in flowing 4% H <sub>2</sub> /N <sub>2</sub> . Room temperature to 1100 °C.....	65
Figure 37. HTXRD of NiAl <sub>2</sub> O <sub>4</sub> + 2.5 wt% ZrO <sub>2</sub> in flowing 4% H <sub>2</sub> /N <sub>2</sub> . Room temperature to 1100 °C.....	65
Figure 38. HTXRD of NiAl <sub>2</sub> O <sub>4</sub> + 2.5 wt% Nb <sub>2</sub> O <sub>5</sub> in flowing 4% H <sub>2</sub> /N <sub>2</sub> . Room temperature to 1100 °C.....	66
Figure 39. HTXRD of NiAl <sub>2</sub> O <sub>4</sub> + 2.5 wt% TiO <sub>2</sub> in flowing 4% H <sub>2</sub> /N <sub>2</sub> . Room temperature to 1100 °C. Corundum formation is seen at 1100 °C.....	67
Figure 40. Final room temperature patterns of the NiAl <sub>2</sub> O <sub>4</sub> + additives HTXRD series .....	68
Figure 41. TGA at 1000 °C in 20 ml/min flowing 4% H <sub>2</sub> /Ar. All samples contained 2.5 wt% ZrO <sub>2</sub> .....	69

Figure 42. TGA at 1000 °C in 20 ml/min flowing 4% H <sub>2</sub> /Ar for an extended dwell for NiAl <sub>2</sub> O <sub>4</sub> and Ni <sub>0.75</sub> Mg <sub>0.25</sub> Al <sub>2</sub> O <sub>4</sub> .....	70
Figure 43. Appearance of the spinel after calcination. From left to right: Ni <sub>x</sub> Mg <sub>1-x</sub> Al <sub>2</sub> O <sub>4</sub> , x = 1, 0.75, 0.5, 0.25, and 0.....	72
Figure 44. Common reduction result during early experiments when a larger reducible mass was used in the furnace .....	72
Figure 45. Non-isothermal TGA measurement began at 750 °C in 20 ml/min flowing 4% H <sub>2</sub> /Ar. Ramp rate was 1 K/min... ..	74
Figure 46. Non-isothermal TGA measurement began at 200 °C in 20 ml/min flowing 4% H <sub>2</sub> /Ar. The ramp rate was 2.5 K/min. ....	75
Figure 47. Comparison of nickel metal phase fraction as determined by Rietveld refinement of X-ray diffraction data and by an isothermal TGA .....	77
Figure 48. Composite and spinel density assuming the model of decreasing nickel, constant Mg/Al ratio, and full oxygen occupancy .....	78
Figure 49. Composite density of spinels reduced in the closed system, plotted as a function of the refined weight percent nickel metal .....	79
Figure 50. Unreduced mixture densities, and densities after reduction in the TGA as a function of nickel metal phase fraction.....	80
Figure 51. Remnant spinel density of samples reduced in the closed system, calculated from the composite density and the refined nickel .....	81
Figure 52. X-Ray diffraction pattern and phase identification of MgAl <sub>2</sub> O <sub>4</sub> + 2.5 wt% ZrO <sub>2</sub> after 16 hours at 1000 °C in 4% H <sub>2</sub> /Ar .....	83
Figure 53. X-Ray diffraction pattern and phase identification of Ni <sub>0.25</sub> Mg <sub>0.75</sub> Al <sub>2</sub> O <sub>4</sub> + 2.5 wt% ZrO <sub>2</sub> after 16 hours at 1000 °C .....	84
Figure 54. X-Ray diffraction pattern and phase identification of Ni <sub>0.5</sub> Mg <sub>0.5</sub> Al <sub>2</sub> O <sub>4</sub> + 2.5 wt% ZrO <sub>2</sub> after 16 hours at 1000 °C in 4% H <sub>2</sub> /Ar .....	85
Figure 55. X-Ray diffraction pattern and phase identification of Ni <sub>0.75</sub> Mg <sub>0.25</sub> Al <sub>2</sub> O <sub>4</sub> + 2.5 wt% ZrO <sub>2</sub> after 40 hours at 1000 °C .....	86

Figure 56. X-Ray diffraction pattern and phase identification of $\text{NiAl}_2\text{O}_4 + 2.5$ wt% $\text{ZrO}_2$ after 40 hours at 1000 °C in 4% $\text{H}_2/\text{Ar}$ .....	87
Figure 57. $\text{Al}_2\text{O}_3 - \text{NiO} - \text{MgO}$ phase diagram showing the $\text{Ni}_x\text{Mg}_{1-x}\text{Al}_2\text{O}_4$ compositions $x = 0.75, 0.5,$ and $0.25$ used in this study. ....	88
Figure 58. $\text{NiAl}_2\text{O}_4 - \text{MgAl}_2\text{O}_4 - \text{Al}_2\text{O}_3$ phase stability diagram. Stability limit between $\text{NiAl}_2\text{O}_4$ and $\text{NiAl}_2\text{O}_4 + \text{Corundum}$ from Rotan et al.....	89
Figure 59. Derived phase stability diagram, showing the remnant spinel compositions which were stable after reduction as blue dots .....	90
Figure 60. Secondary electron image of $\text{NiAl}_2\text{O}_4 + 2.5$ wt% $\text{ZrO}_2$ , calcined for 8 hours at 1500 °C. 10 kX original magnification .....	92
Figure 61. Secondary electron image of $\text{NiAl}_2\text{O}_4 + 2.5$ wt% $\text{ZrO}_2$ , calcined for 8 hours at 1500 °C .....	93
Figure 62. Secondary electron image of $\text{Ni}_{0.75}\text{Mg}_{0.25}\text{Al}_2\text{O}_4 + 2.5$ wt% $\text{ZrO}_2$ , reduced at 850 °C in 300 Torr $\text{H}_2$ for 24 hours.....	94
Figure 63. Low-voltage secondary electron image of $\text{NiAl}_2\text{O}_4 + 2.5$ wt% $\text{ZrO}_2$ , reduced at 750 °C in 300 Torr $\text{H}_2$ for 29 hours.....	95
Figure 64. Low-voltage secondary electron image of $\text{NiAl}_2\text{O}_4 + 2.5$ wt% $\text{ZrO}_2$ , reduced at 750 °C in 300 Torr $\text{H}_2$ for 29 hours.....	96
Figure 65. Secondary electron image of $\text{NiAl}_2\text{O}_4 + 2.5$ wt% $\text{ZrO}_2$ , reduced at 850 °C in 300 Torr $\text{H}_2$ for 24 hours. 50 kX original magnification.....	97
Figure 66. Secondary electron image of $\text{NiAl}_2\text{O}_4 + 2.5$ wt% $\text{ZrO}_2$ , reduced at 900 °C in 300 Torr $\text{H}_2$ for 12 hours. 50 kX original magnification.....	98
Figure 67. Low-voltage secondary electron image of $\text{NiAl}_2\text{O}_4 + 2.5$ wt% $\text{ZrO}_2$ , reduced at 900 °C in 300 Torr $\text{H}_2$ for 12 hours.....	99
Figure 68. Low-voltage secondary electron image of $\text{NiAl}_2\text{O}_4 + 2.5$ wt% $\text{ZrO}_2$ , reduced at 900 °C in 300 Torr $\text{H}_2$ for 12 hours.....	100

Figure 69. Secondary electron image of NiAl <sub>2</sub> O <sub>4</sub> + 2.5 wt% ZrO <sub>2</sub> , reduced at 950 °C in 300 Torr H <sub>2</sub> for 12 hours. 20 kX original magnification.....	101
Figure 70. Secondary electron image of NiAl <sub>2</sub> O <sub>4</sub> + 2.5 wt% ZrO <sub>2</sub> , reduced at 1000 °C in 300 Torr H <sub>2</sub> for 12 hours. 20 kX original magnification.....	102
Figure 71. Secondary electron image of NiAl <sub>2</sub> O <sub>4</sub> + 2.5 wt% ZrO <sub>2</sub> , reduced at 1000 °C in 300 Torr H <sub>2</sub> for 12 hours. 50 kX original magnification.....	103
Figure 72. Secondary electron image of NiAl <sub>2</sub> O <sub>4</sub> + 2.5 wt% ZrO <sub>2</sub> , reduced at 1100 °C in 300 Torr H <sub>2</sub> for 12 hours. 20 kX original magnification.....	104
Figure 73. Secondary electron image of Ni <sub>0.75</sub> Mg <sub>0.25</sub> Al <sub>2</sub> O <sub>4</sub> + 2.5 wt% ZrO <sub>2</sub> , reduced at 850 °C in 300 Torr H <sub>2</sub> for 24 hours.....	105
Figure 74. STEM EDS maps of an agglomerate of spinel and ZrO <sub>2</sub> particles, NiAl <sub>2</sub> O <sub>4</sub> + 2.5 wt% ZrO <sub>2</sub> reduced at 850 °C for 24 hours in 300 Torr H <sub>2</sub> .....	106
Figure 75. Back scatter SEM image of a cross section of NiAl <sub>2</sub> O <sub>4</sub> + 2.5 wt% ZrO <sub>2</sub> reduced at 900 °C for 12 hours in 300 Torr H <sub>2</sub> .....	108
Figure 76. Comparison of refined nickel crystallite sizes to those observed in the SEM for NiAl <sub>2</sub> O <sub>4</sub> + 2.5 wt% ZrO <sub>2</sub> .....	109
Figure 77. TEM image of a specimen cut from NiAl <sub>2</sub> O <sub>4</sub> + 2.5 wt% ZrO <sub>2</sub> reduced at 850 °C for 24 hours in 300 Torr H <sub>2</sub> with a FIB.....	111
Figure 78. TEM image of a specimen cut from NiAl <sub>2</sub> O <sub>4</sub> + 2.5 wt% ZrO <sub>2</sub> reduced at 900 °C for 12 hours in 300 Torr H <sub>2</sub> with a FIB.....	112
Figure 79. TEM image of a specimen cut from NiAl <sub>2</sub> O <sub>4</sub> + 2.5 wt% ZrO <sub>2</sub> reduced at 950 °C for 12 hours in 300 Torr H <sub>2</sub> with a FIB.....	113
Figure 80. Back scatter SEM image of a cross section of NiAl <sub>2</sub> O <sub>4</sub> + 2.5 wt% ZrO <sub>2</sub> reduced at 900 °C for 12 hours in 300 Torr H <sub>2</sub> .....	114
Figure 81. Back scatter SEM image of a cross section of NiAl <sub>2</sub> O <sub>4</sub> + 2.5 wt% ZrO <sub>2</sub> reduced at 950 °C for 12 hours in 300 Torr H <sub>2</sub> .....	115

## ABSTRACT

The reduction of  $\text{Ni}_x\text{Mg}_{1-x}\text{Al}_2\text{O}_4$  in  $\text{H}_2$  to form nickel metal and a remnant oxide was characterized by XRD, HTXRD, TGA, pycnometry, TEM, and SEM. The aim of the work was to investigate the dynamics of the system to better understand its capabilities and limitations for catalysis applications.  $\text{ZrO}_2$  was added to the majority of samples to discourage the transformation of metastable spinel phases to  $\Theta$  or  $\alpha\text{-Al}_2\text{O}_3$ .

As the reduction progresses, one  $\text{O}^{2-}$  is lost for each  $\text{Ni}^{2+}$  which reduces to Ni metal. The temperature of the onset of reduction was shown to vary by composition in flowing 4%  $\text{H}_2/\text{Ar}$  via TGA, with  $\text{NiAl}_2\text{O}_4$  beginning to reduce at  $\sim 780$  °C. The onset temperature of lower nickel compositions were quite close to each other, starting at  $\sim 900$  °C for  $\text{Ni}_{0.75}\text{Mg}_{0.25}\text{Al}_2\text{O}_4$ .

$\text{Ni}_{0.25}\text{Mg}_{0.75}\text{Al}_2\text{O}_4$  and  $\text{Ni}_{0.5}\text{Mg}_{0.5}\text{Al}_2\text{O}_4$  were shown to form Ni metal and a non-stoichiometric spinel of the same Mg-Al ratio as the starting composition.  $\text{NiAl}_2\text{O}_4$  and  $\text{Ni}_{0.75}\text{Mg}_{0.25}\text{Al}_2\text{O}_4$  were found to become unstable as full reduction was approached, and metastable spinel,  $\Theta\text{-Al}_2\text{O}_3$ , and  $\alpha\text{-Al}_2\text{O}_3$  formed sequentially given sufficient time at temperature.

A phase diagram was constructed in a previously uninvestigated region of the  $\text{NiAl}_2\text{O}_4\text{-MgAl}_2\text{O}_4\text{-Al}_2\text{O}_3$  ternary phase diagram using the phase stability of the remnant spinel as indication of the edge of the spinel stability phase field.

Rietveld refinements were performed on all compositions reduced at temperatures from 650 to 1100 °C to quantify structural changes in the spinel and phase fraction, crystallite size and microstrain in all phases.

The formation of non-stoichiometric spinel upon reduction was confirmed by density measurements of the reduced specimens using helium pycnometry.

Significant progress was made towards understanding the dynamics of an important catalyst system. The majority of nickel metal was present as faceted crystallites on the surface, explaining previously observed high catalytic activities. Subsequent studies can use the phase stability and kinetic results of this work to identify additives to stabilize the metastable spinel structures. Good candidates were identified in  $\text{ZrO}_2$  and  $\text{Nb}_2\text{O}_5$ , and  $\text{TiO}_2$  was found to promote the formation of corundum.

## INTRODUCTION

### A. The Importance of Spinel

Many compounds with the spinel structure possess technologically important electrical, magnetic, and refractory properties. Spinel has also been widely used as a model system to examine the relative stabilities of tetrahedral versus octahedral coordination for different ions.<sup>1</sup> Broad solid solution formation is possible with spinels, allowing site preferences to be examined as a function of gradual changes in chemistry.

### B. Properties of Spinel

Magnesium aluminate spinel ( $\text{MgAl}_2\text{O}_4$ ) is noted both for its exceptional resistance to chemical attack, and its mechanical properties at high temperatures. As such, magnesium spinel is a desirable refractory material, but is rarely used as such due to the costs brought on by the difficulties in its processing. Spinel is a difficult material to sinter, with sintering temperatures of  $\sim 1800$  °C necessary to obtain full mechanical properties by traditional ceramic manufacturing routes.  $\text{MgAl}_2\text{O}_4$  experiences a 5% volume expansion upon its phase formation from its starting oxides, reducing the density of the powder compact and retarding densification. Due to this volume expansion, a calcination stage followed by extensive crushing and milling is required. This extra processing, combined with the high temperatures required, is responsible for its high cost.<sup>2</sup>

Nickel aluminate spinel ( $\text{NiAl}_2\text{O}_4$ ) has garnered attention because it can be reduced at high temperature to form a nickel metal reinforced corundum matrix composite, of particular interest for use in high temperature structural applications, or an oxide supported nickel metal catalyst. It has also been of interest for its magnetic properties, high thermal stability, and for use as an anode in aluminum production because of its high resistance to alkalis and attack by molten aluminum.<sup>3-7</sup> Nickel spinel is also difficult to sinter.

### C. Spinel Structure

Spinel is generally regarded as a simple structure type, but they are actually quite complex due to the ability of the spinel to slightly rearrange its structure to accommodate non-stoichiometry, or allow site substitution of cations. Spinel is typically an oxide, but spinels with S, Se, and Te anions also exist.<sup>8</sup> The spinel structure is space group  $Fd\bar{3}m$ , International Crystallographic Tables number 227. The Bravais lattice is face centered cubic, and the basis is two formula units. Consequently, 8 formula units occupy each unit cell.

Described most simply, an oxide spinel is of general formula  $AB_2O_4$ , consisting of a nearly close packed oxygen sublattice, and a cation sublattice of 8 tetrahedral and 16 octahedral sites. Spinel of varying A-B valence pairs exist: II – III spinels are the most common, where the A cation is 2+ and the B cation 3+, but IV – II, VI - I, and I - II spinels exist also, with the IV – II being by far the most common of the latter three.<sup>9</sup> Chemists refer to spinels as  $AB_2O_4$  where the A site is tetrahedral, and the B site octahedral, whereas mineralogists define spinels as  $A_2BO_4$  compounds, reversing the conventions. The  $AB_2O_4$  convention will be used throughout this work. There are a total of 96 interstices within the 32  $O^{2-}$  ions; 64 tetrahedral and 32 octahedral. Of the 64 tetrahedral interstices, 8 are occupied, and 16 of the 32 octahedral interstices are occupied.

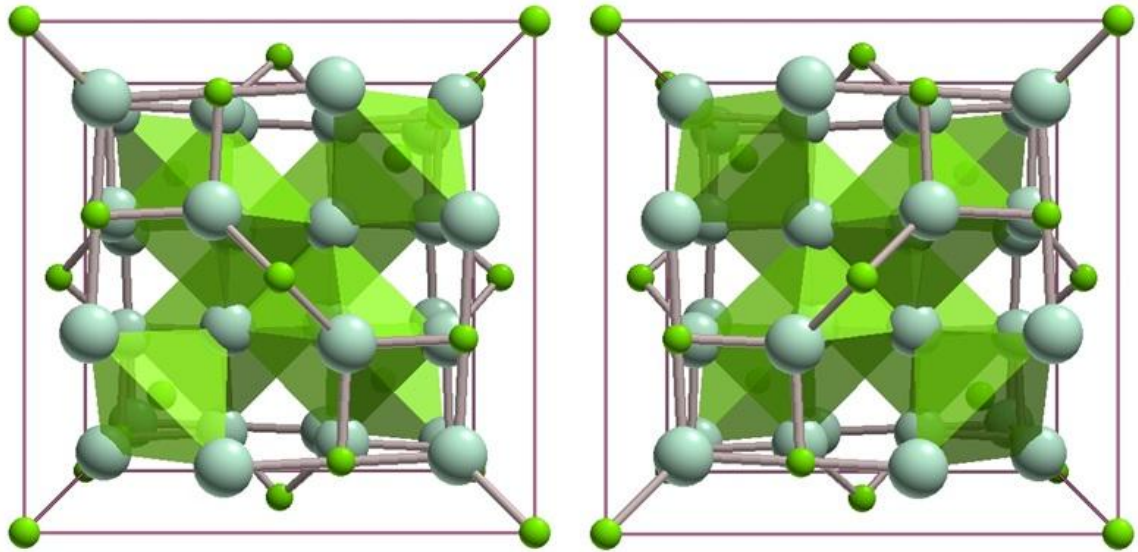


Figure 1. Spinel unit cell viewed along the [010] and [100].

Many choices are possible for the origin, all of point symmetry  $\bar{4}3m$  or  $\bar{3}m$ . The origin can also be assigned to a vacant point or an occupied site. The most common choices are  $\bar{4}3m$  on an occupied tetrahedral position, or  $\bar{3}m$  on an octahedral vacancy, which is an inversion center. The  $\bar{3}m$  origin will be used in this work. The  $\bar{4}3m$  setting can be obtained by translating all  $\bar{3}m$  lattice positions by  $(-a/8)$ .

The tetrahedral and octahedral positions are special, located at  $x = 0.125, y = 0.125, z = 0.125$ , and  $x = 0.5, y = 0.5, z = 0.5$  respectively. These positions correspond to Wyckoff 8a and 16d.<sup>8</sup> The anion position is a general position, and must lie on the [111], Wyckoff general position 32e. Tetrahedral sites are isolated from one another, sharing only corners with neighboring octahedra. Six of the twelve edges of each octahedra are shared with neighboring octahedra.

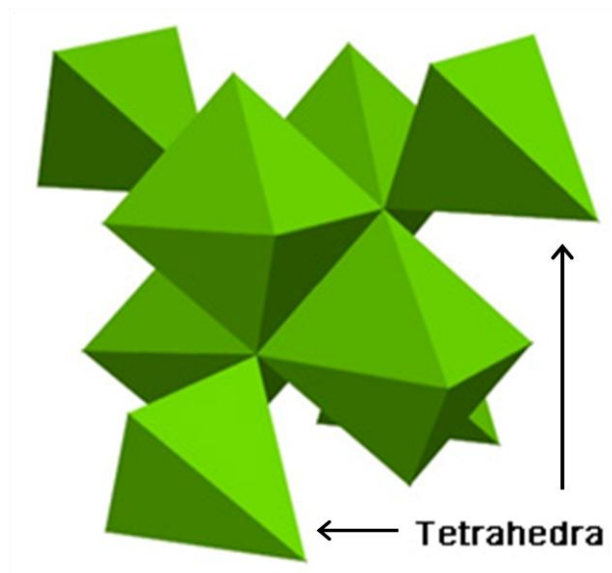


Figure 2. Perspective image of the spinel structure showing the edge-sharing nature of the octahedral sites and the isolated nature of the tetrahedral sites.

Three degrees of freedom define the spinel structure: the lattice parameter,  $a$ , the inversion parameter,  $i$ , and the anion parameter,  $u$ . It is the simultaneous variation of these three parameters that allows spinel to accommodate so many changes.

The lattice parameter of spinels is large, with  $a = 8.80898 \text{ \AA}$  for naturally occurring  $\text{MgAl}_2\text{O}_4$ . Inversion refers to the occupancy of the tetrahedral site by the majority cation. There are twice as many B atoms as tetrahedral sites, so in a fully inverse spinel, all of the tetrahedral sites are occupied by the B ion, with half of the octahedral sites occupied by the rest of the B ions, and the other half of the octahedral sites being occupied by the A ion. In a normal spinel, the A atoms reside on only the tetrahedral sites, with the B atoms on only the octahedral sites. Most spinels lie somewhere between these two extremes, with the inversion parameter,  $i$ , defined as the fraction of the tetrahedral sites occupied by the B atom. A completely random cation arrangement is described by  $i = 0.66$ , which in general all spinels tend toward at higher temperature, whether normal or inverse. Inversion can come from maximizing configurational entropy, maximizing the Madelung constant, or can be due to a transition metal ion with a large octahedral site preference energy, originating from its d-orbital electrons. Inversion has been shown to be an equilibrium function of temperature,

composition, pressure, ionic charge, ionic radii, crystal and ligand field effects, and anion polarization.<sup>1</sup>

Typical values for the anion parameter,  $u$ , are between 0.24 and 0.275. In the  $\bar{3}m$  setting, an oxygen parameter  $u = 0.25$  is a perfectly close-packed oxygen sublattice, with deviation from 0.25 giving a less closely packed sublattice. As  $u$  increases above 0.25, the tetrahedral site becomes enlarged at the expense of the octahedral site.<sup>10</sup> Deviations in  $u$  have an important effect on bond lengths in spinel, which consequently have a significant causal link to the preferred diffusion modes. O'Neill and Navrotsky<sup>10</sup> have provided equations which express the tetrahedral-oxygen and octahedral-oxygen bond lengths in terms of  $a$  and  $u$ .

$$R_{tet} = a \sqrt{3 \left[ u - \frac{1}{8} \right]} \quad (1)$$

$$R_{oct} = a \sqrt{3u^2 - 2u + \frac{3}{8}} \quad (2)$$

The oxygen parameter varies such that the volume of the tetrahedral and octahedral interstice matches the volume of each ion. The variation of the inversion parameter, exchanging cations from the octahedral site to the tetrahedral site, will likewise alter the average cationic radii for each site. The simultaneous variation of these three parameters will minimize the energy of the structure.

Sickafus et al. have computed empirical fits for  $a$  and  $u$  from a compilation of literature data, shown in Equations 3, 4, and 5. Equation 3 computes the average cation radius to be used in Equation 4. Equation 4 gives a least squares fit value for the spinel lattice parameter in angstroms as a function of the average cation radii. Equation 5 gives  $u$  as a function of the cation radius ratio, computed with knowledge of the inversion of the spinel. The  $-1/8$  is to move  $u$  from the  $\bar{4}3m$  point symmetry convention in which it was given to the  $\bar{3}m$  point symmetry convention.

$$\langle r(M) \rangle = 0.33 r_{tet} + 0.66 r_{oct} \quad (3)$$

$$a = 5.815 + 4.143\langle r(M) \rangle \quad (\chi^2 = 0.968) \quad (4)$$

$$u = -\frac{1}{8} + 0.3876 \left[ \frac{\langle r(B) \rangle}{\langle r(A) \rangle} \right]^{-0.07054} \quad (\chi^2 = 0.9944) \quad (5)$$

#### D. NiAl<sub>2</sub>O<sub>4</sub> - MgAl<sub>2</sub>O<sub>4</sub>

Table I provides relevant properties of NiAl<sub>2</sub>O<sub>4</sub> and MgAl<sub>2</sub>O<sub>4</sub>. The 8.083 Å lattice parameter of MgAl<sub>2</sub>O<sub>4</sub> is larger than the 8.048 Å lattice parameter of NiAl<sub>2</sub>O<sub>4</sub>. This larger lattice parameter, along with the lower atomic weight of Mg relative to Ni, gives a much lower density for MgAl<sub>2</sub>O<sub>4</sub>. The reported lattice parameter of NiAl<sub>2</sub>O<sub>4</sub> varies somewhat due to the length of time necessary for the cation distribution to reach equilibrium at low temperatures. MgAl<sub>2</sub>O<sub>4</sub> is a largely normal spinel, with typical *i* at room temperature reported from 0.05 to 0.33.<sup>11</sup> NiAl<sub>2</sub>O<sub>4</sub> is a largely inverse spinel, with typical *i* at room temperature reported from 0.86 to 0.9. The oxygen parameter for MgAl<sub>2</sub>O<sub>4</sub> is reported by Hill et al.<sup>12</sup> to be 0.2624 and 0.256 for NiAl<sub>2</sub>O<sub>4</sub>.

Table I. Structural Parameters of the Solid Solution Endmembers

	Lattice Parameter <sup>1,13</sup>	<i>u</i> <sup>12,13</sup>	<i>i</i> <sup>12,14</sup>	ρ <sup>9</sup> (g/cm <sup>3</sup> )
MgAl <sub>2</sub> O <sub>4</sub>	8.083	0.2624	0.05 - 0.33	3.58
NiAl <sub>2</sub> O <sub>4</sub>	8.045 - 8.048	0.254 - 0.256	0.86 - 0.9	4.50

Determination of *i* in NiAl<sub>2</sub>O<sub>4</sub> is straightforward given the difference in the X-ray scattering power of Ni and Al. Magnetic susceptibility methods have also been used as a supplementary means to assess inversion in NiAl<sub>2</sub>O<sub>4</sub>, although this method can measure relative changes only, not an absolute measurement.<sup>1</sup> Several studies have looked at *i* in NiAl<sub>2</sub>O<sub>4</sub> as a function of quench temperature, since it serves as a good model system for the validation of thermodynamic site mixing models due to the straightforward determination of inversion by X-ray diffraction.<sup>1,3,13,15,16</sup> Accurate determination of *i* in

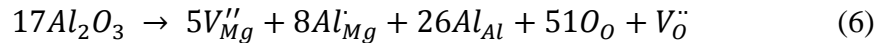
MgAl<sub>2</sub>O<sub>4</sub> is exceedingly difficult due to the very similar X-ray scattering power of Al and Mg. This results in large errors in the refined occupancies on each site, giving a large uncertainty in the inversion.

### E. Non-Stoichiometric Spinel

MgAl<sub>2</sub>O<sub>4</sub> is capable of dissolving both excess MgO and Al<sub>2</sub>O<sub>3</sub>, although the total extent of dissolution of MgO is lower and requires a higher temperature. Al<sub>2</sub>O<sub>3</sub> dissolution is charge compensated by cation vacancies, distributed on both octahedral and tetrahedral sites,<sup>17</sup> and possibly by a small number of oxygen vacancies as well.<sup>18</sup> MgO dissolution starts at 1800 °C.<sup>19</sup> Al<sub>2</sub>O<sub>3</sub> dissolution is possible at lower temperatures, with dissolution beginning at 700 °C, and MgO·2Al<sub>2</sub>O<sub>3</sub> stable at 1600°C, and MgO·4Al<sub>2</sub>O<sub>3</sub> stable at 1800°C. NiAl<sub>2</sub>O<sub>4</sub> is not capable of dissolving excess NiO, but can dissolve excess Al<sub>2</sub>O<sub>3</sub>, but less than MgAl<sub>2</sub>O<sub>4</sub>. Excess Al<sub>2</sub>O<sub>3</sub> results in a smaller lattice parameter for both NiAl<sub>2</sub>O<sub>4</sub> and MgAl<sub>2</sub>O<sub>4</sub>.<sup>19-21</sup>

The solubility limit for Al<sub>2</sub>O<sub>3</sub> in NiAl<sub>2</sub>O<sub>4</sub> lies between 55 and 58 mole percent Al<sub>2</sub>O<sub>3</sub>, with a minimum lattice parameter of 8.0272 Å, as reported by Rotan et al.<sup>21</sup> The oxygen parameter was also seen to decrease with excess Al<sub>2</sub>O<sub>3</sub>, from 0.2558 at stoichiometric NiAl<sub>2</sub>O<sub>4</sub>, to ~ 0.2552 at the stability limit, although there was considerable scatter in the data over this range. The inversion parameter was observed to remain substantially constant at 0.82, with nickel occupancy on both the octahedral and tetrahedral site decreasing uniformly as a function of increasing Al<sub>2</sub>O<sub>3</sub>.

Okuyama et al.<sup>18</sup> have investigated the density of Al-rich nonstoichiometric MgAl<sub>2</sub>O<sub>4</sub> using single crystals grown by the Verneuil method. They found the dissolution of Al<sub>2</sub>O<sub>3</sub> in MgAl<sub>2</sub>O<sub>4</sub> to be charge compensated for by the formation of tetrahedral vacancies and a smaller number of oxygen vacancies, as shown in Equation 6.



The exact ratio of oxygen vacancies to Al<sub>2</sub>O<sub>3</sub> dissolved is questionable however, as Okuyama determined the stoichiometry of the single crystals by comparison to the lattice parameter of polycrystalline non-stoichiometric spinels synthesized by conventional solid state techniques. No allowances were made for differing anion parameter or inversion between the two sets of samples, which could be very different

given the synthesis method employed to create the single crystals, and would alter the lattice parameter for a given stoichiometry. However, regardless of this detail, Okuyama's data supports the formation of oxygen vacancies. Oxygen vacancy formation is also supported by the work of Reddy and Cooper, who have shown the oxygen self-diffusion coefficient to be higher in non-stoichiometric spinel than in stoichiometric spinel.<sup>22</sup>

No information is available in the literature as to the solubility of  $\text{Al}_2\text{O}_3$  in the solid solution of  $\text{NiAl}_2\text{O}_4 - \text{MgAl}_2\text{O}_4$ .

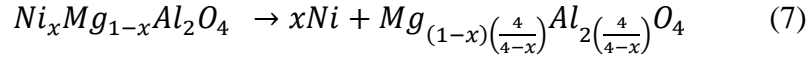
## F. Reduction Process

Many instances of the reduction of  $\text{NiAl}_2\text{O}_4$  are available in literature.<sup>23-33</sup> These are typically for use as structural materials or catalysts, but little information is available on the reduction of  $\text{Ni}_x\text{Mg}_{1-x}\text{Al}_2\text{O}_4$ . Quenard investigated the reduction of  $\text{Co}_x\text{Mg}_{1-x}\text{Al}_2\text{O}_4$  and  $\text{Ni}_x\text{Mg}_{1-x}\text{Al}_2\text{O}_4$ , but the transition metal loadings were quite low, sufficient to give four weight percent metal at complete reduction. At sufficiently low oxygen partial pressures,  $\text{Ni}^{2+}$  will leave  $\text{Ni}_x\text{Mg}_{1-x}\text{Al}_2\text{O}_4$  to form Ni metal. A corresponding number of  $\text{O}^{2-}$  leaves the spinel concurrently with the nickel, as demonstrated by thermogravimetric analysis in flowing hydrogen.

In previous work by our group at Alfred University, it was reported that both  $V''_{\text{Ni}}$  and  $V''_{\text{O}}$  remained in the spinel until a high extent of reduction was achieved and metastable spinels formed.<sup>34</sup> In conducting the present work, it was found that a calculation error had been made in extracting the spinel density from the density of the mixture of spinel and nickel metal. The density of the spinel as calculated with this error appeared to support an equal number of  $V''_{\text{Ni}}$  and  $V''_{\text{O}}$ . Rietveld refinement of X-ray and neutron diffraction data show no strong preference to one model or the other. This is not surprising, as the switch from one model to the other maintains the same structure and stoichiometry, and only confines the spinel to a smaller volume. When the error was corrected, the remnant spinel density was seen to match that of an increasingly Mg and Al rich spinel.

It has been conclusively shown that the spinel loses oxygen during reduction, but it is also clear that oxygen vacancies do not accumulate. After forming,  $V''_{\text{Ni}}$  and  $V''_{\text{O}}$

would be free to move within the structure by the counter-diffusion of ions, though likely in a coordinated manner due to their charged nature. Presumably the vacancies move to the surface or consolidate to form internal porosity to leave the spinel Mg and Al rich with full oxygen occupancy, as shown in Equation 7.



From a practical standpoint, the extent of reduction that a sample undergoes in a closed system is determined by the reducible sample mass, the volume of the system, the temperature gradient in the system, and the starting moisture content. At the start of the reaction, X moles of H<sub>2</sub> are present in the furnace, along with Y moles of H<sub>2</sub>O. Given that the furnace has been continuously pumped on by a roughing pump as it heats at 3 K/min to the target reduction temperature, the amount of H<sub>2</sub>O present should be very low. The ratio between the partial pressures of H<sub>2</sub> and H<sub>2</sub>O and the temperature of the furnace determine the PO<sub>2</sub>.



$$\Delta G^\circ = -RT \ln \left[ \frac{a(H_2O)^2}{a(H_2)^2 a(O_2)} \right] \quad (9)$$

$$\Delta G^\circ = -RT \ln \left[ \frac{P(H_2O)^2}{P(H_2)^2 P(O_2)} \right] \quad (10)$$

$$P(O_2) = e^{-\frac{\Delta G^\circ}{RT}} \left[ \frac{P(H_2O)^2}{P(H_2)^2} \right] \quad (11)$$

If the PO<sub>2</sub> is below the dissociation pressure of any of the compositions present, Equation 12 will progress to the right. This consumes H<sub>2</sub>, forming H<sub>2</sub>O.



The back reaction of 8 to re-establish equilibrium in the atmosphere will raise the PO<sub>2</sub>. For an isothermal reduction, the rate of the reaction will slow as the affinity for the reaction is decreased, due to the increasing PO<sub>2</sub> and the change in the phase composition to be closer to that of equilibrium. The reaction will further slow as the reaction interface advances into the spinel particle, increasing the necessary diffusion distances. The reaction will continue to proceed at a continuously decreasing rate until the PO<sub>2</sub> has risen such that it is in equilibrium with the current phase composition. The X starting moles of H<sub>2</sub> in the furnace are capable of reducing X moles of Ni metal out of the spinel, but only

if the  $\text{H}_2\text{O}/\text{H}_2$  ratio remains low enough to keep the  $\text{PO}_2$  below the dissociation pressure of the spinel. Whether or not there is enough  $\text{H}_2$  to meet this criteria depends on the reducible nickel mass and the moles of  $\text{H}_2$  in the furnace, with the number of moles of  $\text{H}_2$  being determined by the pressure of  $\text{H}_2$  applied, the volume of the furnace, and its specific thermal gradient.

If there is an insufficient number of moles of  $\text{H}_2$  present to maintain a  $\text{PO}_2$  below the dissociation pressure of the compositions present, the reduction will proceed to an extent in each composition governed by its particular dissociation pressure. The reduction will proceed the furthest in the composition with the highest dissociation pressure, and the least in the composition with the lowest dissociation pressure.

If using a flowing reducing gas rather than a closed system, the  $\text{H}_2\text{O}$  formed from the reduction will be continuously swept away from the sample and the  $\text{PO}_2$  will remain constant for any fixed temperature. The reaction rate will still slow as the reaction progresses due to the lowered affinity for the reaction as the change in phase composition approaches the equilibrium phase assemblage. The advancement of the reaction interface into the powder will also slow the reaction rate, but the  $\text{PO}_2$  will not increase.

The use of both flowing gas and closed system reductions can yield valuable data, but they have very different characteristics. Unless atmospheres and sample masses are chosen with great care and extensive knowledge of the system, a reduction performed for a certain time and temperature under flowing gas is unlikely to yield the same results if performed in a closed system. The possibility of reactions of system components with the atmosphere to alter  $\text{PO}_2$  is an additional complication.

The  $\text{PO}_2$  equilibrium phase diagram for  $\text{NiAl}_2\text{O}_4$  was determined by Elrefaie and Smeltzer<sup>35</sup> between 1123 and 1423K with the use of a galvanic cell and a calcia-stabilized zirconia electrolyte. They found the dissociation pressure of the Ni-NiO equilibria and the  $\text{NiAl}_2\text{O}_4 + \text{NiO} - \text{NiAl}_2\text{O}_4 + \text{Ni}$  to be very similar, within one order of magnitude in  $\text{PO}_2$ ,  $3.8 \times 10^{-11}$  at 1000 °C. The Ni + corundum phase field is ~ 2 orders of magnitude lower,  $4.9 \times 10^{-13}$  at 1000 °C. At very low  $\text{PO}_2$ ,  $\sim 10^{-23}$  at 1000 °C, a small amount of Al will reduce from corundum, forming a Ni-Al alloy.

## G. Nucleation, Growth, Diffusion

The final microstructure of the reduced composite is dependent upon both the starting microstructure and the reduction conditions. A small initial grain size or a small particle size will result in a composite with a greater number of small metal crystallites due to the greater number of nucleation sites. A small particle size will also yield a greater fraction of metal crystallites on the surface as compared to a larger particle size due to the reduced diffusion distance to the surface. Short circuit diffusion effects could also play a role given the right combination of microstructure and reduction temperature, affecting metal particle shape and distribution. The reduction of  $\text{Ni}^{2+}$  to  $\text{Ni}^0$  requires the diffusion of  $\text{H}_2$  and the  $\text{Ni}^{2+}$  to bring the two species together. Lattice diffusion is typically the slowest diffusion process. Imperfections in the crystal, whether grain boundaries or dislocations, offer a much faster diffusion pathway. In temperature regimes where lattice diffusion is sufficiently slow, the bulk of the reduction reaction will be concentrated around these fast diffusion pathways. Given that dislocations, and grain boundaries in specific areas, tend to be straight, this results in long, narrow metal crystallites reduced from the ceramic. Rogers and Trumble have examined reduction reactions in the system  $(\text{Mg,Ni})\text{O}$  as a function of stoichiometry and treatment temperature.<sup>36</sup> Their own work and analysis of published work supports the appearance of uniform reduction microstructures at reduction temperature above 0.5 of the homologous melting temperature, and non-uniform microstructures below 0.5 of the homologous melting temperature. This trend was observed for  $(\text{Mg,Ni})\text{O}$ , single crystals and polycrystals,  $(\text{Mn,Fe})\text{O}$  polycrystals, and in single crystals of  $(\text{Mg,Cu})\text{O}$  and  $(\text{Mg,Co})\text{O}$ . This threshold was seen to vary somewhat with composition.

The reduction parameters used also greatly affect the final microstructure. Lower  $\text{PO}_2$  and higher temperature both increase the kinetics of the reaction. At higher reaction rates, inhomogeneous nucleation is likely to be preferred to homogenous nucleation. This would concentrate the metal crystallites around defects and result in larger crystallites as there are fewer nucleation sites available. Higher reduction temperatures would also shift crystallites to larger sizes due to Ostwald ripening processes.<sup>37</sup>

## H. Addition of Zirconia

Transition aluminas are frequently used as metallic catalyst supports, as they are high surface area materials, and also provide beneficial catalyst-support interactions.<sup>38</sup> A constant difficulty in working with transition aluminas is the possibility of a phase transformation to  $\Theta$  or  $\alpha$ - $\text{Al}_2\text{O}_3$ . This results in a catastrophic loss of porosity, and can severely reduce or entirely eliminate the activity of the catalyst. To circumvent this, reaction temperatures are controlled to a temperature low enough such that the transition alumina maintains its structure for the necessary time period,<sup>39</sup> However, some reactions require higher temperatures, and others would enjoy greater efficiencies with a higher reaction temperature.

A current research project at Alfred University aims to utilize reduced spinels as an internally reforming fuel cell anode, which can be oxidized then re-reduced to burn off coke deposits or certain compounds which are poisonous to the catalytic activity. A performance benefit would be realized for this application if the anode could operate at higher temperature or for longer times without sacrificing performance by forming less catalytically active oxide phases. For this reason, a search was conducted for additives that would allow the use of higher nickel compositions by discouraging the formation of  $\Theta$  phase metastable spinel or corundum.

Üstündag et al.<sup>31</sup> reduced monolithic  $\text{NiAl}_2\text{O}_4$  samples without  $\text{ZrO}_2$  and with various  $\text{ZrO}_2$  loadings, at 1100, 1300, and 1350 °C in a  $\text{CO}/\text{CO}_2$  mixture to control  $\text{PO}_2$ . After reduction, the  $\text{ZrO}_2$  samples showed a tendency to retain greater amounts of defect spinel and form less corundum. For this reason, phase stability studies of  $\text{Ni}_x\text{Mg}_{1-x}\text{Al}_2\text{O}_4 + 2.5$  weight percent  $\text{ZrO}_2$  were conducted.

## I. Metastable Phases Based on the Spinel Structure

Several groups have reported observations of metastable phases related to the spinel structure which contain greater amounts of alumina than the solubility limit of alumina in spinel.<sup>40-44</sup> At very high temperatures, ~1900 °C, the spinel phase field extends almost to pure  $\text{Al}_2\text{O}_3$ . Upon cooling from the melt, different mixtures of  $\text{NiO}$  or  $\text{MgO}$  and  $\text{Al}_2\text{O}_3$ , metastable phases form as precipitates, or crystallize upon annealing. This is contrary to the mixture of  $\text{Al}_2\text{O}_3$ -rich non-stoichiometric  $\text{NiAl}_2\text{O}_4$  and corundum

the equilibrium phase diagram predicts. Metastable phases have been observed at stoichiometries of  $\text{NiAl}_6\text{O}_{10}$ ,  $\text{NiAl}_{10}\text{O}_{16}$ ,  $\text{NiAl}_{26}\text{O}_{40}$ , and  $\text{NiAl}_{32}\text{O}_{49}$  and a poorly characterized phase with  $\frac{\text{Al}_2\text{O}_3}{\text{NiO}} > 99$ . There also exists a high temperature phase of a structure continuous between that of the “A” and  $\epsilon$  phases. Upon annealing for periods of  $\sim 150$  hours at  $1050^\circ\text{C}$ , the metastable phases transition to a mixture of spinel and corundum.<sup>41</sup>

The  $\Theta$  phase has been reported to be isomorphic with  $\beta\text{-Ga}_2\text{O}_3$ , as is the metastable  $\Theta\text{-Al}_2\text{O}_3$  phase. However, the reported space group of the metastable spinel  $\Theta$  is  $\text{P2}/\text{m}$ , which is not equivalent with  $\text{C2}/\text{m}$ , the space group reported for  $\beta\text{-Ga}_2\text{O}_3$  and  $\Theta\text{-Al}_2\text{O}_3$ .<sup>45</sup>

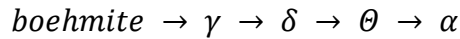
The remaining A, B,  $\epsilon$ , and  $\delta_3$  phases have been shown to be periodic antiphase boundary (PAPB) structures built on the spinel phase. The PAPB structures induce a slight distortion in the oxygen sublattice and paired octahedral vacancies are in the vicinity of the twin domain boundaries. Unit cells have been assigned to all the PAPB phases, but a space group has been assigned only to  $\text{NiAl}_{10}\text{O}_{16}$ , the B phase, by Bassoul and Gilles, as  $\text{P2}_1/\text{b}$ . They have asserted that accurate space group determination for these structures can be made only by single crystal or electron diffraction techniques. Known information on these metastable phases is compiled in Table II.

Table II. Structural Parameters of the Metastable Nickel Spinel Phases<sup>40-43</sup>

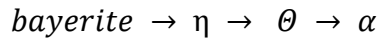
Phase Name	Stoichiometry	Bravais Lattice	Space Group	a (Å)	b (Å)	c (Å)	$\beta$	$\gamma$
A	NiAl <sub>6</sub> O <sub>10</sub>	Monoclinic						
B	NiAl <sub>10</sub> O <sub>16</sub>	Monoclinic	P2 <sub>1</sub> /b	7.98	15.75	7.95	-	91.1°
$\epsilon$	NiAl <sub>10</sub> O <sub>16</sub>	Monoclinic						
$\delta_3$	NiAl <sub>26</sub> O <sub>40</sub>	Tetragonal	P12/m1	7.958	7.958	11.768	-	-
$\varphi_{Ni}$	NiAl <sub>32</sub> O <sub>49</sub>	Monoclinic		9.305	5.631	12.098	100.9	-
$\Theta_{Ni}$	$\frac{Al_2O_3}{NiO} > 99$	Monoclinic	P2/m	5.62	2.91	11.78	104.09	-

## J. Transition Aluminas

Alumina possesses a host of metastable polymorphs distinct from the stable polymorph, corundum, or  $\alpha$ - $\text{Al}_2\text{O}_3$ . These metastable polymorphs are described as transition aluminas, as they are phases present during the transition from an aluminum hydroxide (boehmite) or aluminum oxyhydroxide (bayerite) to corundum.<sup>46</sup> The dehydration of boehmite follows the series:



The dehydration of bayerite follows the series:



Corundum is based on the hexagonal close packing of oxygen, whereas  $\gamma$ ,  $\eta$ ,  $\delta$  and  $\Theta$  are all based on face centered anion packing. All but  $\Theta$  are based on the spinel structure, with their specific cation arrangement differentiating them from one another. Theta alumina has been assigned a monoclinic cell with the space group  $C2/m$ , with four formula units per cell.<sup>45</sup>

The  $\gamma$ -alumina phase is described as a disordered, defective member of the spinel structure. Written as a spinel typically is, the formula of  $\gamma$ -alumina is  $\text{Al}_{(8/3)}\text{O}_4$ . Some manner of charge compensation is necessary for  $\text{Al}_{(8/3)}\text{O}_4$  to be in the spinel structure, typically ascribed to  $V''_{tet}$ . The exact structure of  $\gamma$ -alumina is controversial. Various methods show that the occupancy of non-spinel sites is necessary to reproduce the characteristics of  $\gamma$ -alumina. However other methods give satisfying results while only occupying spinel sites, usually showing a preference for tetrahedral vacancies over octahedral vacancies.<sup>47</sup> The structure of  $\delta$ - $\text{Al}_2\text{O}_3$  is poorly understood, usually described as  $\gamma$ - $\text{Al}_2\text{O}_3$  with a degree of vacancy ordering which produces superstructure lines in a diffraction pattern.<sup>47</sup>

The structures of all the transition aluminas but  $\Theta$  are regarded as highly controversial. Much of the controversy arises from the fact that by their very nature, the transition aluminas are poorly crystalline, making exact structure solutions difficult. Also, phase progression from one transition alumina to another is a continuous, rather than a discrete process. It has been shown that there is not one exact temperature of

transition to move from one polymorph to another, but a lower temperature sustained for a longer time will still produce a transformation.<sup>48</sup>

### **K. Connection Between Metastable Spinel and the Transition Aluminas**

An understanding of transition aluminas is important as it is a system similar to the transformation of a metastable spinel to  $\Theta$ - $\text{Al}_2\text{O}_3$  and corundum. In particular,  $\gamma$ - $\text{Al}_2\text{O}_3$  assumes the spinel structure, with poor crystallinity and a large number of defects, with  $\delta$ - $\text{Al}_2\text{O}_3$  believed to be closely related to the structure of  $\gamma$ - $\text{Al}_2\text{O}_3$  but with ordered vacancies that result in superstructure lines. The “A”, “B”,  $\epsilon$ ,  $\delta_3$  and  $\phi$  metastable spinels may be regarded as a family of structures similar to  $\delta$ - $\text{Al}_2\text{O}_3$  in that they are the transition structures between a spinel structure and corundum. The manner of defects in  $\delta$ - $\text{Al}_2\text{O}_3$  are not completely clear, while the metastable spinels contain well-defined, but complex periodic antiphase boundaries, which essentially impart a superstructure of vacancy pairs.

### **L. Nickel Crystallite Shape**

The shape of the nickel metal crystallites is important for catalytic applications. Points on a crystal are known to be more catalytically active than facet edges, which are more active than crystal planes.

Surface faceting is a means of surface energy minimization, whereby planes with low surface energy take up a greater surface area of the particle, reducing or eliminating entirely the area taken up by planes with a greater surface energy. Meltzmann et al.<sup>49</sup> investigated the equilibrium crystal shape of nickel metal by dewetting a nickel metal thin film deposited on a sapphire substrate via annealing at 1300 or 1350 °C in a  $\text{H}_2$  atmosphere to form equilibrated nickel crystallites. The (111) and (100) planes were found to be the lowest energy surfaces by their extent in the equilibrium morphology. The equilibrium shapes obtained were not too different from spherical, with the closest descriptor being an under inflated soccer ball.

## EXPERIMENTAL PROCEDURE

### A. Spinel Synthesis

Appropriate amounts of NiO (97%, Acros Organics), Mg(OH)<sub>2</sub> (99%, Fisher Scientific),  $\alpha$ -Al<sub>2</sub>O<sub>3</sub> (99%, Fisher Scientific), ZrO(NO<sub>3</sub>)<sub>2</sub>·6H<sub>2</sub>O (99%, Aldrich Chemistry) were batched to form NiAl<sub>2</sub>O<sub>4</sub>, Ni<sub>0.75</sub>Mg<sub>0.25</sub>Al<sub>2</sub>O<sub>4</sub>, Ni<sub>0.5</sub>Mg<sub>0.5</sub>Al<sub>2</sub>O<sub>4</sub>, Ni<sub>0.25</sub>Mg<sub>0.75</sub>Al<sub>2</sub>O<sub>4</sub>, and MgAl<sub>2</sub>O<sub>4</sub>, all with 2.5 weight percent ZrO<sub>2</sub>. TiO<sub>2</sub> and Nb<sub>2</sub>O<sub>5</sub> containing NiAl<sub>2</sub>O<sub>4</sub> compositions were also synthesized. The TiO<sub>2</sub> and Nb<sub>2</sub>O<sub>5</sub> were both added as oxides to give 2.5 wt% of the total batch. This gives 3.55, 5.36, and 1.68 mole percent of ZrO<sub>2</sub>, TiO<sub>2</sub>, and Nb<sub>2</sub>O<sub>5</sub> respectively. Thermogravimetric analysis was performed on each raw material to determine loss on ignition, which was then accounted for in batching calculations. Each batch was vibratory milled for 30 minutes in deionized H<sub>2</sub>O with Al<sub>2</sub>O<sub>3</sub> media in plastic jars. Zirconyl nitrate is water soluble, so deionized water was chosen as the milling medium to ensure a homogenous distribution throughout the batch.

After milling, the slurry was dried overnight in an oven, mixed in an alumina mortar and pestle, and then calcined for 8 hours at 1500 °C in an electric furnace, using a heating rate of 5 K/min. After an 8 hour dwell, the furnace was allowed to cool to room temperature at a rate no faster than 5 °C/min. The calcined powders were then hand ground in an alumina mortar and pestle and passed through a U.S. number 50 sieve, with an opening size of 297  $\mu$ m. X-ray diffraction analysis showed the calcined batches to consist of single phase spinel with small amounts of tetragonal and monoclinic ZrO<sub>2</sub>, with the exception of a small amount of NiO, ~ 0.5 wt%, detected in the NiAl<sub>2</sub>O<sub>4</sub> + 2.5 wt% ZrO<sub>2</sub> composition.

### B. Closed System Reduction

In early sample reductions, the sample mass in the alumina tube furnace was not strictly controlled. This led to inconsistencies with regard to the refined nickel metal content of the reduced samples due to the depletion of H<sub>2</sub>. To eliminate possible sources of variation, strict process controls were instituted for all reduction runs from which data

is reported. A mass of  $3.30\text{g} \pm 0.001\text{g}$ , for each composition  $x = 0.25, 0.50, 0.75,$  and  $1,$  for  $\text{Ni}_x\text{Mg}_{1-x}\text{Al}_2\text{O}_4$  was placed in the furnace for every run, in high alumina crucibles (CoorsTek), on an alumina setter plate. The position of the samples in the furnace was reproduced from run to run by means of a measuring stick. The furnace was then closed and a vacuum started. When the pressure reached the lower limit of the capacitance manometer used ( $0.1$  Torr), the furnace began heating at  $3\text{K}/\text{min}$  to the target reduction temperature. When the target reduction temperature was reached,  $300 \pm 3$  Torr of ultra-pure  $\text{H}_2$  gas was applied to the system, monitored by means of a capacitance manometer. The furnace temperature was regulated by an S-type thermocouple in an alumina tube placed just above the sample position. The thermocouple was pushed into the tube snugly at the beginning of the temperature dwell to ensure that the thermocouple bead was tight against the alumina tube. A dwell time corresponding to each reduction temperature was then started after the  $\text{H}_2$  was introduced to the system, per Table III. In the absence of any strong indicators to suggest appropriate dwell times for each reaction temperature, HTXRD measurements were performed in  $20$  ml/min flowing  $4\%$   $\text{H}_2/\text{N}_2$ . The reduction times chosen were the amount of time until the nickel metal reflection stopped increasing in intensity. These times were determined in an earlier study using the  $\text{Ni}_x\text{Mg}_{1-x}\text{Al}_2\text{O}_4$  solid solution series without a  $\text{ZrO}_2$  additive.<sup>34</sup>

Table III. Dwell Times Used for Each Reduction Temperature

Reduction Temperature ( $^{\circ}\text{C}$ )	Dwell Time (hours)
650	94
700	51
750	29
800	24
850	24
900	12
950	12
1000	12
1100	12

At the end of the dwell, the furnace was allowed to cool to room temperature at a rate no greater than 3 K/min, with no change made to the furnace atmosphere. Upon cooling to room temperature, the furnace was opened, and the samples were removed. The powder packs tended to be lightly consolidated, with the degree of consolidation increasing with the total amount of reduction experienced. In all cases, light pressure with a metal spatula was sufficient to pulverize the powder pack. The reduced spinels were then hand ground in an alumina mortar and pestle and passed through a U.S. number 50 sieve. Only as much grinding as was necessary to pass the reduced spinels through the sieve was done. Two sets of samples were reduced at both 800 °C and 950 °C to assess the reproducibility of the reduction.

### **C. Isothermal TGA/DTA**

Isothermal thermogravimetric analysis, differential thermal analysis measurements were carried out in a Setaram SETSYS Evolution, capable of 0.002  $\mu\text{g}$  resolution and 0.03  $\mu\text{g}$  noise RMS. The SETSYS Evolution uses background subtraction to provide more accurate results. To do this, a measurement is made with empty crucibles under the exact same conditions that will later be used with a sample. The mass and DTA signals from this measurement are then subtracted from subsequent measurements to remove any minor experimental artifacts from the data.

To avoid damaging the platinum components of the system with hydrogen, optional equipment was used. A W-Re TGA/DTA rod and furnace control thermocouple was used, along with 85  $\mu\text{l}$  W crucibles. The standard alumina furnace tube was replaced with an amorphous carbon tube. Powder, 76.1 – 80.2 mg, was loaded into one W crucible, leaving the other crucible in the instrument empty. The system was then evacuated with a roughing pump to approximately 0.40 mbar, then filled with ultra-pure helium at a flow rate of 200 ml/min. Once the pressure in the furnace had risen to atmospheric, the flow of helium was reduced to 20 ml/min. Once the mass signal had stabilized from the change in flow rate, the measurement began. The system ramped at 15 K/min to 150 °C, and dwelled for 20 minutes to remove any adsorbed moisture. After that dwell, the furnace was ramped at 10 K/min to 1000 °C, with the sample temperature tending to overshoot by 7 °C and remain there. After a one hour hold at 1000 °C in

20ml/min flowing helium, the gas flow was switched to 20ml/min of 4% H<sub>2</sub> in argon. Dwell time at 1000 °C was 16 or 40 hours. A 16 hour dwell time experiment was conducted for every sample composition, with an additional experiment with a 40 hour dwell time being used for NiAl<sub>2</sub>O<sub>4</sub> + 2.5 wt% ZrO<sub>2</sub> and Ni<sub>0.75</sub>Mg<sub>0.25</sub>Al<sub>2</sub>O<sub>4</sub> + 2.5 wt% ZrO<sub>2</sub>, as their mass losses did not reach a constant minimum mass during the 16 hour dwell, as the other compositions had. A mass of 126.7 and 109.2 mg was used for NiAl<sub>2</sub>O<sub>4</sub> + 2.5 wt% ZrO<sub>2</sub> and Ni<sub>0.75</sub>Mg<sub>0.25</sub>Al<sub>2</sub>O<sub>4</sub> + 2.5 wt% ZrO<sub>2</sub> respectively, so the reaction rates cannot be directly compared to those of the 16 hour dwell time experiments, which used a smaller sample mass. Argon was used for the diluent gas in this experiment rather than nitrogen as in the HTXRD measurements, due to the concern of forming carbonitride on the amorphous carbon furnace tube.

The mass change that occurred prior to the introduction of hydrogen was added to the initial sample mass such that samples were normalized to 100% mass at the time of the introduction of the hydrogen. This was done to account for any non-spinel or zirconia mass (adsorbed moisture or gas) in the sample at the time of loading so that mass loss percentages would be accurate. The amount of this correction was always small, never exceeding 0.5 mg (0.65 mass %). The final mass measurement while under helium was used for this calculation rather than the first measurement under hydrogen, as the switching of gases sometimes caused a momentary disturbance in the mass signal.

The samples from the isothermal TGA/DTA measurements were retained for analysis by He pycnometry and X-ray diffraction on a zero background holder, such that extent of reduction as determined via weight loss and Rietveld refinement and density could be known simultaneously to give a better understanding of the behavior of the material.

Spinel which had already been somewhat reduced were also subjected to the previously mentioned isothermal schedule. Spinels of each ZrO<sub>2</sub>-containing composition reduced at 950 and 1100 °C for 12 hours in the closed system furnace in 300 Torr pure H<sub>2</sub> were reduced such that the observed weight loss could be compared to that of the as-synthesized spinels to calculate their extent of reduction and their consequent nickel metal phase fraction. This was done to assess the accuracy of using the Rietveld refinement of the X-ray diffraction patterns to determine the nickel metal phase fraction.

#### D. Nonisothermal TGA/DTA

Nonisothermal TGA measurements were performed on NiO and the spinel solid solution compositions. Between 102 and 108 mg of sample was loaded into one W crucible, leaving the second crucible in the instrument empty. The process of pumping down the instrument and filling with helium was identical to the isothermal TGA measurements. The system ramped at 15 K/min to 200 °C and dwelled for 40 minutes to remove any adsorbed moisture or gases. After the 40 minute hold at 200 °C in 20ml/min helium, the gas flow was switched to 20ml/min of 4% H<sub>2</sub> in argon. The furnace was then ramped at 2.5 K/min to 1100 °C. Again, the mass change that occurred prior to the introduction of hydrogen was added to the initial sample mass such that masses were normalized to 100% mass at the time of the introduction of the hydrogen. Nonisothermal TGA experiments with a 1 K/min ramp rate were also performed on the spinel samples to assess if their apparent reduction onset temperature shifted with ramp rate. The 1 K/min experiments used a 15 K/min ramp rate to 750 °C and dwelled for 40 minutes. The 4% H<sub>2</sub> in argon flow was then started, and the furnace was ramped at 1 K/min to 1100 °C. The two heating programs are illustrated in Figure 3. Background subtraction was also used for both the 2.5 K/min and the 1 K/min ramp rate nonisothermal reductions by performing a measurement with both sample crucibles empty.

Temperature calibration of the instrument was performed with the use of the NIST DTA temperature standards K<sub>2</sub>SO<sub>4</sub>, BaCO<sub>3</sub>, SrCO<sub>3</sub>, and KClO<sub>4</sub>, covering a temperature range of 295 to 925 °C.

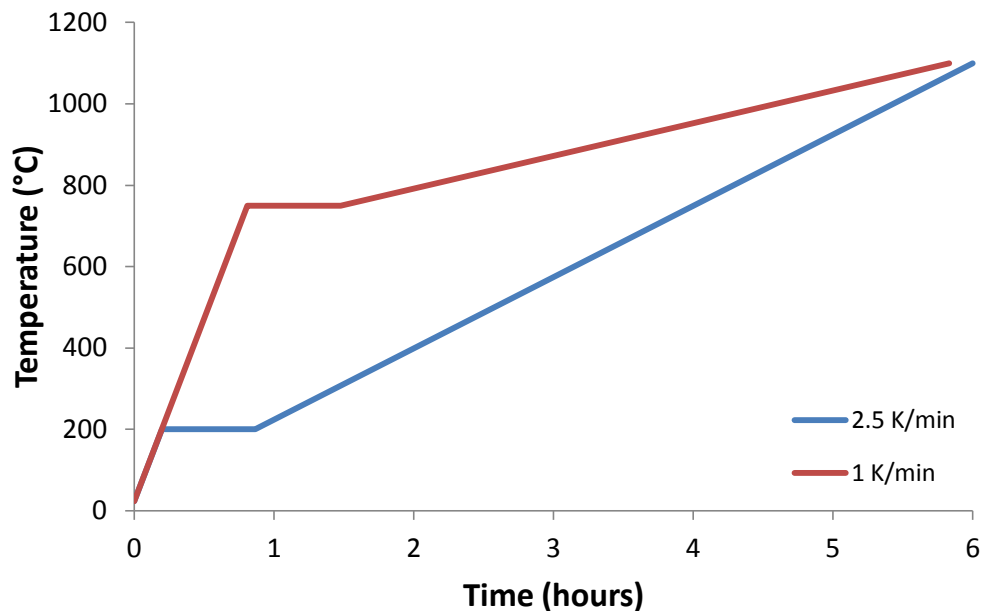


Figure 3. Heating programs used in the nonisothermal TGA measurements. He was flowing until the end of the dwell, 20 ml/min 4% H<sub>2</sub>/Ar was started thereafter.

### E. Helium Pycnometry

Density measurements were performed using a Micromeritics AccuPyc II 1340 gas displacement density analyzer with a 1 cm<sup>3</sup> sample chamber. To perform the helium pycnometry measurement, a quantity of powder was weighed and inserted into the analysis chamber. The analysis chamber was evacuated and purged with helium five times, then raised to a set pressure with helium. When stability in the pressure reading was achieved, the analysis chamber was opened to an evacuated reference volume. The volume of the sample can then be calculated, and used to calculate the sample density. After the first measurement, the chamber was evacuated and the process repeated for a total of five measurements, which were then averaged.

The densities of the spinel samples isothermally reduced in the TGA for 40 or 16 hours at 1000 °C in 20 ml/min flowing 4% H<sub>2</sub>/Ar were measured using an insert in the chamber to reduce its volume to 0.1 cm<sup>3</sup>. The smaller chamber volume allows for more accurate density determinations when using the small amounts of sample.

A calibration procedure was performed by making a volume measurement with the chamber empty, and with a steel ball of a well determined volume in it. The pressure determinations from these two measurements define the zero volume pressure and the pressure at the volume of the steel ball. The  $0.1 \text{ cm}^3$  insert is calibrated by performing a volume measurement on the insert after the pycnometer has been calibrated by the above process. The measured volume of the insert is then subtracted from the sample chamber volume, giving the free volume of the chamber with the insert in place.

Initially, samples were dried overnight in an oven prior to pycnometric measurement, but it was found that drying the samples made no difference to the measured density. Later samples were not dried.

#### **F. Room Temperature X-ray Diffraction**

X-ray diffraction was performed in Bragg-Brentano geometry on unreduced and reduced spinel samples using thick mount powder specimens. Patterns were obtained on a Bruker D8 Advance diffractometer using  $\text{Cu-K}_\alpha$  radiation, a  $2.5^\circ$  Soller slit, a 15 mm incident beam variable slit, 30 rotations per minute in-plane spinning, a Ni foil  $\text{K}_\beta$ -filter, and a LynxEye position sensitive detector with a range of  $2.946^\circ 2\Theta$ , using a step size of  $0.014^\circ 2\Theta$ , and a count time of 1.5 seconds from  $10$  to  $140^\circ 2\Theta$ .

X-ray diffraction measurements were performed on the spinels reduced in the 16 and 40 hour dwell  $1000^\circ\text{C}$  isothermal TGA experiments using the same parameters, except a zero background sample holder and 5mm incident beam variable slit were used due to the smaller amount of sample.

#### **G. High Temperature X-ray Diffraction in Flowing 4% $\text{H}_2/\text{N}_2$**

High temperature X-ray diffraction in flowing  $4\%\text{H}_2/\text{N}_2$  was performed in a modified Siemens D5000 diffractometer.<sup>50</sup>  $\text{Cu-K}_\alpha$  radiation was used, with a VÅntec-1 position sensitive detector, covering  $12^\circ 2\Theta$ . Samples were ground with a YSZ mortar and pestle in isopropanol and deposited onto platinum coated sapphire sample holders. Scan parameters were  $15$  to  $80^\circ 2\Theta$ , with a scan rate of  $5.86^\circ 2\Theta/\text{minute}$ . A step size of  $0.022^\circ 2\Theta$  was used with a count time of  $0.23 \text{ s/step}$ , for a time of 11 minutes and 5

seconds per pattern. A 20 ml/min flow of 4% H<sub>2</sub>/N<sub>2</sub> was used throughout the measurement. A pattern was recorded at 30 °C, followed by heating the furnace at 10.2 K/min to 600 °C, followed by a 30 minute dwell, then a pattern was recorded. The same heating rate and dwell time were used for subsequent measurements, stepping 50 °C at a time to 1100 °C. After the 1100 °C pattern, the furnace was allowed to cool at a rate of 60 K/min. During cooling, the furnace was equilibrated at 900, 700, 500, and 300 °C to record a pattern, and a final pattern was recorded after cooling to 30 °C. These parameters were used for the NiAl<sub>2</sub>O<sub>4</sub> + 2.5 wt% additive series.

Patterns were obtained for the Ni<sub>x</sub>Mg<sub>1-x</sub>Al<sub>2</sub>O<sub>4</sub> series starting at 700 °C and stepping 100 °C to a maximum temperature of 1300 °C. The first pattern obtained, NiAl<sub>2</sub>O<sub>4</sub> + 2.5 wt. % ZrO<sub>2</sub>, used Co radiation before the system was switched to Cu radiation permanently. This set of experiments used a flow rate of 200 ml/min of 4% H<sub>2</sub>/N<sub>2</sub>.

## H. Rietveld Refinement with TOPAS

Rietveld structure refinements were performed with Bruker Total Pattern Analysis Solution software (TOPAS).<sup>51</sup> Diffraction patterns for the unreduced spinels, closed system reduced spinels, and isothermally reduced in TGA spinels were collected on the Bruker D8 Advance with the use of a variable incident beam slit and a position sensitive detector. TOPAS software is only capable of correcting for one of these factors, so the intensities were converted to simulated fixed slit intensities by using a filter in the JADE software package (Materials Data Inc.). Each data set was also adjusted by reducing all intensities by a factor sufficient give a realistic value for R<sub>exp</sub>, the statistically expected residual.

The fundamental parameters peak shape approach was used. An eight term Chebychev polynomial was used to fit the background. The Linear PSD instrumental effects were used, with a 2 $\Theta$  angular range of the PSD of 2.946, and a virtual Fixed Diffraction Slit angle of 0.472918, which was determined by refinement of SRM 640d. The Simple Axial Model was used for the Axial Convolution, with a fixed value of 5.50 mm, as that value suitably matched the low angle peak shape of all collected patterns. Sample displacement was refined for all patterns. Lorentz polarization effects were

accounted for with a value of 0 for the LP factor, corresponding to no monochromator. No preferred orientation, absorption, or surface roughness corrections were found necessary. If any pattern exhibited a reflection at the  $140^\circ 2\theta$  upper limit collected, that region was excluded from the refinement.

Lattice constants were refined for all phases, as were Lorentzian crystallite size and microstrain broadening terms. A maximum crystallite size constraint of 2000 nm, and a minimum constraint of 20 nm were used for all phases. Above approximately 2000 nm, a further increase in crystallite size was found to have no perceptible effect on the calculated peak broadening. It was seen as desirable to enter a maximum crystallite size constraint such that seeing a refined crystallite size at that value made it apparent that the upper limit had been reached, rather than having an arbitrarily large value with a large standard deviation and no real physical significance. A 20 nm minimum constraint was used to prevent the Ni metal phase from refining to a value where it became so broad that it was really only contributing to the background. This constraint was used as it was desirable to have the Ni metal phase refining for all reduced spinel samples, including those where the extent of reduction was low enough such that the Ni metal peak had not yet distinguished itself from the background. A minimum constraint of 0 and a maximum constraint of 1 were applied for microstrain broadening to prevent the refinement from arriving at values with little physical significance.

### **1. $\text{Ni}_x\text{Mg}_{1-x}\text{Al}_2\text{O}_4$ Model**

The spinel model used space group  $\text{Fd}\bar{3}\text{mZ}$ , International Crystallographic Tables number 227. The model for the reduced spinel began with the lattice parameter, crystallite size, strain, and O parameter of the resultant refinement of the unreduced specimen of the same composition.

The tetrahedrally and octahedrally coordinated cation positions were not refined, as they are special positions located at  $x = 0.125$ ,  $y = 0.125$ ,  $z = 0.125$ , and  $x = 0.5$ ,  $y = 0.5$ ,  $z = 0.5$ , respectively. The oxygen parameter,  $u$ , was refined, constrained to be along the [111] direction in keeping with the general position, via the constraint  $x = y = z$ . The oxygen parameter would sometimes refine to the very unrealistic value of  $\sim 0.02$ , giving a very poor refinement, but the refinement was unable to correct itself, and a manual adjustment was needed to continue with the refinement. To avoid this, a minimum

constraint of 0.22 was placed on the oxygen parameter. A value of 0.22 is unrealistically low, but the refinement was able to recover by itself if it reached that value. No maximum constraint was deemed necessary, as the oxygen parameter never rose to such a value that the refinement failed.

Thermal parameters were refined for the spinel sites, with all tetrahedral site atoms constrained to have the same thermal parameter, and the thermal parameter of all octahedral atoms likewise constrained to be the same.

Atomic occupancies for the spinel were refined with the use of constraints. The occupancy of any atom on the tetrahedral site was allowed to refine freely. The octahedral nickel occupancy was also allowed to refine freely. The octahedral Al and Mg occupancies were constrained via the total nickel occupancy accounting for multiplicity, and the value for Al or Mg respectively on the tetrahedral site. The total Al and Mg were constrained to give a constant ratio with respect to each other, and to increase their occupancies accordingly to charge compensate for a decrease in the total nickel occupancy, keeping the oxygen site occupancy constant at 1. Figures 4 and 5 illustrate the allowed values of spinel stoichiometry under the constraint equations shown in Table IV. Although the lines for each composition are shown ending at  $x$  in  $\text{Ni}_x\text{Mg}_{1-x}\text{Al}_2\text{O}_4$  for each composition, no maximum constraint was used for the total amount of nickel. Any such maximum constraint would be circular given the other requirements of the model.

Table IV shows the equations used to constrain the octahedral site occupancies. The constraints account for the octahedral site having twice the multiplicity of the tetrahedral site, 16 and 8 respectively

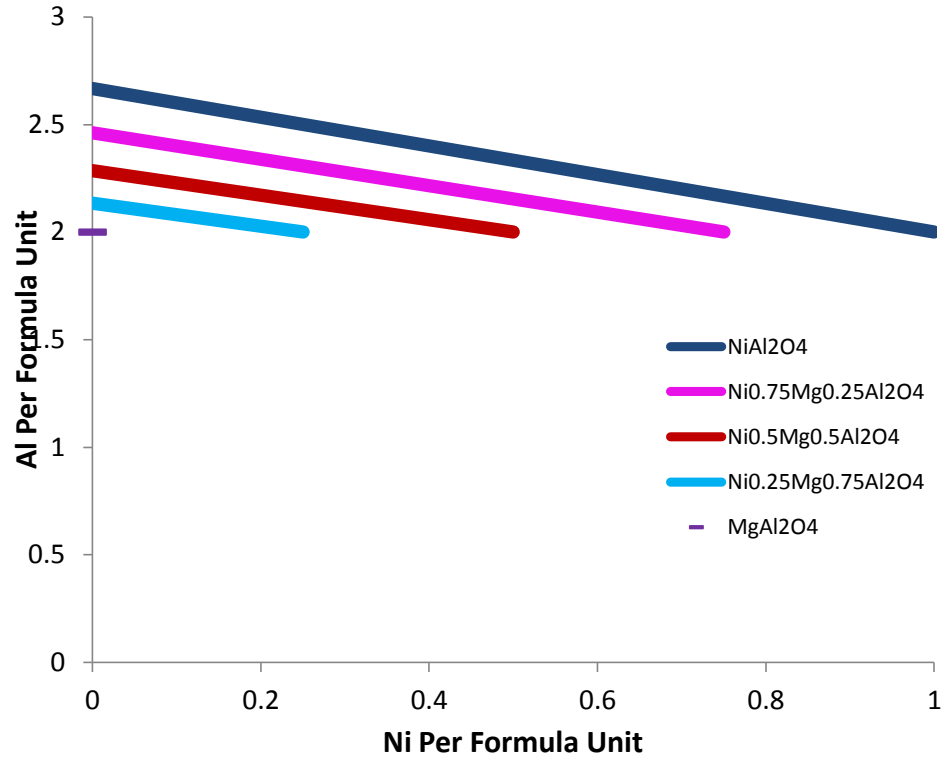


Figure 4. Illustration of the allowed combinations of nickel and aluminum per formula unit for each spinel composition. These allowed combinations were used to constrain the spinel stoichiometry to maintain charge neutrality and a constant Mg/Al ratio.

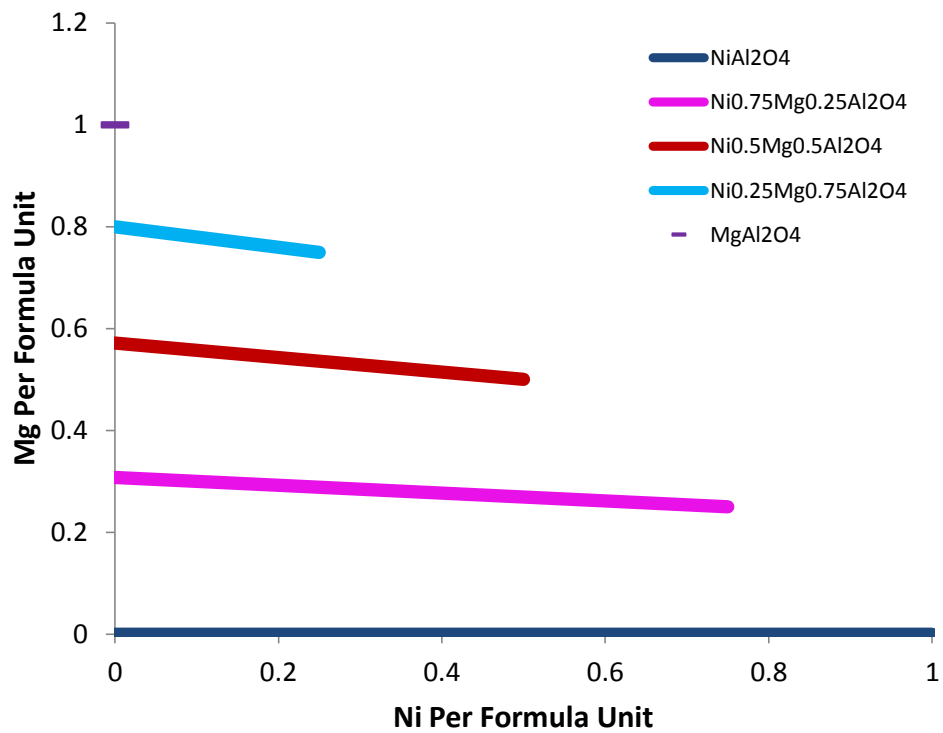


Figure 5. Illustration of the allowed combinations of nickel and magnesium per formula unit for each spinel composition. These allowed combinations were used to constrain the spinel stoichiometry to maintain charge neutrality and a constant Mg/Al ratio.

Table IV. Occupancy Constraints Used in the Refinement of  $\text{Ni}_x\text{Mg}_{1-x}\text{Al}_2\text{O}_4$

	Tetrahedral Site			Octahedral Site			Oxygen
Multiplicity	8			16			32
Ion	$\text{Ni}^{2+}$	$\text{Mg}^{2+}$	$\text{Al}^{3+}$	$\text{Ni}^{2+}$	$\text{Mg}^{2+}$	$\text{Al}^{3+}$	$\text{O}^{2-}$
Occupancy Constraint	"Ni"	"Mg"	"Al"	"Ni2"	$\frac{(1-x)\left(\frac{4}{4-x}\right) - \left(\frac{(1-x)\frac{4}{4-x}}{1-x}\right)(\text{Ni} + 2 * \text{Ni}2) - \text{Mg}}{2}$	$\frac{2\left(\frac{4}{4-x}\right) - \left(\frac{2\frac{4}{4-x}}{1-x}\right)(\text{Ni} + 2 * \text{Ni}2) - \text{Al}}{2}$	Fixed at 1

## 2. Nickel Metal Model

The nickel metal model used space group Fm-3m, International Crystallographic Tables number 225. The starting lattice parameter used was 5.250Å, with 200 nm crystallite size, and 0.1 Lorentzian microstrain broadening. The atomic position and occupancy were not refined. The thermal parameter was fixed at 1.

In the samples with a higher extent of reduction, a shoulder on the low angle side becomes evident on the nickel metal reflections, as can be seen in Figure 6. In the absence of an adequate physical model to account for this intensity, a tangent  $\Theta$  dependent hat function convolution was added to the nickel metal structure refinement. The hat function was chosen solely for its ability to fit the shoulder more accurately than alternative choices. It was necessary to satisfactorily fit the peak shape in order to include all the intensity from the nickel in the model, so other refined structural changes could accurately be indexed against the extent of reduction. If the low angle shoulder was not included in the model, the refined nickel metal phase fraction would become progressively less accurate with the higher extent of reduction samples.

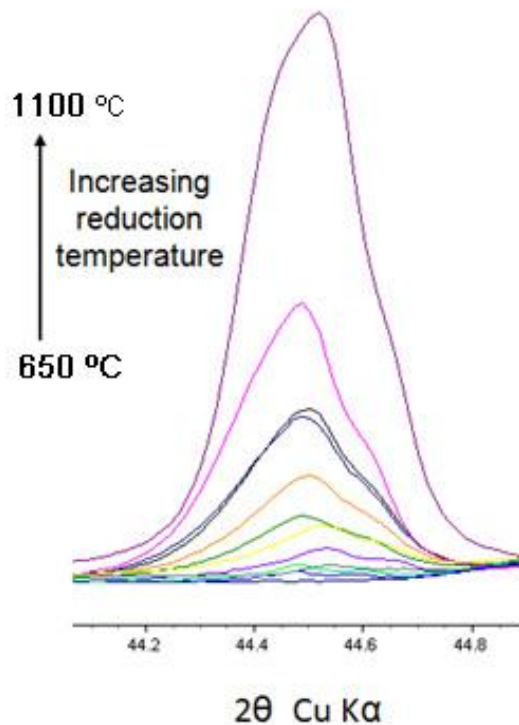


Figure 6. Room temperature XRD patterns from  $\text{NiAl}_2\text{O}_4 + 2.5 \text{ wt\% ZrO}_2$  reduced at temperatures 650 °C to 1100 °C in 300 Torr  $\text{H}_2$ . The (111) reflection of Ni metal is shown to demonstrate the low angle shoulder, which was present on all the nickel metal reflections.

### 3. Zirconia Models

Reflections from both monoclinic  $\text{ZrO}_2$ , referred to as baddeleyite, and tetragonal  $\text{ZrO}_2$  were present in the unreduced and reduced spinels. Starting lattice parameters used in the refinement for the  $\text{ZrO}_2$  phases are given in Table V. Thermal parameters were fixed at 1 for both  $\text{ZrO}_2$  models. Only the lattice parameters, Lorentzian crystallite size broadening, and Lorentzian microstrain broadening were refined for the  $\text{ZrO}_2$  models. No atomic positions, occupancies, or thermal parameters were refined.

Table V. Starting Structural Parameters Used in the ZrO<sub>2</sub> Models

	Baddeleyite	Tetragonal ZrO <sub>2</sub>
Space Group	P121/c1	P42/nmc
a	5.149	3.599
b	5.219	-
c	5.318	5.196
$\beta$	99.05	-
Crystallite Size	200	1216
Microstrain	0.25	0.125

### I. Standard Voltage Scanning Electron Microscopy

All standard voltage electron micrographs were obtained with an FEI Quanta 200F Environmental Scanning Electron Microscope. All samples were dispersed onto carbon planchets with acetone and carbon coated.

### J. Low Voltage Scanning Electron Microscopy

Low-voltage electron micrographs were obtained on a Hitachi S-3400 variable pressure SEM, from 0.2 – 6 kV. No conductive coating was necessary.

### K. TEM

TEM investigations were performed using a Hitachi HF-3300 cold FE-STEM/TEM at the ShaRE User facility at Oak Ridge National Lab. One initial sample was reduced powder, which was too thick to be electron transparent, but EDS maps were collected. Subsequent specimens were made electron beam transparent via cutting them into thin sections with a focused ion beam.

## **L. Powder Cross Sections**

Powder cross sections were obtained by suspending a portion of reduced powder in thermoset epoxy, approximately five volume percent. The sample mounts were then ground and polished, starting with 300 grit SiC paper, and using progressively smaller sizes, ending with a 1  $\mu\text{m}$  polycrystalline diamond suspension. Mounts were then cleaned with acetone and carbon coated prior to imaging in the FEI Quanta 200F ESEM.

## RESULTS AND DISCUSSION

### A. Rietveld Refinement of X-ray Diffraction Data

As shown in Figure 7 the lattice parameters of the intermediate members of the solid solution series,  $\text{Ni}_{0.75}\text{Mg}_{0.25}\text{Al}_2\text{O}_4$ ,  $\text{Ni}_{0.5}\text{Mg}_{0.5}\text{Al}_2\text{O}_4$ ,  $\text{Ni}_{0.25}\text{Mg}_{0.75}\text{Al}_2\text{O}_4$ , deviate from Vegard's Law behavior. However, this is not unexpected, as the degree of inversion of a spinel will cause deviations in the lattice parameter away from Vegard's Law behavior. In fact, the variation of the lattice parameter of the spinel with composition closely resembles that seen by Porta et al.,<sup>1</sup> who used X-ray diffraction to examine the variation of inversion with composition.

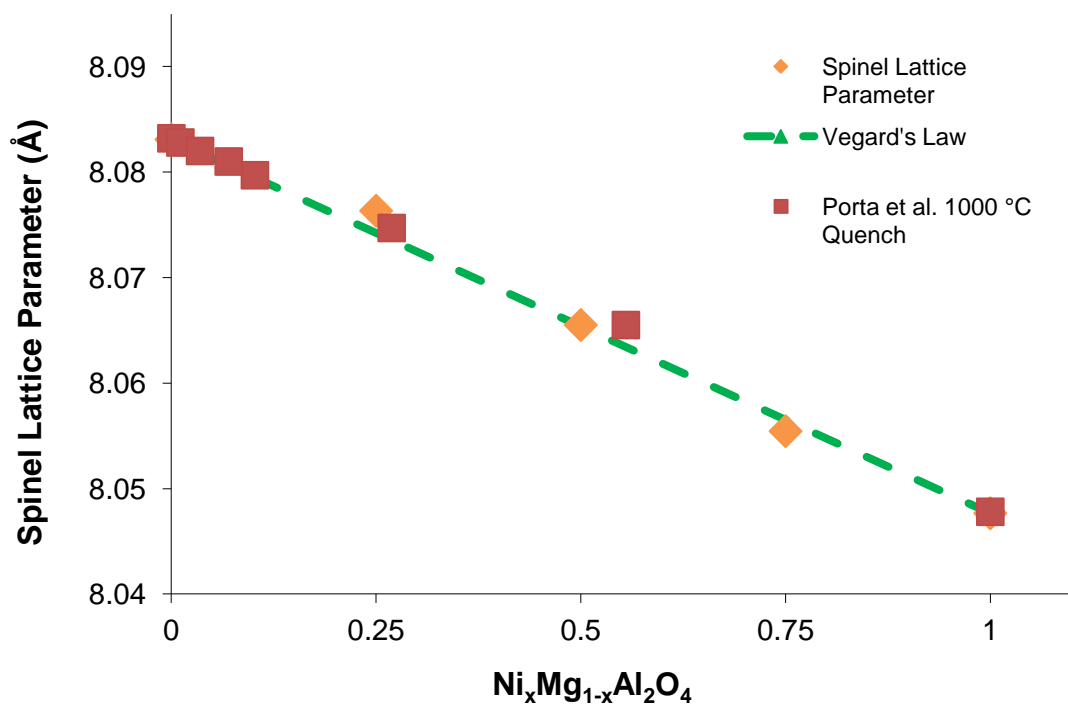


Figure 7. Refined lattice parameters for  $\text{Ni}_x\text{Mg}_{1-x}\text{Al}_2\text{O}_4$ . Error bars of one standard deviation are smaller than the data marker.

Figures 8 and 9 illustrate the complex changes in the spinel peak shape at different reduction temperatures. Of the patterns shown, metastable spinel phases are present in the  $\text{NiAl}_2\text{O}_4 + 2.5 \text{ wt\% ZrO}_2$  reduced at 950, 1000, and 1100 °C, and in  $\text{Ni}_{0.75}\text{Mg}_{0.25}\text{Al}_2\text{O}_4 + 2.5 \text{ wt\% ZrO}_2$  reduced at 900, 950, 1000, and 1100 °C. These results are summarized in Table VI. Although  $\text{Ni}_{0.75}\text{Mg}_{0.25}\text{Al}_2\text{O}_4$  is not stable after reduction at 900 °C while  $\text{NiAl}_2\text{O}_4$  is stable at 900 °C, this should not be misconstrued that  $\text{Ni}_{0.75}\text{Mg}_{0.25}\text{Al}_2\text{O}_4$  is less stable than  $\text{NiAl}_2\text{O}_4$ . This is instead due to the faster reduction kinetics of  $\text{Ni}_{0.75}\text{Mg}_{0.25}\text{Al}_2\text{O}_4$ , which achieved a greater extent of reduction in the 900 °C reduction sample set than did  $\text{NiAl}_2\text{O}_4$ . This is discussed in greater depth in the following sections.

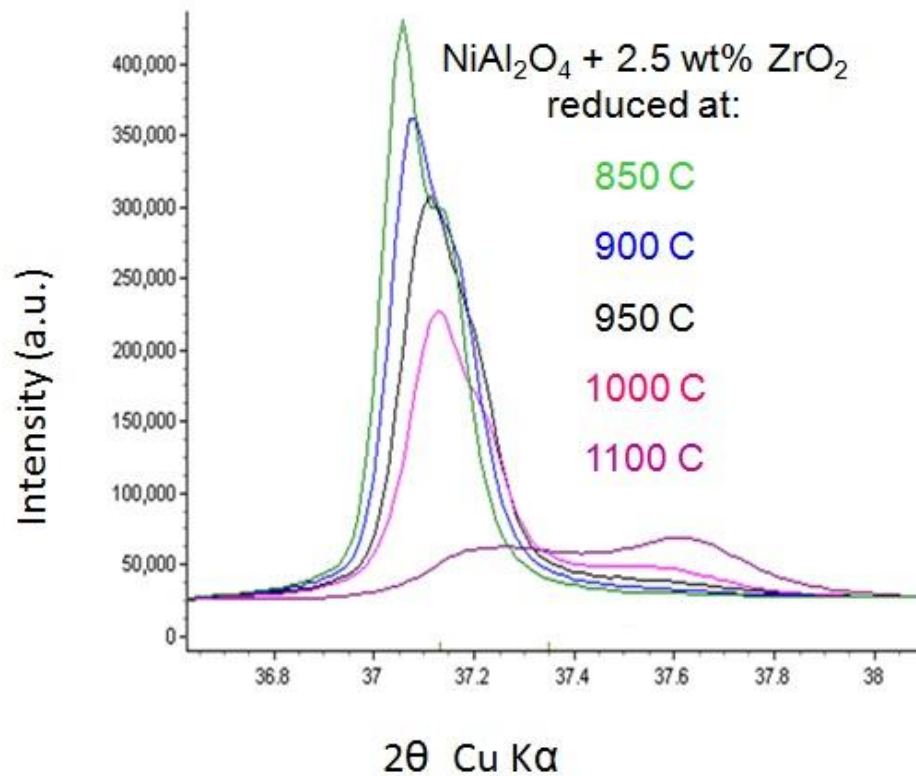


Figure 8. Room temperature X-ray diffraction patterns showing the (311) reflection of  $\text{NiAl}_2\text{O}_4$  after reduction at 850 – 1100 °C in 300 Torr  $\text{H}_2$  for 12 or 24 hours.

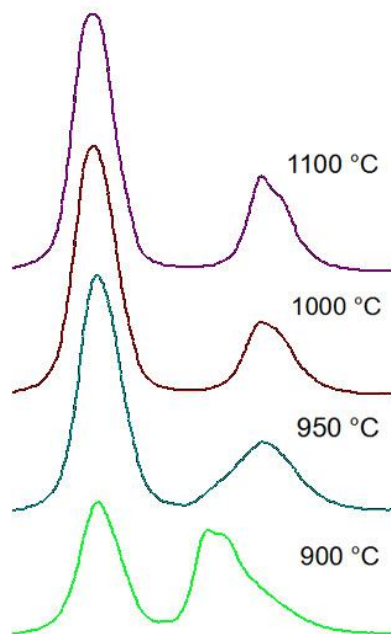


Figure 9. Room temperature X-ray diffraction patterns showing the nickel (111) and the (311) reflection of  $\text{Ni}_{0.75}\text{Mg}_{0.25}\text{Al}_2\text{O}_4$  after reduction at 900 – 1100 °C in 300 Torr  $\text{H}_2$  for 12 hours. The complex change in the spinel peak shape with increasing reduction is shown.

Table VI. Closed System Reduction Observed Phase Stability

Reduction Temperature (°C)	$\text{NiAl}_2\text{O}_4$	$\text{Ni}_{0.75}\text{Mg}_{0.25}\text{Al}_2\text{O}_4$	$\text{Ni}_{0.5}\text{Mg}_{0.5}\text{Al}_2\text{O}_4$	$\text{Ni}_{0.25}\text{Mg}_{0.75}\text{Al}_2\text{O}_4$
650	Stable	Stable	Stable	Stable
700	Stable	Stable	Stable	Stable
750	Stable	Stable	Stable	Stable
800	Stable	Stable	Stable	Stable
850	Stable	Stable	Stable	Stable
900	Stable	Unstable	Stable	Stable
950	Unstable	Unstable	Stable	Stable
1000	Unstable	Unstable	Stable	Stable
1100	Unstable	Unstable	Stable	Stable

Figure 10 shows the goodness of fit,  $R_{wp}/R_{exp}$ , of the Rietveld refinements of the closed system reduced spinels. Overall, good fits were obtained. The GOF of some of the refinements are less than 1 due to the scaling procedure used to reduce the maximum counts from the 200,000 – 400,000 which was obtained to the 20,000 – 30,000 for which the refinement statistics are designed. The high GOFs for  $Ni_{0.75}Mg_{0.25}Al_2O_4 + 2.5 \text{ wt\% ZrO}_2$  result from the peak splitting of the spinel phase in the 900 and 950 °C reductions. The high values for  $NiAl_2O_4 + 2.5 \text{ wt\% ZrO}_2$  are a result of a large amount of metastable spinel phase present, which was not modeled in the refinement.

Figures 11 through 14 show the refinement and difference pattern for one of the higher quality, and two of the lower quality fits respectively, with Figure 14 being a close up to show the spinel peak shape which resulted in a less satisfactory fit in the refinement shown in Figure 13.

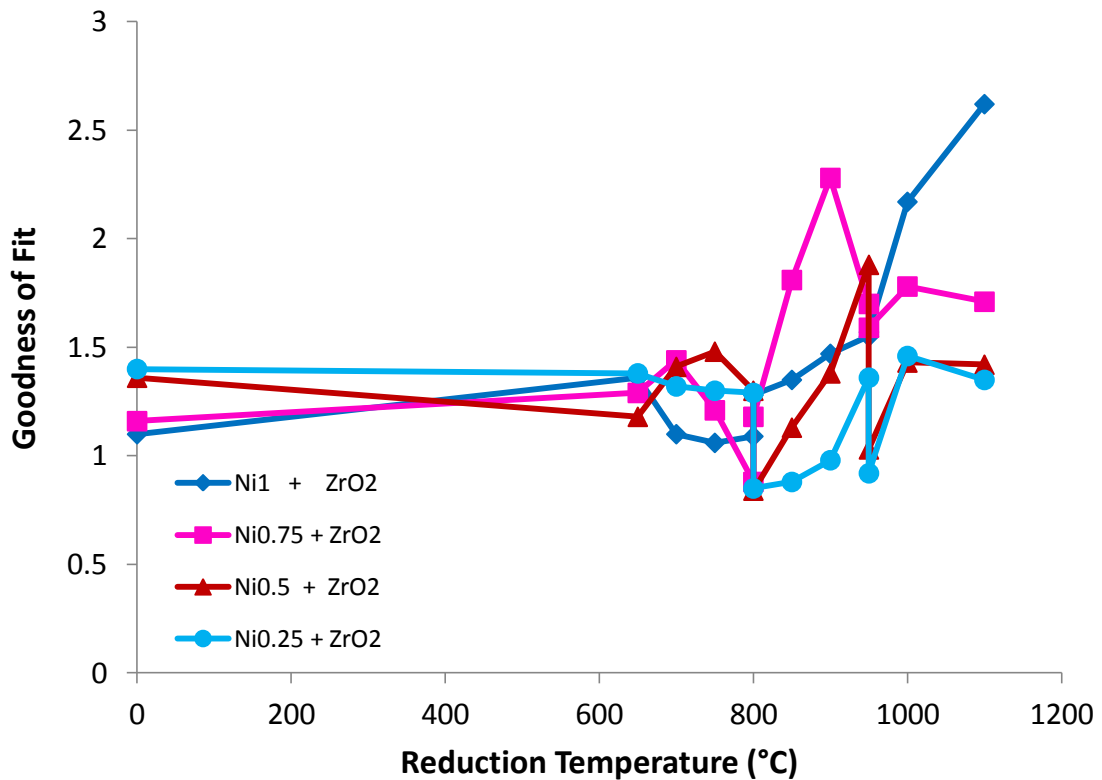


Figure 10. Goodness of fit for the Rietveld refinements of the closed system reduced spinels.

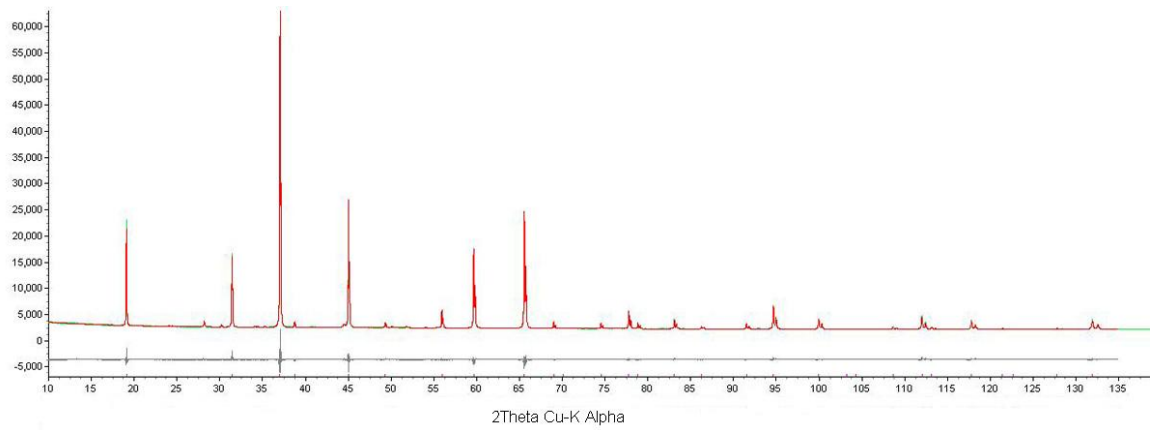


Figure 11. Refinement of  $\text{NiAl}_2\text{O}_4 + 2.5 \text{ wt\% ZrO}_2$  reduced at  $750 \text{ }^\circ\text{C}$  for 29 hours in 300 Torr  $\text{H}_2$ , showing a high quality fit.

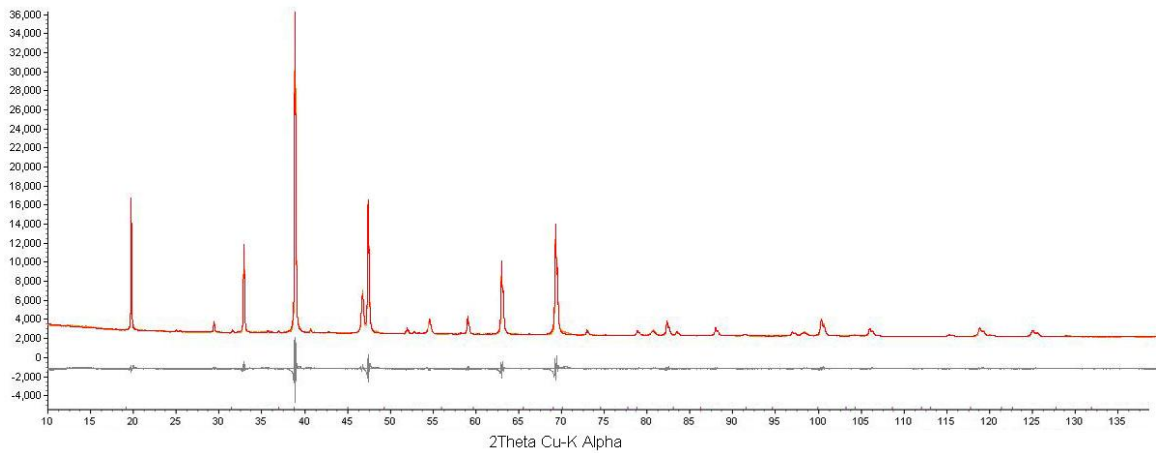


Figure 12. Refinement of  $\text{NiAl}_2\text{O}_4 + 2.5 \text{ wt\% ZrO}_2$  reduced at  $900 \text{ }^\circ\text{C}$  for 12 hours in 300 Torr  $\text{H}_2$ . A lesser quality fit was obtained due to difficulties with adequately modeling the peak shapes.

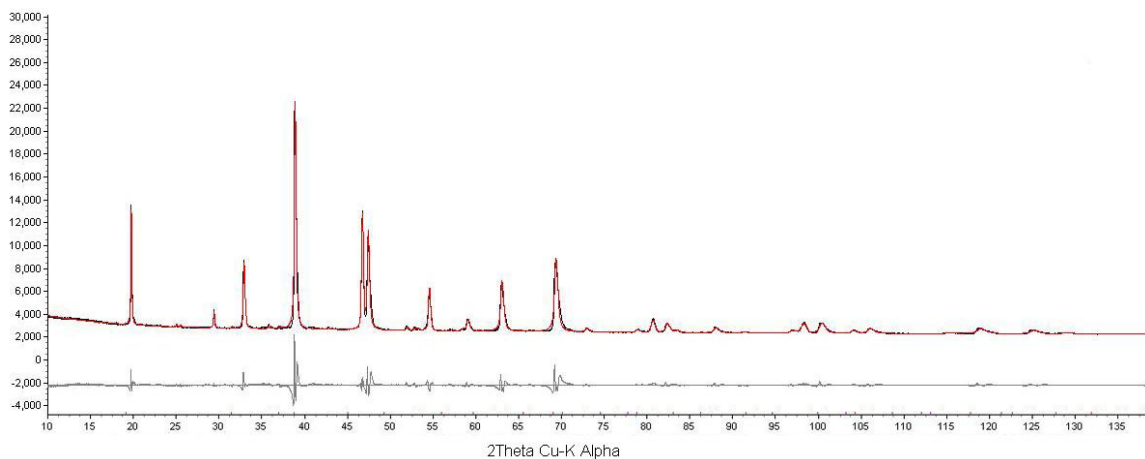


Figure 13. Refinement of  $\text{Ni}_{0.75}\text{Mg}_{0.25}\text{Al}_2\text{O}_4 + 2.5 \text{ wt\% ZrO}_2$  reduced at  $900 \text{ }^\circ\text{C}$  for 12 hours in 300 Torr  $\text{H}_2$ . Fit is relatively poor due to peak splitting in the spinel.

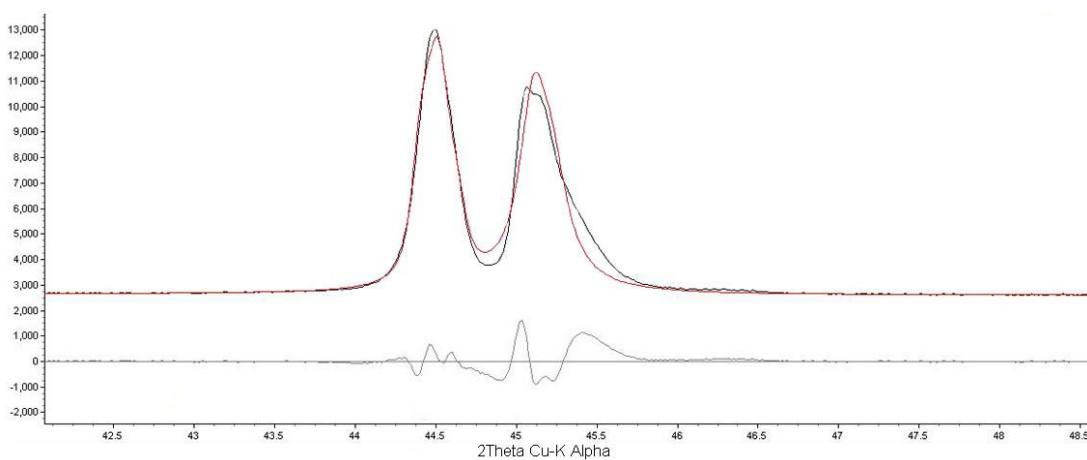


Figure 14. Refinement of  $\text{Ni}_{0.75}\text{Mg}_{0.25}\text{Al}_2\text{O}_4 + 2.5 \text{ wt\% ZrO}_2$  reduced at  $900 \text{ }^\circ\text{C}$  for 12 hours in 300 Torr  $\text{H}_2$ . Fit is relatively poor due to peak splitting in the spinel.

Figure 15 shows the refined total site occupancies for the tetrahedral and octahedral site in  $\text{NiAl}_2\text{O}_4 + 2.5 \text{ wt\% ZrO}_2$ . The behavior of the site occupancies in  $\text{NiAl}_2\text{O}_4 + 2.5 \text{ wt\% ZrO}_2$  is typical of all compositions. It was not possible to place a maximum site occupancy constraint due to technical reasons involving the spinel model used. The refined values of the total octahedral site occupancy start slightly higher than 1, and the total tetrahedral site occupancy starts slightly under 1. Both totals decrease as

the reduction proceeds, as the total number of cations decreases due to the relative increase of  $\text{Al}^{3+}$  and the formation of charge compensating cation vacancies.

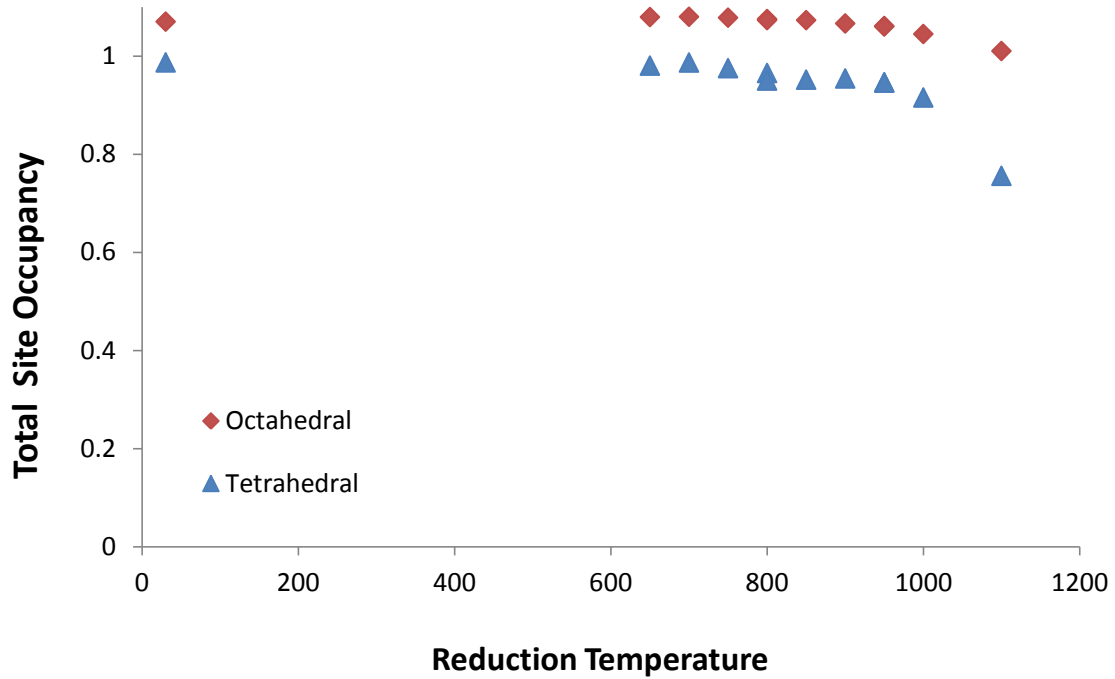


Figure 15. Refined total site occupancy of the octahedral and tetrahedral site for the closed system reduced  $\text{NiAl}_2\text{O}_4 + 2.5 \text{ wt\% ZrO}_2$ . This behavior is typical of the other compositions

Sickafus et al. have shown that there is good agreement when comparing the average cationic radii of a binary spinel to its lattice parameter,<sup>8</sup> but this agreement is shown over the lattice parameter range of  $8\text{\AA}$  to  $9.2\text{\AA}$ . Over the lattice parameter range of  $\text{MgAl}_2\text{O}_4$  to  $\text{NiAl}_2\text{O}_4$  of  $8.048$  to  $8.082 \text{\AA}$ , the observed lattice parameter variation fits well within the scatter shown by Sickafus. This comparison is made in Figure 16. It is tempting to ascribe the deviation of the solid solution compositions from Sickafus's fit to the error in the determination of the inversion of the spinel. Since tetrahedral and octahedral radii differ,<sup>12</sup> the inversion of the spinel affects the average cation radii. It is likely that the refined values of the spinel are correct, and this solid solution series deviates slightly from the behavior of the larger population of spinels.

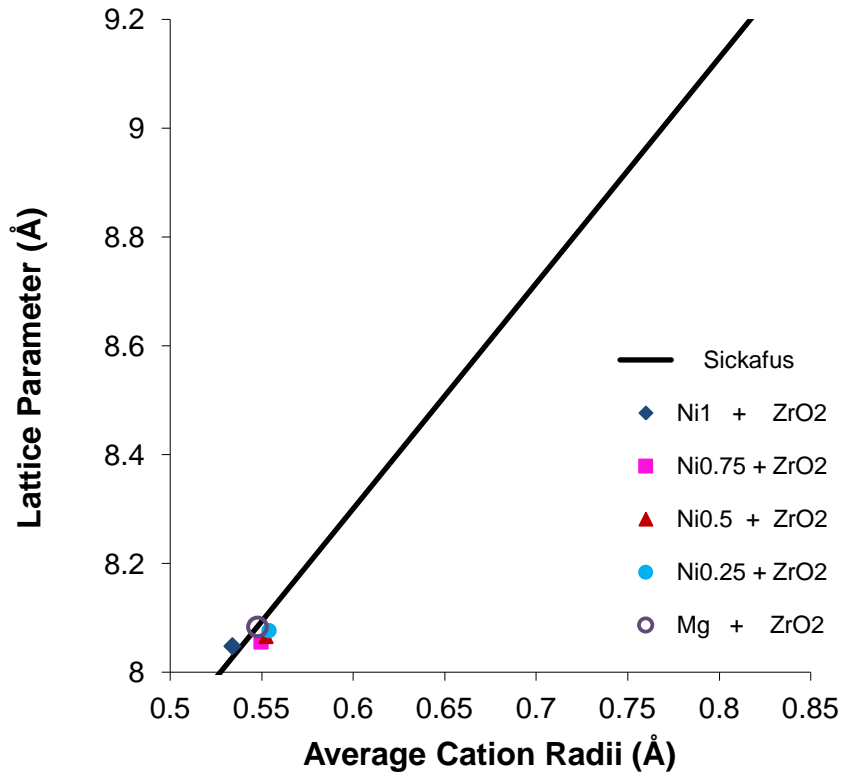


Figure 16. As-synthesized spinel lattice parameters and comparison to an empirical fit for an array of binary spinel compositions by Sickafus et al. The axis ranges shown match those in Sickafus et al.<sup>8</sup>

A comparison to the work of Porta et al.<sup>1</sup> in this respect is not possible, as they assumed the fraction of Mg ions on tetrahedral sites to be constant at 1 while determining the distribution of Ni between the octahedral and tetrahedral sites. This assumption precludes an accurate determination of the average cation radii. The tetrahedral and octahedral cation radii used in this calculation are taken from the work of O'Neill and Navrotsky,<sup>10</sup> who performed a procedure like that used by Shannon and Prewitt in developing the cation radii tables, but instead used only spinel structures in the fitting procedure. This revealed small but significant differences in the radius assumed by cations in spinels versus their radii in other structures.

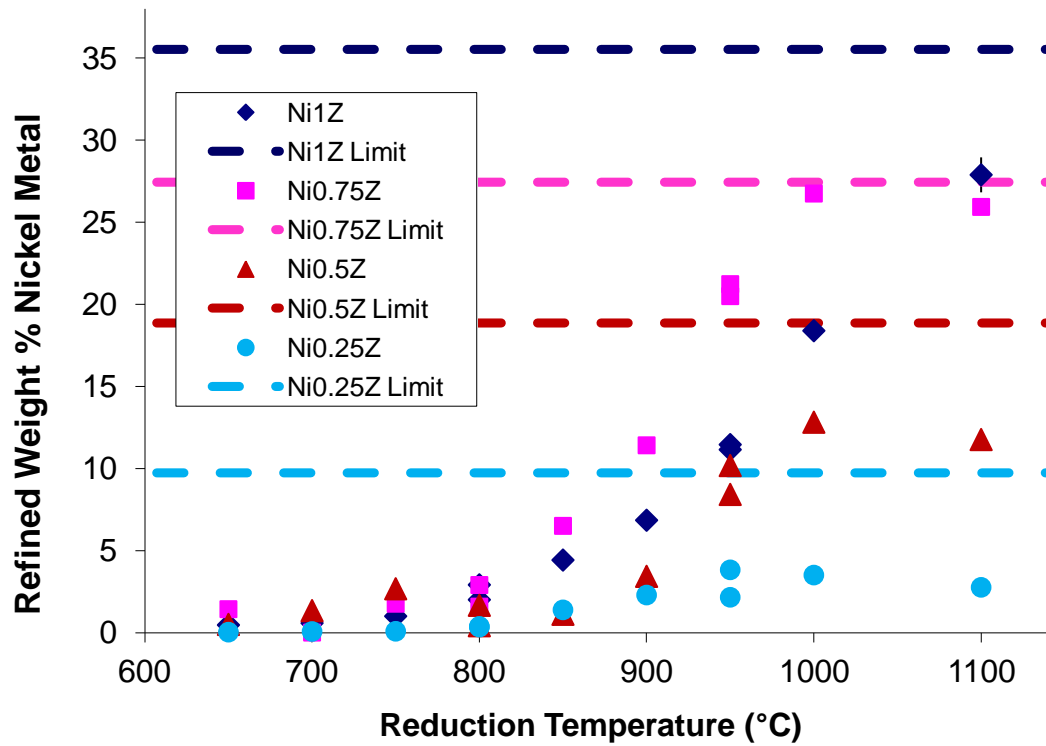


Figure 17. Refined nickel metal weight percent reduced from each composition as a function of reduction temperature. Error bars of one standard deviation are shown, but most are smaller than the data marker.

Figure 17 shows the nickel metal weight percent present after reduction for the time corresponding to each reduction temperature. The presence of nickel metal is barely detectable by X-ray diffraction in the 650 and 700 °C reduced spinels, but the crystallites can readily be seen in the SEM in the  $\text{NiAl}_2\text{O}_4 + 2.5 \text{ wt.}\% \text{ ZrO}_2$  samples, as shown in Figures 18 and 19.

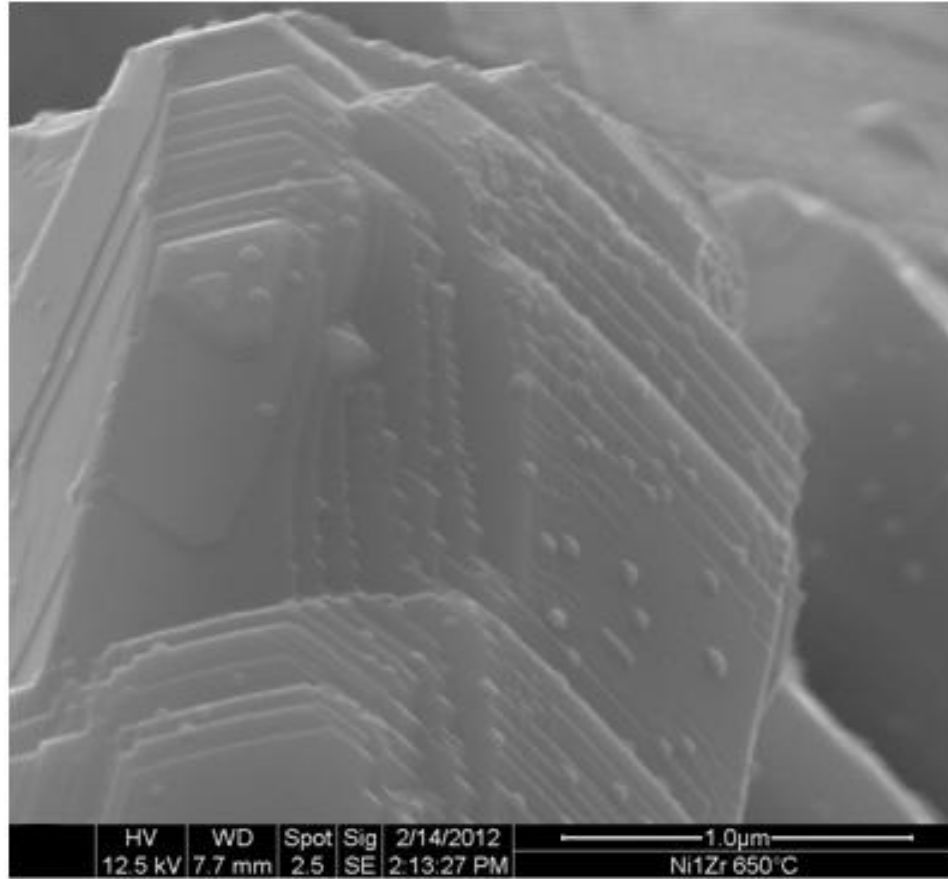


Figure 18. Secondary electron image of  $\text{NiAl}_2\text{O}_4 + 2.5 \text{ wt\% ZrO}_2$ , reduced at  $650^\circ\text{C}$  in 300 Torr  $\text{H}_2$  for 94 hours. 50 kX original magnification.

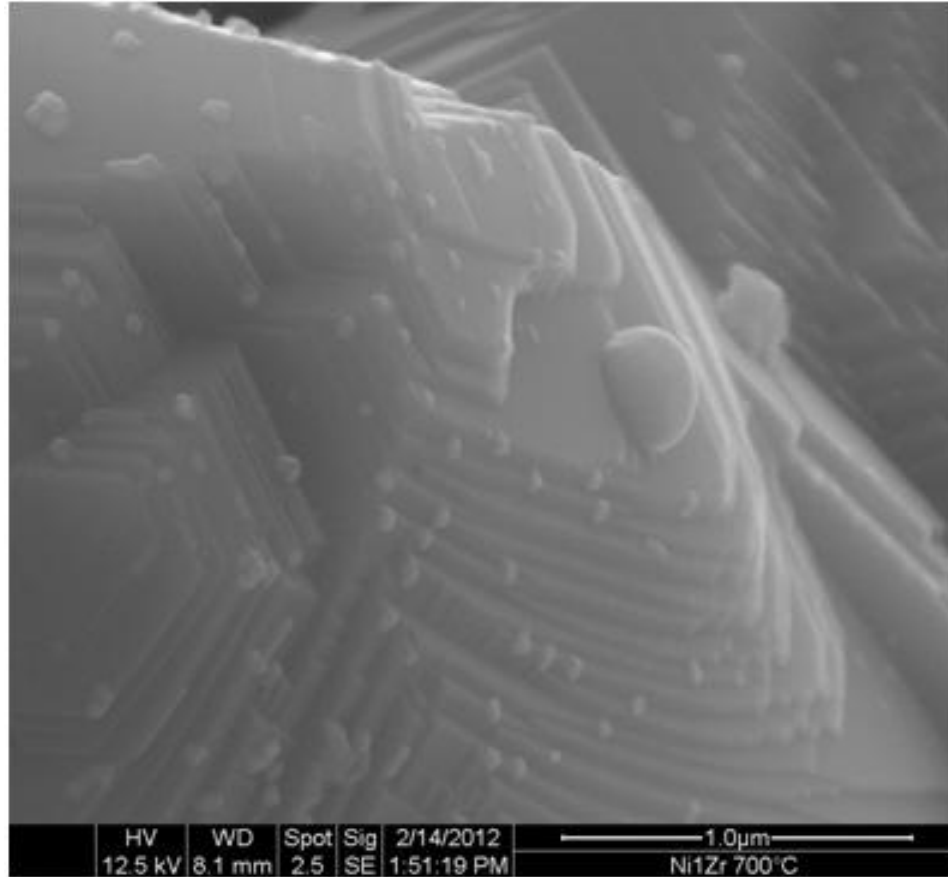


Figure 19. Secondary electron image of  $\text{NiAl}_2\text{O}_4 + 2.5 \text{ wt\% ZrO}_2$ , reduced at  $700 \text{ }^\circ\text{C}$  in 300 Torr  $\text{H}_2$  for 71 hours. 50 kX original magnification.

Only  $\text{Ni}_{0.75}\text{Mg}_{0.25}\text{Al}_2\text{O}_4 + 2.5 \text{ wt\% ZrO}_2$  reached full reduction at any of the reduction temperatures employed, indicating that the number of moles of  $\text{H}_2$  present in the furnace was insufficient given the reducible nickel mass present. Kinetic effects are also apparent, as the phase fraction of nickel metal in  $\text{Ni}_{0.75}\text{Mg}_{0.25}\text{Al}_2\text{O}_4 + 2.5 \text{ wt\% ZrO}_2$  is equal to or greater than the nickel metal phase fraction in  $\text{NiAl}_2\text{O}_4 + 2.5 \text{ wt\% ZrO}_2$  from  $750 \text{ }^\circ\text{C}$  to  $1000 \text{ }^\circ\text{C}$ , despite containing less nickel. This can be explained by the isothermal and nonisothermal TGA results discussed later, where  $\text{Ni}_{0.75}\text{Mg}_{0.25}\text{Al}_2\text{O}_4 + 2.5 \text{ wt\% ZrO}_2$  consistently shows a faster rate of weight loss than does  $\text{NiAl}_2\text{O}_4 + 2.5 \text{ wt\% ZrO}_2$ . The Rietveld refinement results suggest that the  $\text{Ni}_{0.75}\text{Mg}_{0.25}\text{Al}_2\text{O}_4 + 2.5 \text{ wt\% ZrO}_2$  composition consumes a large proportion of the  $\text{H}_2$  in the furnace. This would continue until the  $\text{PO}_2$  rose to the dissociation pressure of the  $\text{Ni}_{0.75}\text{Mg}_{0.25}\text{Al}_2\text{O}_4 + 2.5 \text{ wt\% ZrO}_2$ , at

which point the  $\text{NiAl}_2\text{O}_4 + 2.5 \text{ wt\% ZrO}_2$  would consume the remaining  $\text{H}_2$  until the  $\text{PO}_2$  rose to its dissociation pressure.

There is apparently a shifting in the kinetics of the reduction of  $\text{NiAl}_2\text{O}_4 + 2.5 \text{ wt\% ZrO}_2$  at 1100 °C, as  $\text{Ni}_{0.75}\text{Mg}_{0.25}\text{Al}_2\text{O}_4 + 2.5 \text{ wt\% ZrO}_2$  ends with less nickel metal than it did at 1000 °C. The reduction of  $\text{NiAl}_2\text{O}_4 + 2.5 \text{ wt\% ZrO}_2$  is not necessarily faster than that of  $\text{Ni}_{0.75}\text{Mg}_{0.25}\text{Al}_2\text{O}_4 + 2.5 \text{ wt\% ZrO}_2$  at 1100 °C, as they could reduce at nearly the same rate until the  $\text{PO}_2$  reached the dissociation pressure of  $\text{Ni}_{0.75}\text{Mg}_{0.25}\text{Al}_2\text{O}_4 + 2.5 \text{ wt\% ZrO}_2$ , at which point the  $\text{NiAl}_2\text{O}_4 + 2.5 \text{ wt\% ZrO}_2$  would be able to consume a little more of the  $\text{H}_2$ . It is possible that this is a thermodynamic effect rather than a kinetic one. Nothing is known of the dissociation pressures of the solid solution compositions, and if the dissociation pressures of the compositions shift different relatively to one another with temperature, the dissociation pressure limits could also explain this behavior given that this is reduction in a closed system. The same effect is observed for  $\text{Ni}_{0.5}\text{Mg}_{0.5}\text{Al}_2\text{O}_4 + 2.5 \text{ wt\% ZrO}_2$ , as it contains less nickel metal after reduction at 1100 °C than after reduction at 1000 °C. This is also seen for  $\text{Ni}_{0.25}\text{Mg}_{0.25}\text{Al}_2\text{O}_4 + 2.5 \text{ wt\% ZrO}_2$  at 1000 °C and 1100 °C. Given that the 1100 °C do not fit earlier trends, that reduction was repeated. The results originally seen were reproduced, but are not reported.

Figure 20 shows the refined lattice parameter for each composition in the as-synthesized form, and at each reduction temperature used. There is very little change in the lattice parameter of any composition until the 800 or 850 °C reduction. This agrees well with the refined weight percent nickel shown in Figure 17, where no significant amount of nickel is reduced from the spinel until 800 °C. The strange results seen in Figure 17 as to the lowered weight percent nickel metal at higher temperatures are also reproduced in the spinel lattice parameter. It should be noted that the refined spinel lattice parameter and the refined nickel metal phase fraction are two completely independent results of the Rietveld refinement that show the same trend.

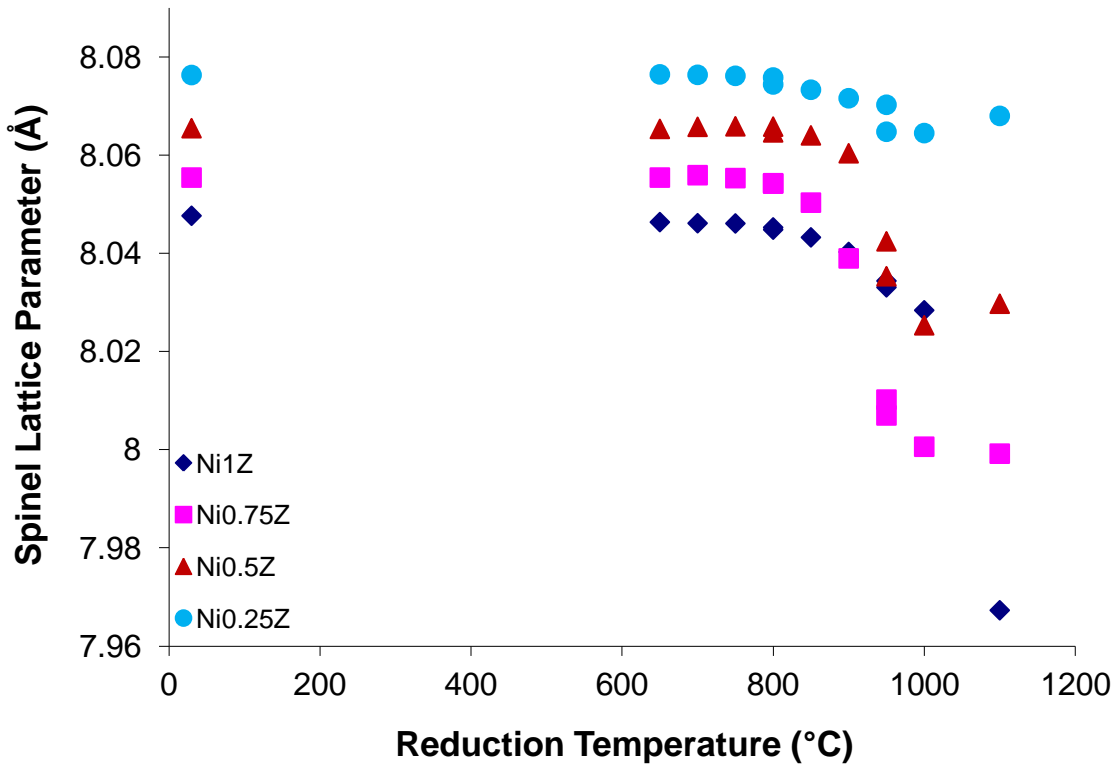


Figure 20. Observed spinel lattice parameter versus the temperature of reduction. Error bars of one standard deviation are smaller than the data marker.

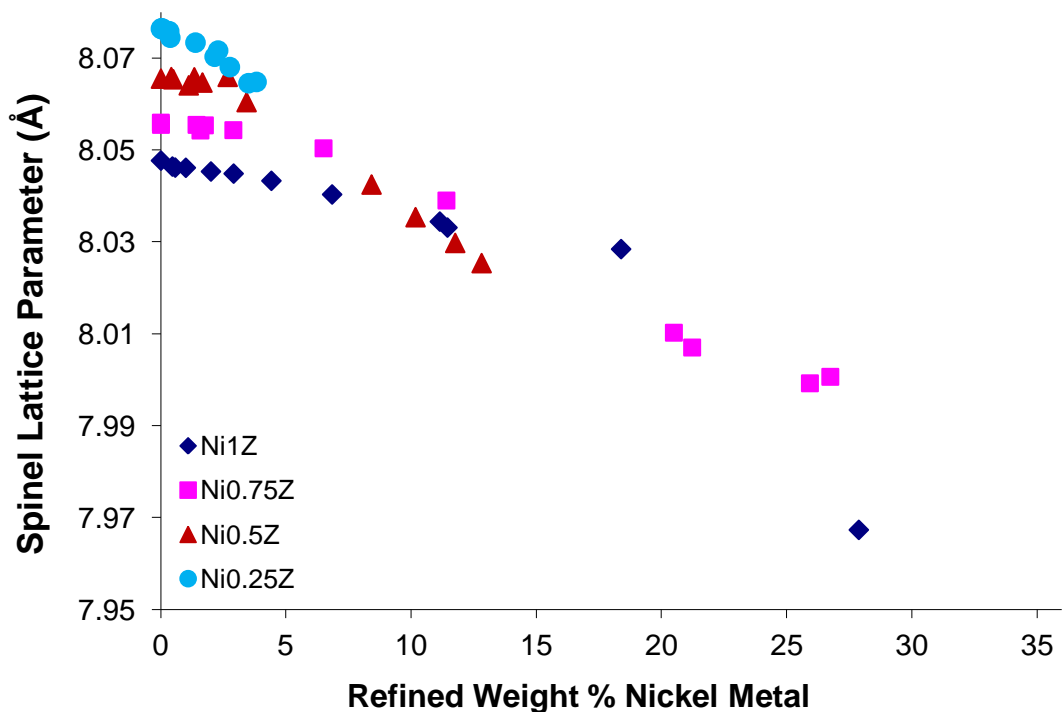


Figure 21. Observed spinel lattice parameters as a function of refined nickel metal weight percent. Error bars are smaller than the data markers.

Figure 21 shows the refined spinel lattice parameters plotted as a function of the refined weight percent of nickel metal. Plotted in this manner, it can be seen that the odd trends seen in Figure 17 and Figure 20 are in agreement with one another. Each set of data follows the trend well except the  $\text{NiAl}_2\text{O}_4 + 2.5 \text{ wt\% ZrO}_2$  sample reduced at 1100 °C.

Figure 22 plots the refined oxygen parameter as a function of the refined weight percent nickel metal. All compositions show a reasonable trend. The lowest value of the oxygen parameter refined by Rotan et al.<sup>21</sup> in studying  $\text{Al}_2\text{O}_3$  excess in  $\text{NiAl}_2\text{O}_4$  was 0.255. One of the refined values of the oxygen parameter of  $\text{NiAl}_2\text{O}_4 + 2.5 \text{ wt\% ZrO}_2$  is at 0.255, while four others are below it. This may be an indication that the remnant spinel remaining in those four samples, the two 950 °C samples, and the 1000 and 1100 °C samples may not be stable, and may transform to metastable spinel if heated to a suitable temperature.

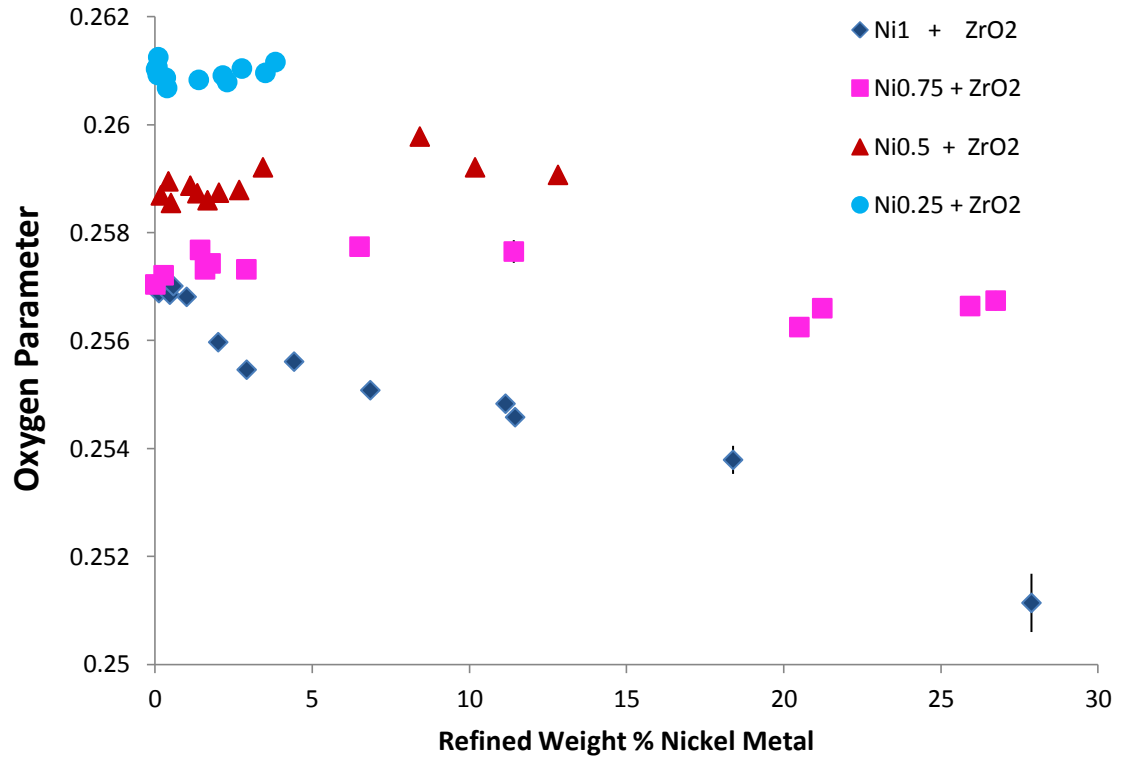


Figure 22. Oxygen parameter in the spinel as a function of the refined weight percent nickel metal. Error bars of one standard deviation are shown, but are smaller than most of the data markers.

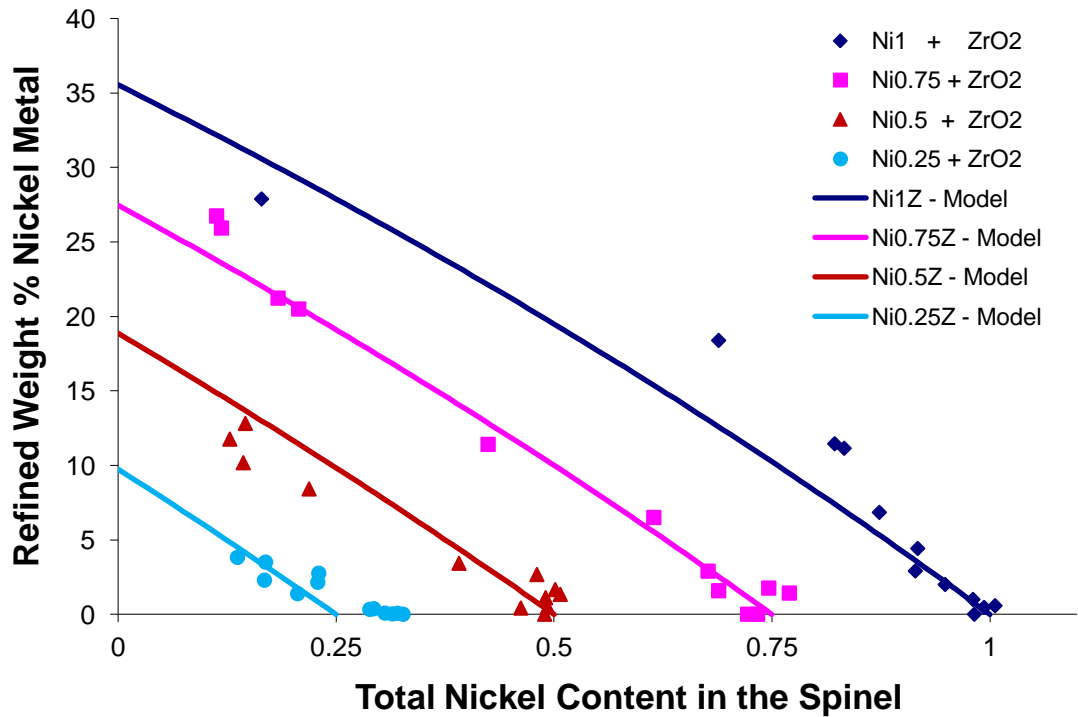


Figure 23. Refined weight percent nickel metal versus the combined octahedral and tetrahedral nickel spinel refined site occupancies. Solid lines show conservation of mass for nickel. Data points show the results of refinements, of which the total nickel in the spinel and the refined nickel metal phase fraction are independent quantities.

Figure 23 shows a comparison between total nickel conservation and the results of the refinement. The solid lines show a mass balance of nickel, illustrating the concept that if nickel leaves the spinel, it must become nickel metal. The mass loss of oxygen from the sample is accounted for in the mass balance between the spinel and the nickel metal. Agreement between the nickel occupancy in the spinel and the refined nickel metal phase fraction was not enforced in the refinement, as attempting to do so created a circular constraint. The low reduction temperature  $\text{Ni}_{0.25}\text{Mg}_{0.75}\text{Al}_2\text{O}_4 + 2.5 \text{ wt\% ZrO}_2$  sample's refinements yield too much nickel in the spinel, but the agreement is quite good for the rest of the samples.

Figures 24 and 25 show refined microstrain broadening in the nickel metal and the spinel respectively, plotted as a function of the refined weight percent of nickel metal. No real trend is seen for microstrain in the nickel, but a general trend of increasing

microstrain with increasing nickel metal phase fraction can be seen, though some very high values are seen for  $\text{Ni}_{0.75}\text{Mg}_{0.25}\text{Al}_2\text{O}_4 + 2.5 \text{ wt\% ZrO}_2$  due to the peak splitting that occurs in the 900 and 950 °C reduction samples, as can be seen in Figure 9. An increase in the microstrain of the spinel with increasing nickel metal phase fraction agrees with the model system, as the removal of  $\text{Ni}^{2+}$  from the spinel creates cation vacancies to charge compensate for the increasing  $\text{Al}^{3+}$  content. Cation vacancies are crystalline imperfections, and would contribute to microstrain broadening, so this result is consistent with expectations.

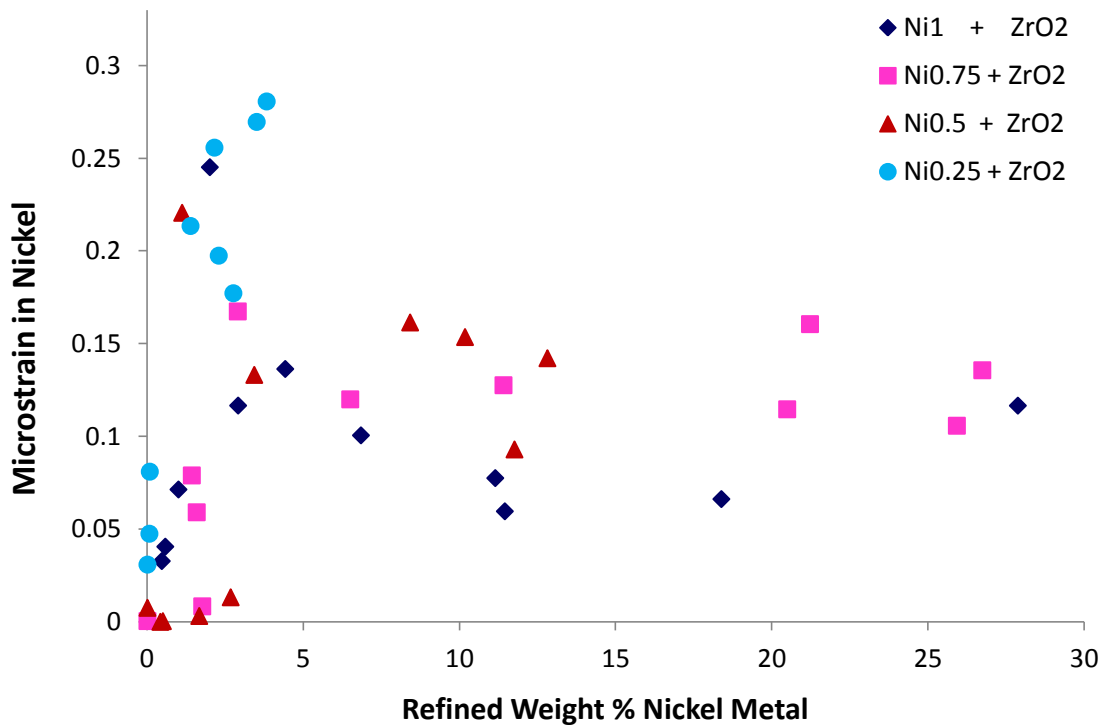


Figure 24. Microstrain in nickel metal as a function of the refined weight percent of nickel metal.

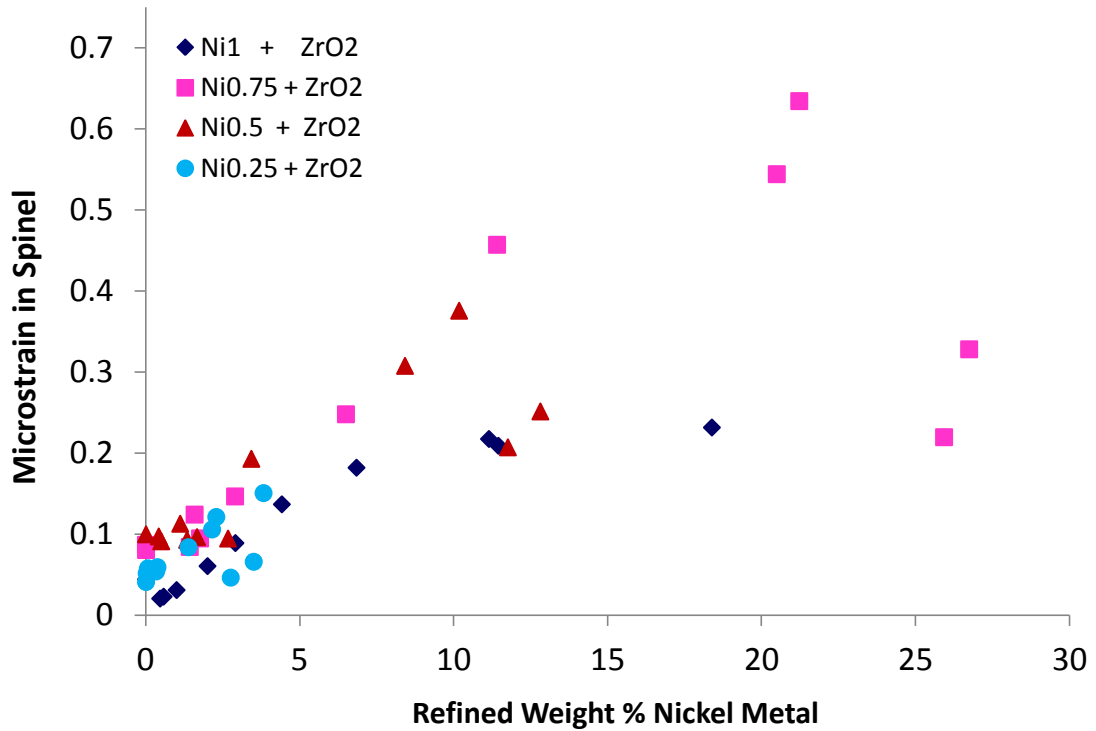


Figure 25. Microstrain in the spinel as a function of the refined weight percent of nickel metal.

The shape of the nickel metal reflections which necessitate the use of the tan theta dependent hat function convolution to fit is shown in Figure 6. Figures 26 and 27 show the magnitude of the hat function convolution plotted as a function of the reduction temperature used, and the refined weight percent of nickel metal respectively. Neither plot is particularly more convincing than the other. The behavior of the  $\text{Ni}_{0.25}\text{Mg}_{0.75}\text{Al}_2\text{O}_4 + 2.5 \text{ wt\% ZrO}_2$  sample does not fit with the rest of the data set plotted against either variable, but visual inspection of the patterns confirms that its nickel metal peak looks more normal with increasing reduction temperature. Weight percent nickel metal and reduction temperature are highly correlated in this data set, making discrimination difficult. Three causes for the observed nickel metal peak shapes were hypothesized. The first was the peak shape was due to a reflection of slightly lower d-spacing from a metastable spinel-based phase. Second, the asymmetry was due to thermal expansion mismatch between the spinel and the nickel metal upon cooling from the reduction temperature. Nearly all of the nickel metal is on the surface of the spinel

particles, and the coefficient of thermal expansion of spinel is roughly half of that of the nickel metal. The portion of the nickel metal crystallite nearest the interface would be constrained from contracting as much as the rest of the nickel metal crystallite, giving a higher lattice spacing in the vicinity of the spinel. Thirdly, the low angle shoulder could be due to a small amount of Ni-Al alloy, which has a higher lattice parameter than pure nickel metal.

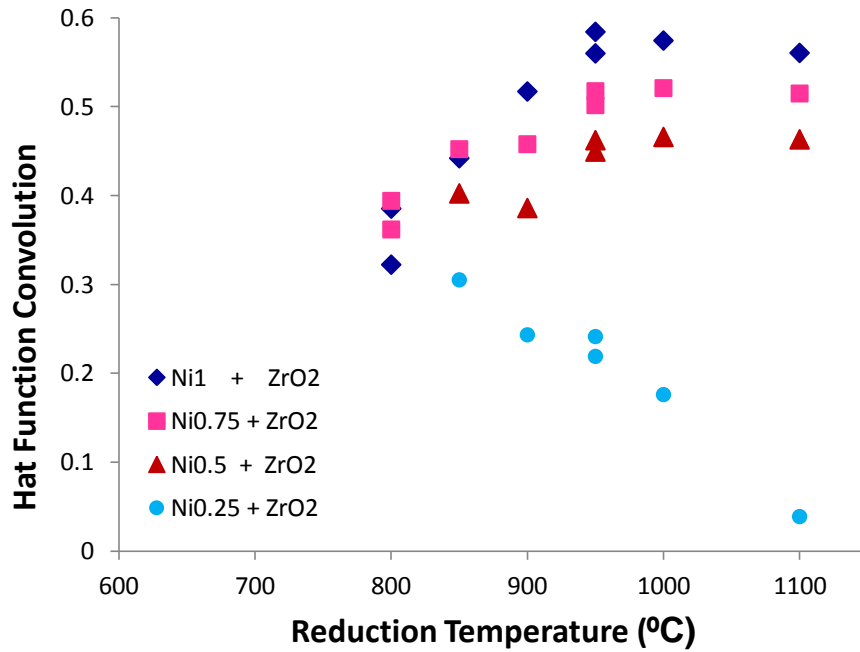


Figure 26. Value of the  $\tan-\Theta$  dependent hat function convolution used in fitting the nickel metal reflections, as a function of reduction temperature.

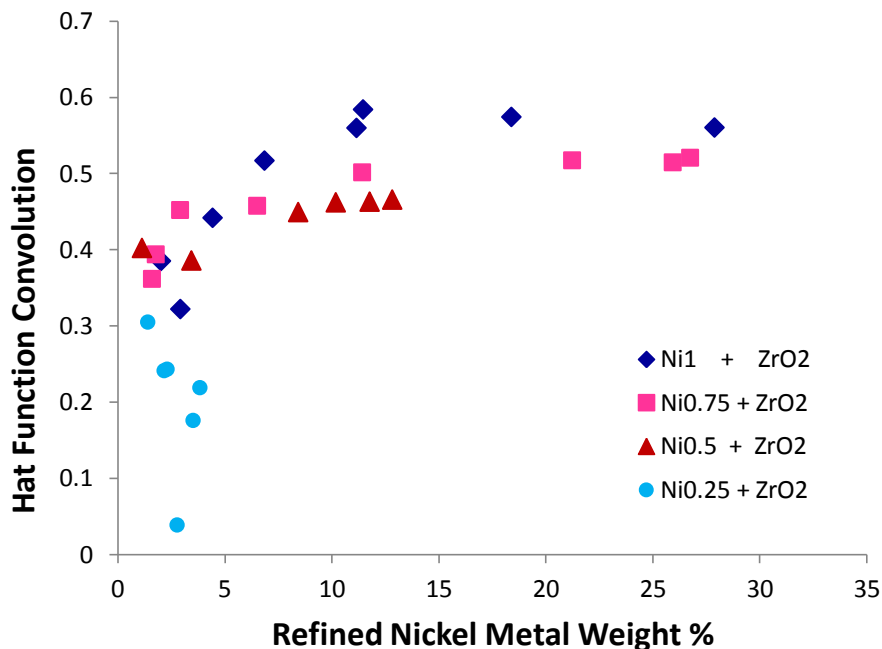


Figure 27. Value of the  $\tan\Theta$  dependent hat function convolution used in fitting the nickel metal reflections, as a function of the refined weight percent of nickel metal.

High temperature X-ray diffraction was deemed the best tool for investigating the nickel metal peak shape, as it could inform as to the accuracy of hypotheses one and two. To conduct this investigation,  $\text{NiAl}_2\text{O}_4 + 2.5 \text{ wt.}\% \text{ ZrO}_2$  reduced at  $1000 \text{ }^\circ\text{C}$  for 12 hours in 300 Torr  $\text{H}_2$  was placed in the high temperature diffractometer under a flow of  $\text{N}_2$  so the sample would not reduce further, and patterns were recorded at  $30 \text{ }^\circ\text{C}$ , and at intervals of  $100 \text{ }^\circ\text{C}$  to  $1000 \text{ }^\circ\text{C}$ . If the root cause of the peak shape were thermal expansion mismatch, the peak shape should alter from a distorted shape at room temperature, towards a normal peak shape at the reduction temperature. If a metastable spinel polymorph were the cause of the peak distortion, the differences in the coefficient of thermal expansion between the spinel and the nickel metal would cause the peaks to separate as higher temperatures were reached. If too slow a heating rate were used, the metastable phase could transform to another metastable phase or corundum, but that new set of peaks would be seen in the diffraction pattern.

The resolution of the high temperature diffractometer was somewhat lower than for room temperature scans, and as such it was somewhat difficult to discern the peak

shape distortion visually; however, Rietveld refinement was able to quantify the distortion. When a sample of  $\text{NiAl}_2\text{O}_4 + 2.5 \text{ wt\% ZrO}_2$  previously reduced at  $1000^\circ\text{C}$  for 12 hours in 300 Torr  $\text{H}_2$  was heated in  $\text{N}_2$ , the magnitude of the hat function convolution is seen to decrease monotonically upon heating. The magnitude of the convolution reached 0 at 900 and  $1000^\circ\text{C}$ , but returns upon cooling to  $30^\circ\text{C}$ , as seen in Figure 28. As can be seen in Figure 26, the hat function convolution reaches a maximum in the  $950^\circ\text{C}$  reduced samples for all but the  $\text{Ni}_{0.25}\text{Mg}_{0.75}\text{Al}_2\text{O}_4$  composition. This suggests that  $\sim 900 - 950^\circ\text{C}$  is a strain free temperature for the Ni metal and the spinel, such that the thermal expansion mismatch only affects them upon cooling below this temperature.

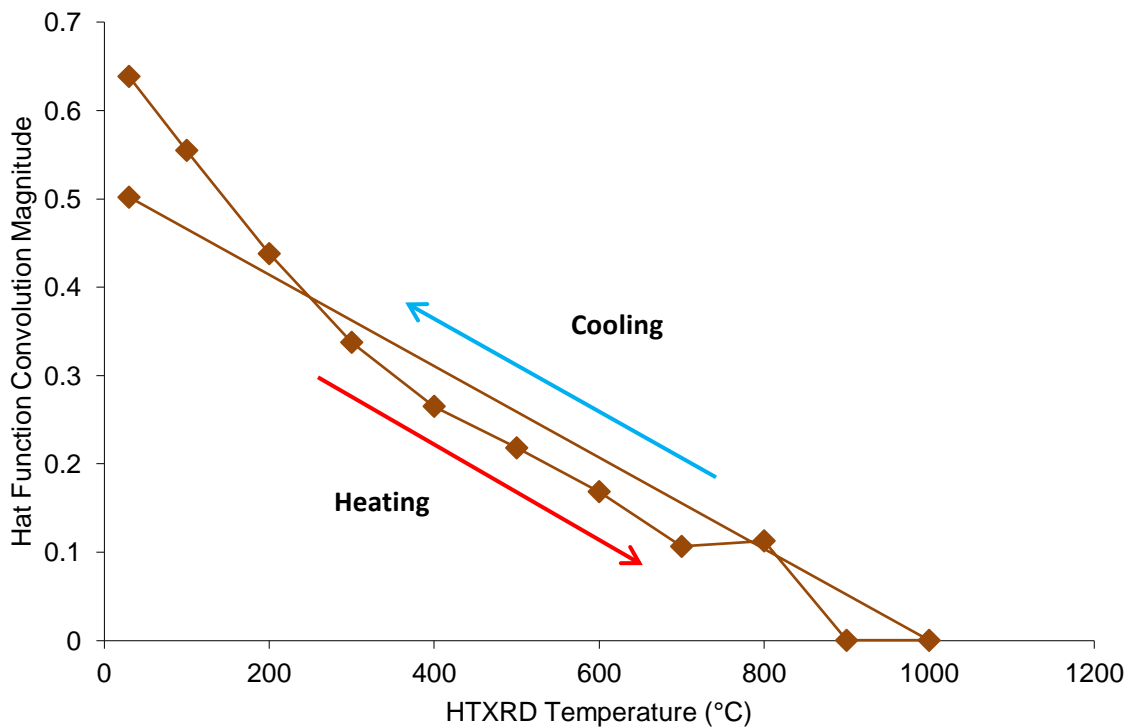


Figure 28. Refined hat function convolution of nickel metal during HTXRD in flowing  $\text{N}_2$  of  $\text{NiAl}_2\text{O}_4 + 2.5 \text{ wt\% ZrO}_2$  reduced at  $1000^\circ\text{C}$  for 12 hours in 300 Torr  $\text{H}_2$ . The peak shape distortion disappears upon heating, and reappears upon cooling.

An inert atmosphere of flowing N<sub>2</sub> was used to preclude further reduction that would complicate the results. Given that the mixture of nonstoichiometric spinel and metastable spinel and nickel metal is not a thermodynamically stable mixture at any PO<sub>2</sub>, some of the nickel metal was resorbed by the spinel during the measurement, as can be seen in Figure 29, which complicates the analysis of this result somewhat. Nonetheless, the hat function convolution is seen in Figure 28 to go to 0 at high temperature and return upon cooling, which strongly supports the assertion that the nickel metal peak shape distortion results from thermal expansion mismatch between the nickel metal and the spinel.

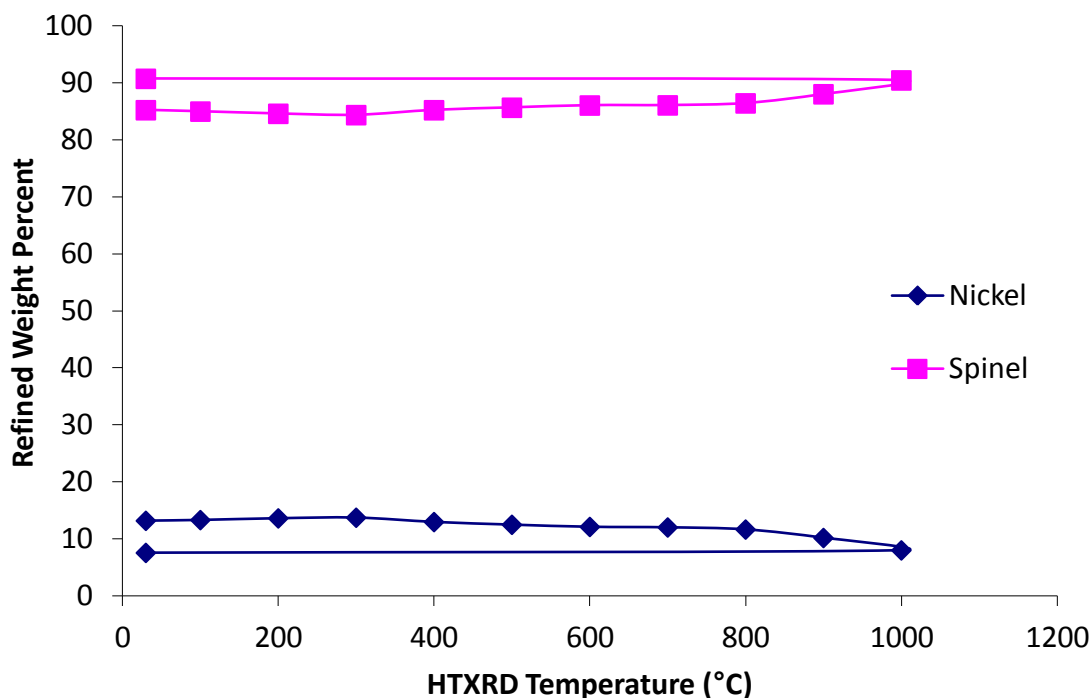


Figure 29. Refined weight percents of nickel and spinel during the HTXRD measurement in flowing N<sub>2</sub> of NiAl<sub>2</sub>O<sub>4</sub> + 2.5 wt% ZrO<sub>2</sub> reduced at 1000 °C for 12 hours in 300 Torr H<sub>2</sub>. Resorption of some nickel by the spinel is seen.

Of the three possibilities (thermal expansion mismatch, a metastable spinel, or some Ni-Al alloy), the presence of a Ni-Al alloy was deemed the least likely based on available literature. From the work of Elrefaie and Smeltzer<sup>35</sup> on the oxygen activity and

temperature dependence of the reduction of  $\text{NiAl}_2\text{O}_4$ , the formation of a Ni-Al alloy requires an oxygen partial pressure of  $\sim 10^{-22}$  atm at  $1000^\circ\text{C}$ . For reference, that is below the stability limit of  $\text{SiO}_2$ ,  $\text{MnO}$ , and  $\text{Cr}_2\text{O}_3$ . However, EELS maps obtained in the TEM strongly suggest at least some Al is present in the needle-like nickel particles in the interior of grains, shown in Figure 30. The TEM image of this crystallite can be seen in Figure 77. Despite the low oxygen partial pressure reported by Elrefaie and Smeltzer necessary to form a Ni-Al alloy, its existence in these samples and its contribution to the nickel metal peak shape cannot fully be discounted.

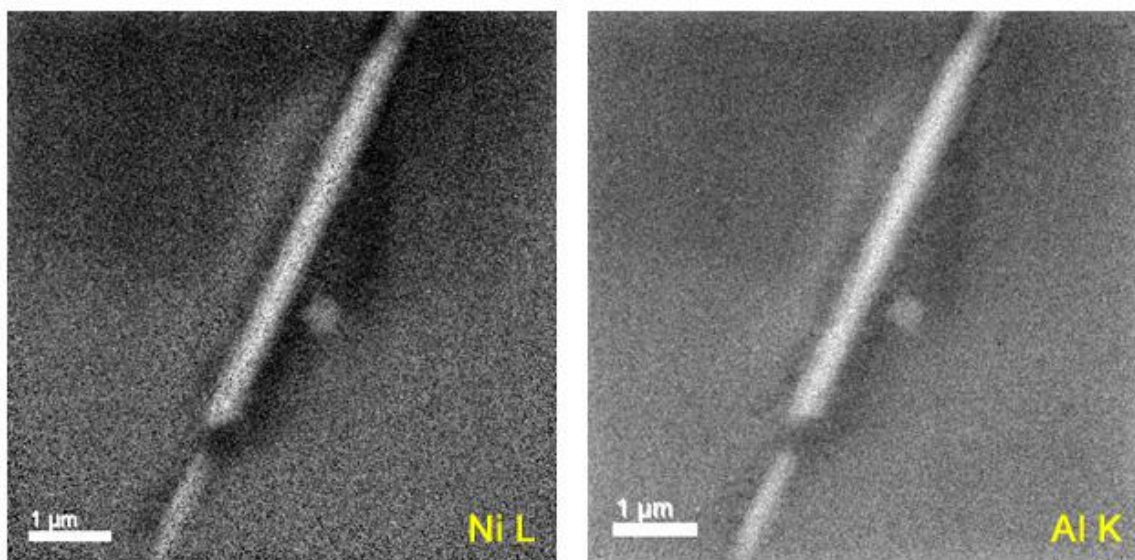


Figure 30. Ni L and Al K EELS maps from a needle-like nickel particle from the interior of a spinel grain in  $\text{NiAl}_2\text{O}_4 + 2.5$  wt%  $\text{ZrO}_2$  reduced at  $850^\circ\text{C}$  for 24 hours in 300 Torr  $\text{H}_2$ .

The distorted nickel peak shape is not observed when highly reduced samples obtained in the HTXRD or TGA are run in the Bruker D8 high resolution X-ray diffractometer. This could be viewed as evidence of the formation of a Ni-Al alloy in the pure  $\text{H}_2$  reduced samples, as the atmosphere in the HTXRD and TGA experiments was kept constant with a flowing stream of 4%  $\text{H}_2$ , while the closed system reductions started with pure  $\text{H}_2$ , which would then become an  $\text{H}_2/\text{H}_2\text{O}$  mixture as the reduction commenced. The pure  $\text{H}_2$  used would give a much lower oxygen partial pressure at the start of the

reduction than that seen by the samples reduced in the TGA or HTXRD, perhaps low enough to form a Ni-Al alloy with a small amount of aluminum.

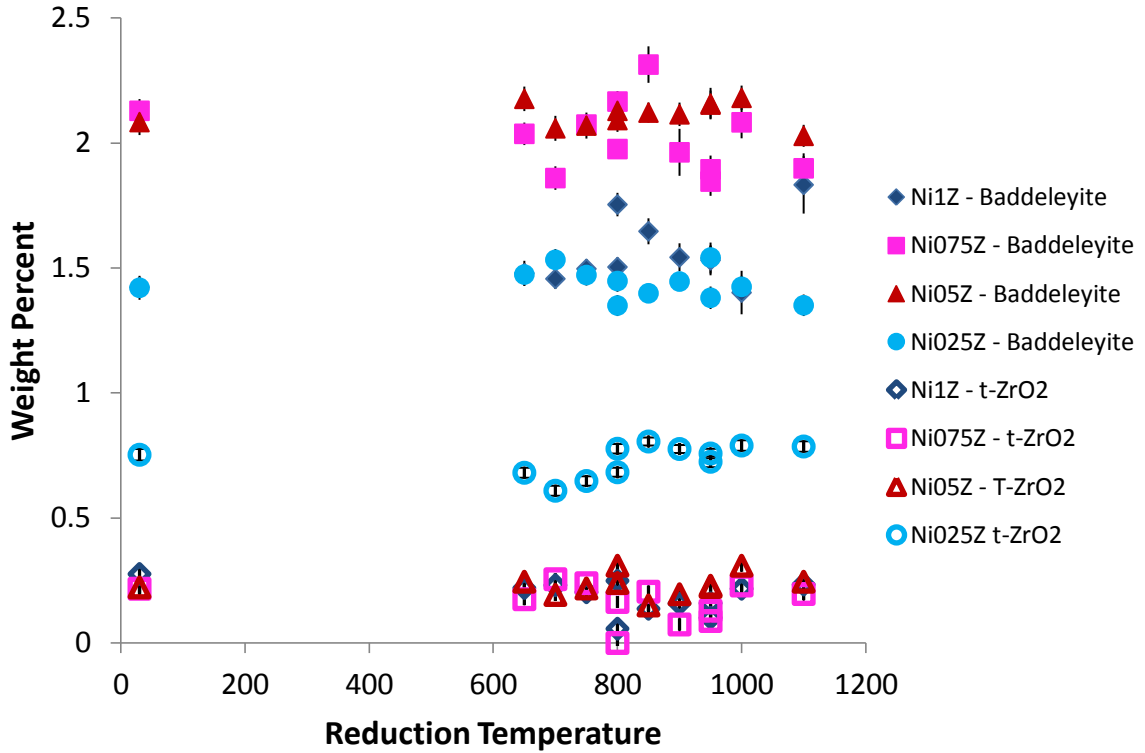


Figure 31. Refined Baddeleyite and tetragonal  $ZrO_2$  weight percents in the reduced spinel composites. Error bars show one standard deviation.

Figure 31 shows the refined monoclinic and tetragonal  $ZrO_2$  phase fractions for each refinement. The refined values are impressively consistent given the very small amounts.

In the refinements of samples containing metastable phases, the refined nickel metal phase fraction should be regarded as no more than an estimate, as many reflections of the metastable phases are not accounted for by the spinel model. The metastable phases share all the reflection lines of spinel, making exact determination of the appearance of metastable phases somewhat challenging. Inclusion of metastable phases in the refinement is impractical and not particularly useful. Structures are not available for any of the metastable phases. Even if structures were available, adding them to the

refinement in an attempt to determine the amount of nickel metal present by refinement would be inaccurate, as very little is known about the solubility limits of the phases.

## B. High Temperature X-ray Diffraction – $\text{Ni}_x\text{Mg}_{1-x}\text{Al}_2\text{O}_4$

Figures 32 through 35 show HTXRD of the solid solution series in 200 ml/min flowing 4%  $\text{H}_2/\text{N}_2$  at 30 °C, then 600, 700, 800, 900, 1000, 1100, 1200, and finally 1300 °C. Ni metal formation is visible in all samples in the 900 °C pattern. Upon reaching a temperature of 1300 °C, both  $\text{NiAl}_2\text{O}_4 + 2.5 \text{ wt\% ZrO}_2$  and  $\text{Ni}_{0.75}\text{Mg}_{0.25}\text{Al}_2\text{O}_4 + 2.5 \text{ wt\% ZrO}_2$  form corundum, which is not seen in either sample when reduced for 40 hours at 1000 °C in the TGA. Theta- $\text{Al}_2\text{O}_3$  is seen in the  $\text{NiAl}_2\text{O}_4 + 2.5 \text{ wt\% ZrO}_2$  composition after reducing for 40 hours in the TGA. However, no alumina phases are seen in  $\text{Ni}_{0.75}\text{Mg}_{0.25}\text{Al}_2\text{O}_4 + 2.5 \text{ wt\% ZrO}_2$  after 40 hours in the TGA.

$\text{Ni}_{0.5}\text{Mg}_{0.5}\text{Al}_2\text{O}_4 + 2.5 \text{ wt\% ZrO}_2$  and  $\text{Ni}_{0.25}\text{Mg}_{0.75}\text{Al}_2\text{O}_4 + 2.5 \text{ wt\% ZrO}_2$  show only nickel metal, the zirconia phases, and spinel; the same phases present after reduction at 1000 °C for 16 hours in the TGA.

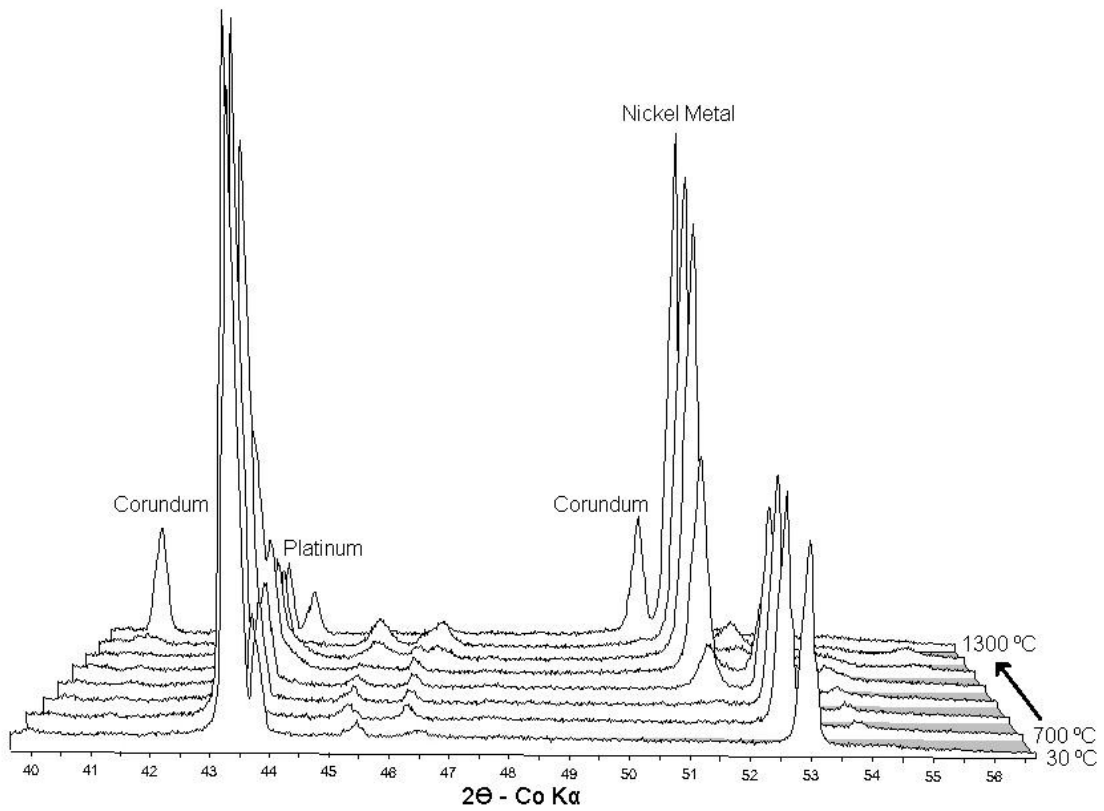


Figure 32. HTXRD of  $\text{NiAl}_2\text{O}_4 + 2.5 \text{ wt\% ZrO}_2$  in flowing  $4\% \text{ H}_2/\text{N}_2$ . Room temperature to 1300 °C.  $\text{Co-K}\alpha$  radiation. Nickel metal is clearly seen at 900 °C, and corundum at 1300 °C.

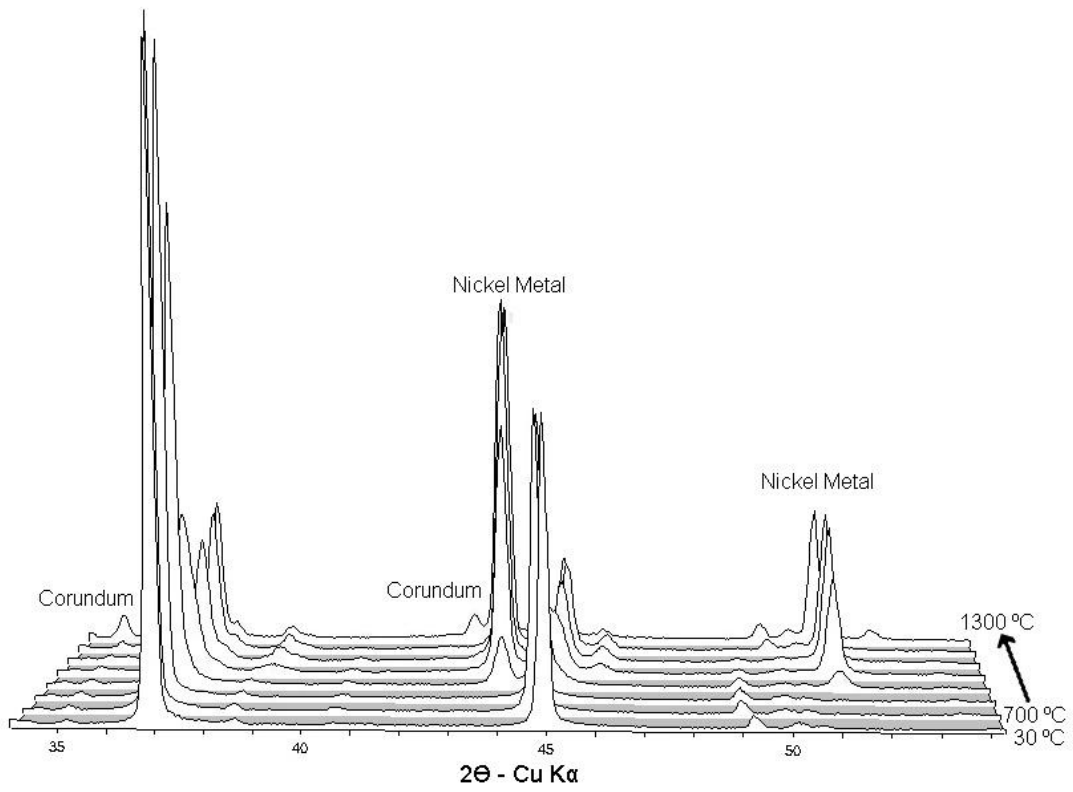


Figure 33. HTXRD of  $\text{Ni}_{0.75}\text{Mg}_{0.25}\text{Al}_2\text{O}_4 + 2.5 \text{ wt\% ZrO}_2$  in flowing 4%  $\text{H}_2/\text{N}_2$ . Room temperature to 1300 °C. Nickel metal is clearly seen at 900 °C, and corundum at 1300 °C.

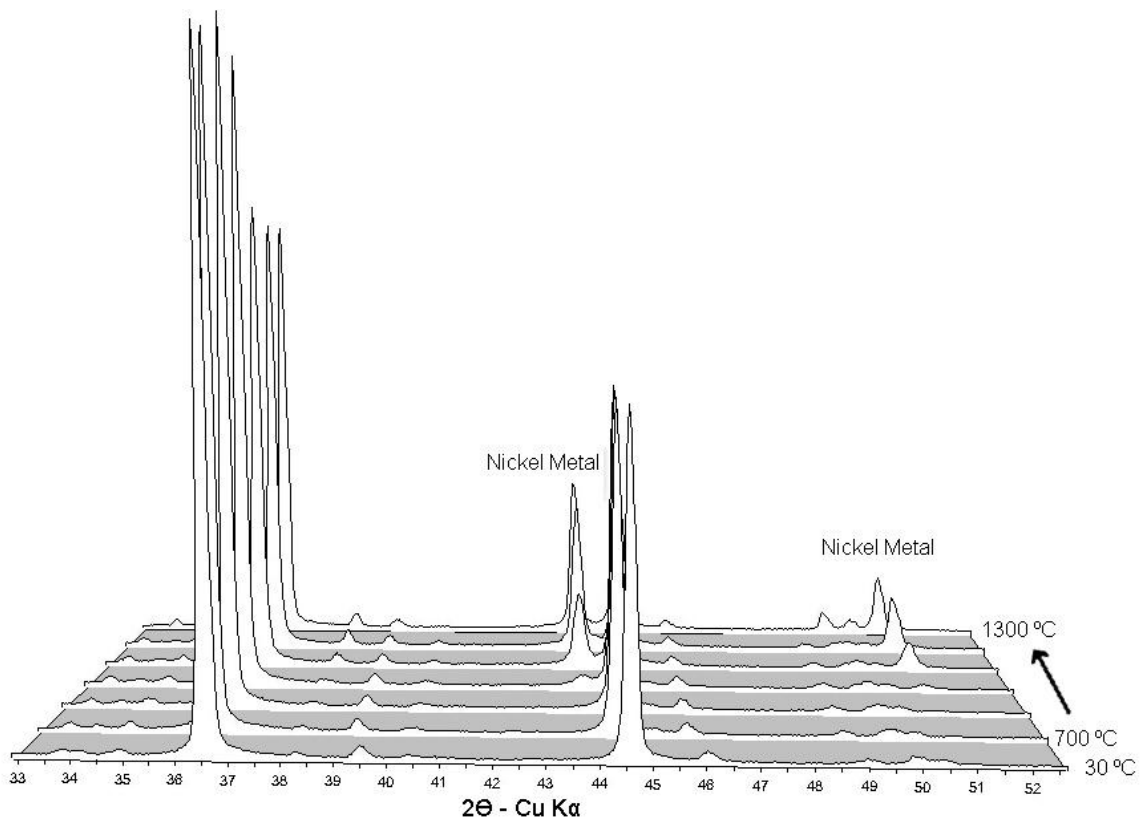


Figure 34. HTXRD of  $\text{Ni}_{0.5}\text{Mg}_{0.5}\text{Al}_2\text{O}_4 + 2.5 \text{ wt\% ZrO}_2$  in flowing 4%  $\text{H}_2/\text{N}_2$ . Room temperature to 1300 °C. Nickel metal is clearly seen at 900 °C, and no corundum formation is seen.

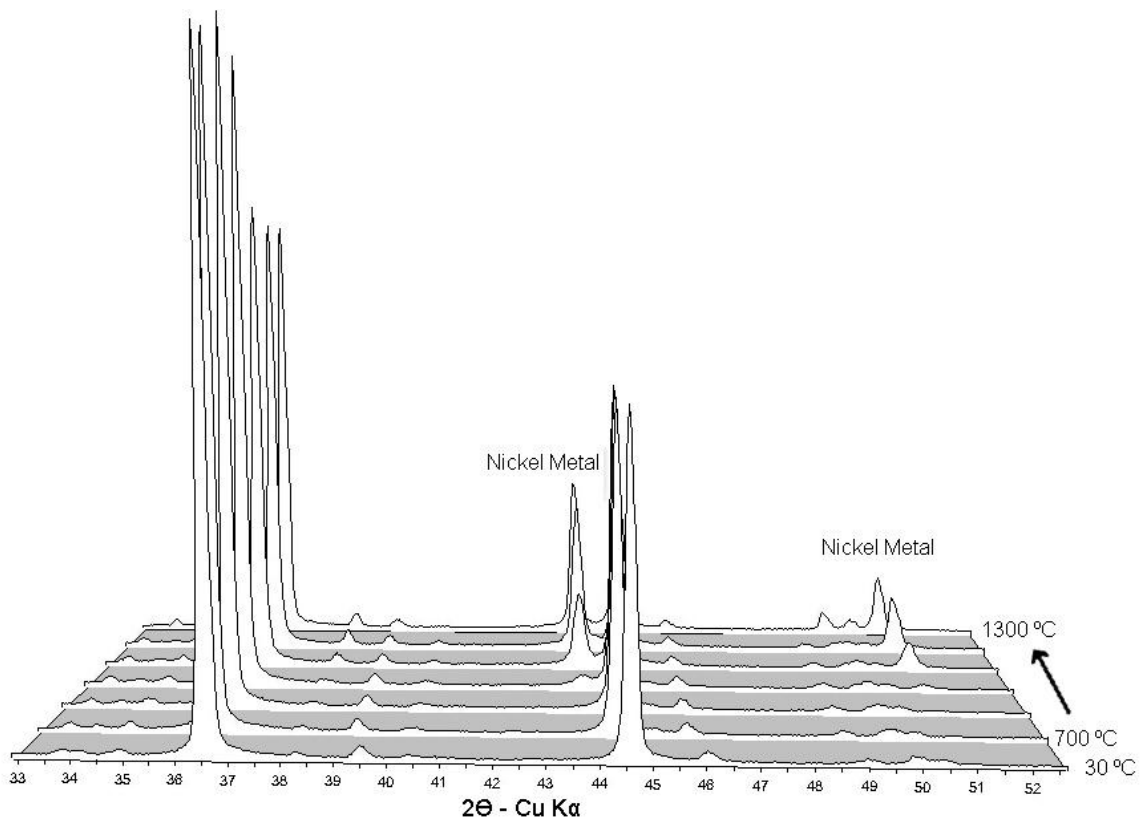


Figure 35. HTXRD of  $\text{Ni}_{0.25}\text{Mg}_{0.75}\text{Al}_2\text{O}_4 + 2.5 \text{ wt\% ZrO}_2$  in flowing 4%  $\text{H}_2/\text{N}_2$ . Room temperature to 1300 °C. Nickel metal is clearly seen at 900 °C, and no corundum formation is seen.

### C. High Temperature X-ray Diffraction – NiAl<sub>2</sub>O<sub>4</sub> + Additives

High temperature X-ray diffraction experiments up to 1100 °C in 20 ml/min flowing 4% H<sub>2</sub>/N<sub>2</sub> were conducted to evaluate the effects of 2.5 weight percent ZrO<sub>2</sub>, TiO<sub>2</sub> and Nb<sub>2</sub>O<sub>5</sub> on the kinetics of the transformation of metastable spinel phases to  $\Theta$ -Al<sub>2</sub>O<sub>3</sub> or  $\alpha$ -Al<sub>2</sub>O<sub>3</sub>. Figures 36 through 39 show the HTXRD patterns, starting at 30°C, then 600, 650, 700, 750, 800, 850, 900, 950, 1000, 1050, 1100, 900, 700, 500, 300, and finally 30 °C.

Undoped NiAl<sub>2</sub>O<sub>4</sub>, and the samples doped with ZrO<sub>2</sub> and Nb<sub>2</sub>O<sub>5</sub> formed metastable spinels phases after substantial reduction, shown in Figures 36 through 38. The metastable spinel peaks in both the ZrO<sub>2</sub> and Nb<sub>2</sub>O<sub>5</sub> sample appear to be less developed than in the undoped NiAl<sub>2</sub>O<sub>4</sub>. There is no clear difference between the behavior of the ZrO<sub>2</sub> and Nb<sub>2</sub>O<sub>5</sub> doped samples.

The behavior of the TiO<sub>2</sub> doped sample shown in Figure 39 is, however, very different. Corundum is seen at 1100 °C, and its phase fraction increases during cooling to 900 °C before the next pattern is obtained. A very small amount of TiO<sub>2</sub> is seen to have a very large effect to hasten the formation of corundum from metastable spinel phases. A comparison of the patterns obtained upon cooling for all samples is shown in Figure 40.

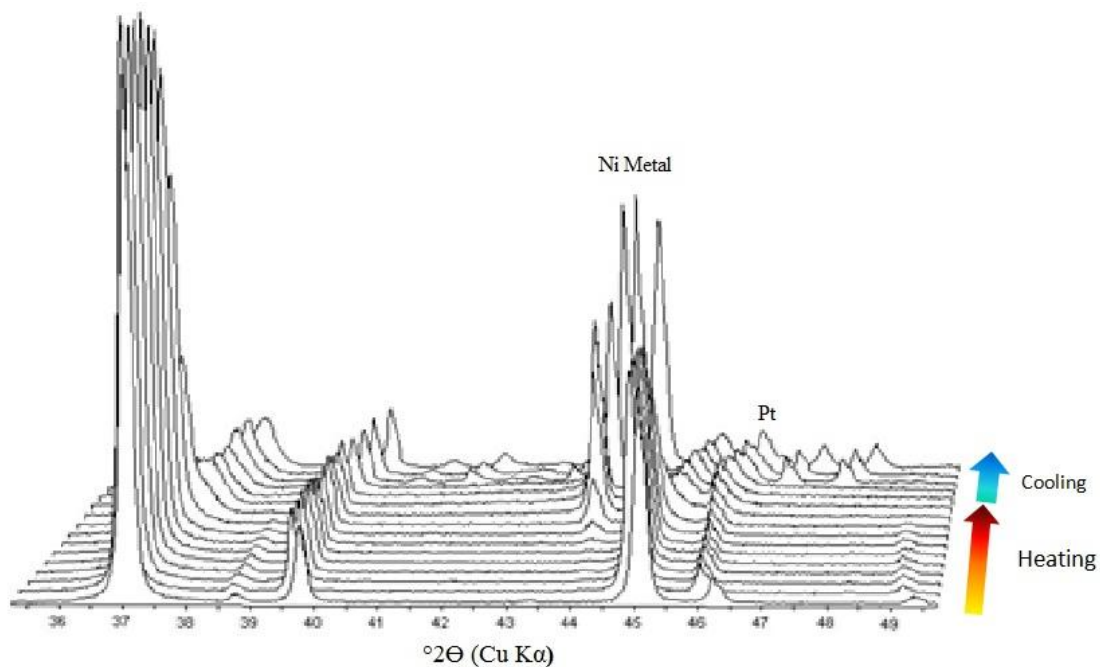


Figure 36. HTXRD of NiAl<sub>2</sub>O<sub>4</sub> in flowing 4% H<sub>2</sub>/N<sub>2</sub>. Room temperature to 1100 °C.

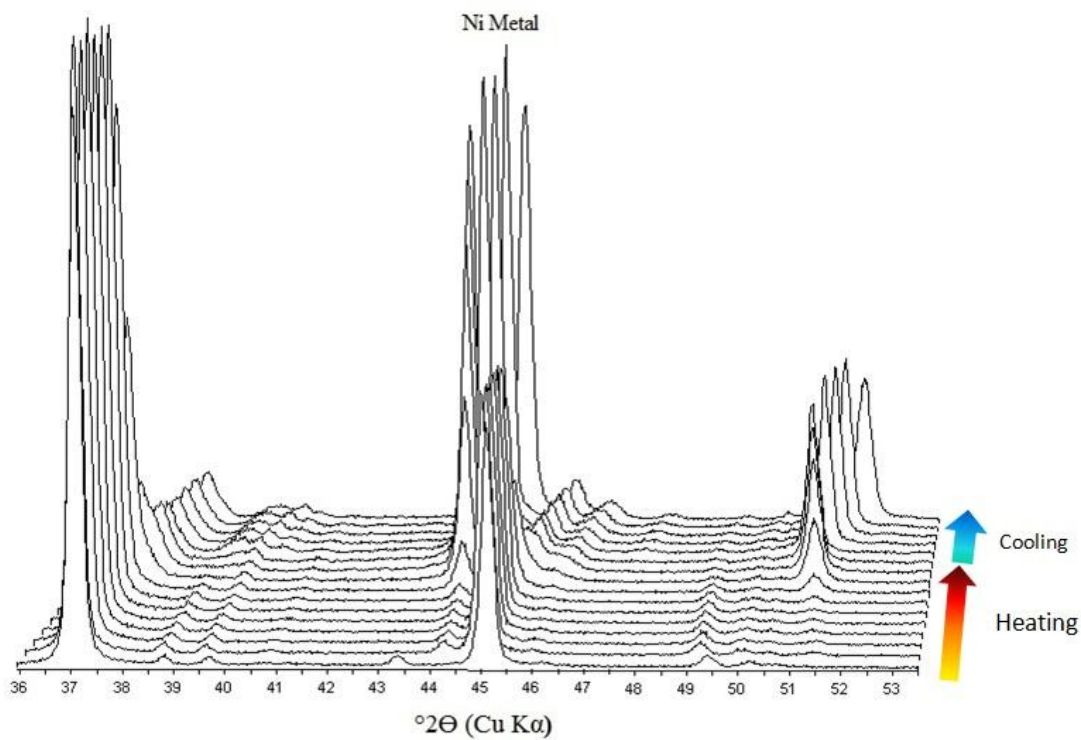


Figure 37. HTXRD of NiAl<sub>2</sub>O<sub>4</sub> + 2.5 wt% ZrO<sub>2</sub> in flowing 4% H<sub>2</sub>/N<sub>2</sub>. Room temperature to 1100 °C.

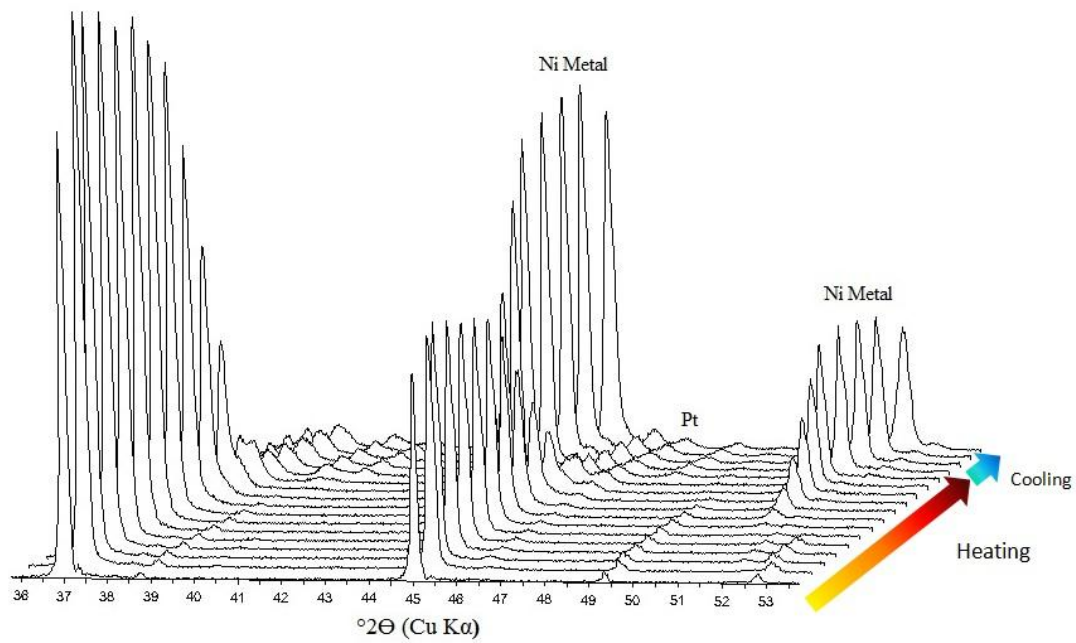


Figure 38. HTXRD of  $\text{NiAl}_2\text{O}_4 + 2.5 \text{ wt\% Nb}_2\text{O}_5$  in flowing 4%  $\text{H}_2/\text{N}_2$ . Room temperature to 1100 °C.

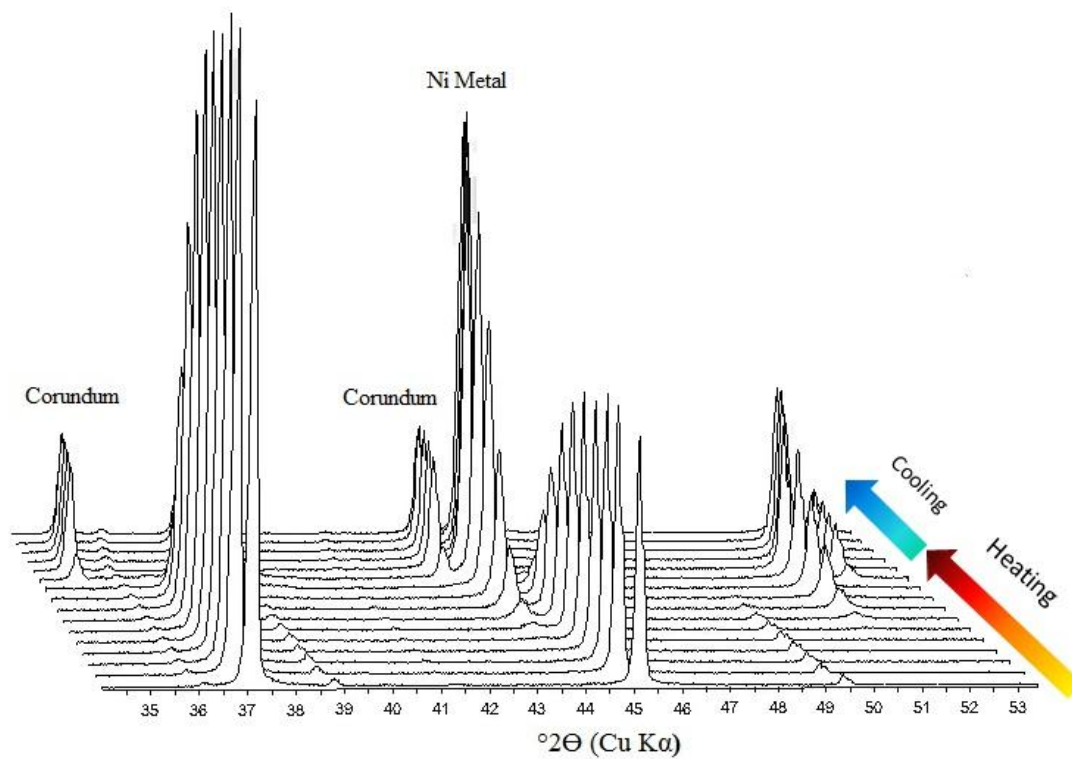


Figure 39. HTXRD of  $\text{NiAl}_2\text{O}_4 + 2.5 \text{ wt\% TiO}_2$  in flowing 4%  $\text{H}_2/\text{N}_2$ . Room temperature to 1100 °C. Corundum formation is seen at 1100 °C.

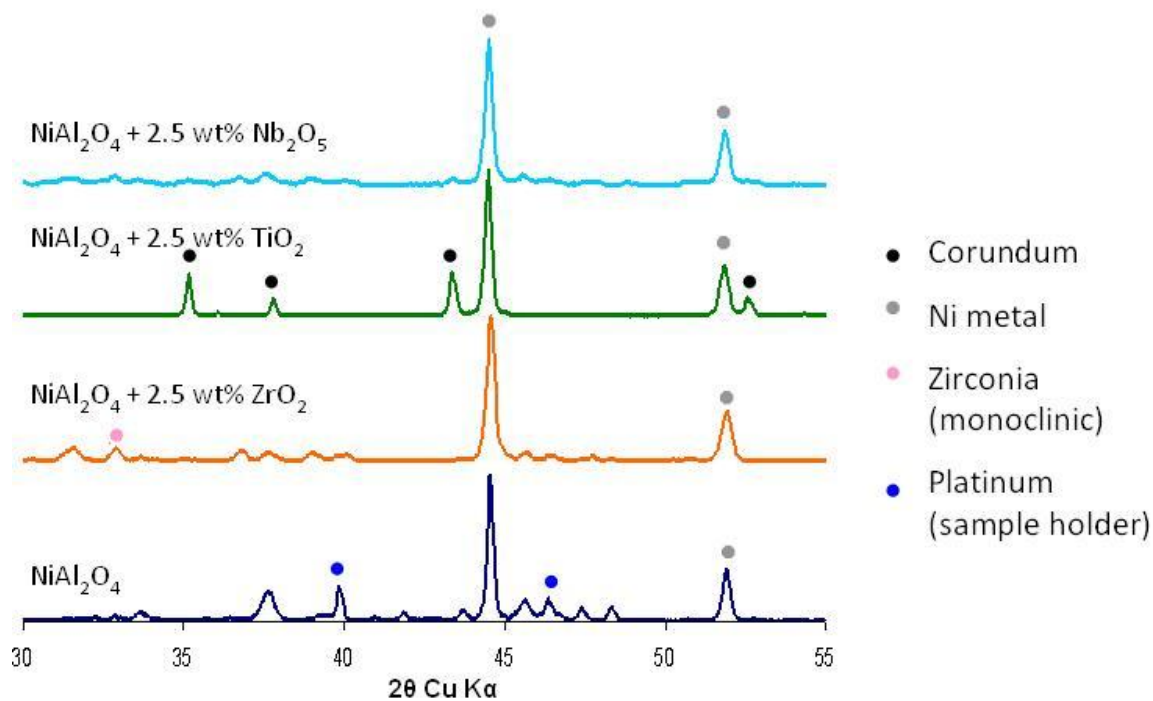


Figure 40. Final room temperature patterns of the  $\text{NiAl}_2\text{O}_4$  + additives HTXRD series.

#### D. Isothermal TGA/DTA

Figure 41 shows the results of the isothermal TGA experiments at 1000 °C. The dashed lines show the limit of weight loss for each composition on the basis of the loss of one oxygen ion for each nickel ion present.  $\text{NiAl}_2\text{O}_4$  + 2.5 wt%  $\text{ZrO}_2$  and  $\text{Ni}_{0.75}\text{Mg}_{0.25}\text{Al}_2\text{O}_4$  + 2.5 wt%  $\text{ZrO}_2$  did not reach their full weight loss during the 16 hour hold, so the measurement was repeated with the dwell time extended to 40 hours, for those two compositions only, which is shown in Figure 42. The 40 hour dwell time samples, rather than the 16 hour dwell time samples were used for  $\text{NiAl}_2\text{O}_4$  + 2.5 wt%  $\text{ZrO}_2$  and  $\text{Ni}_{0.75}\text{Mg}_{0.25}\text{Al}_2\text{O}_4$  + 2.5 wt%  $\text{ZrO}_2$  for X-ray diffraction and helium pycnometry.

The reduction kinetics of  $\text{Ni}_{0.75}\text{Mg}_{0.25}\text{Al}_2\text{O}_4$  are the fastest on a mass percent loss basis at 1000 °C, which explains results seen in the closed system reductions where at several temperatures, the  $\text{Ni}_{0.75}\text{Mg}_{0.25}\text{Al}_2\text{O}_4$  sample contains more nickel metal than does  $\text{NiAl}_2\text{O}_4$ . The kinetics of  $\text{NiAl}_2\text{O}_4$  and  $\text{Ni}_{0.5}\text{Mg}_{0.5}\text{Al}_2\text{O}_4$  are very similar, with  $\text{Ni}_{0.25}\text{Mg}_{0.75}\text{Al}_2\text{O}_4$  being the slowest. The differences in kinetics are likely due to the

specific phase formed at the surface in a very thin layer. Diffusion of reactants and products in this surface layer would likely be the controlling factor in the kinetics. Larger changes in the surface area caused by changes in volume, such as porosity or cracking would also affect the kinetics, but images of all compositions throughout the reduction are not available to make this comparison.

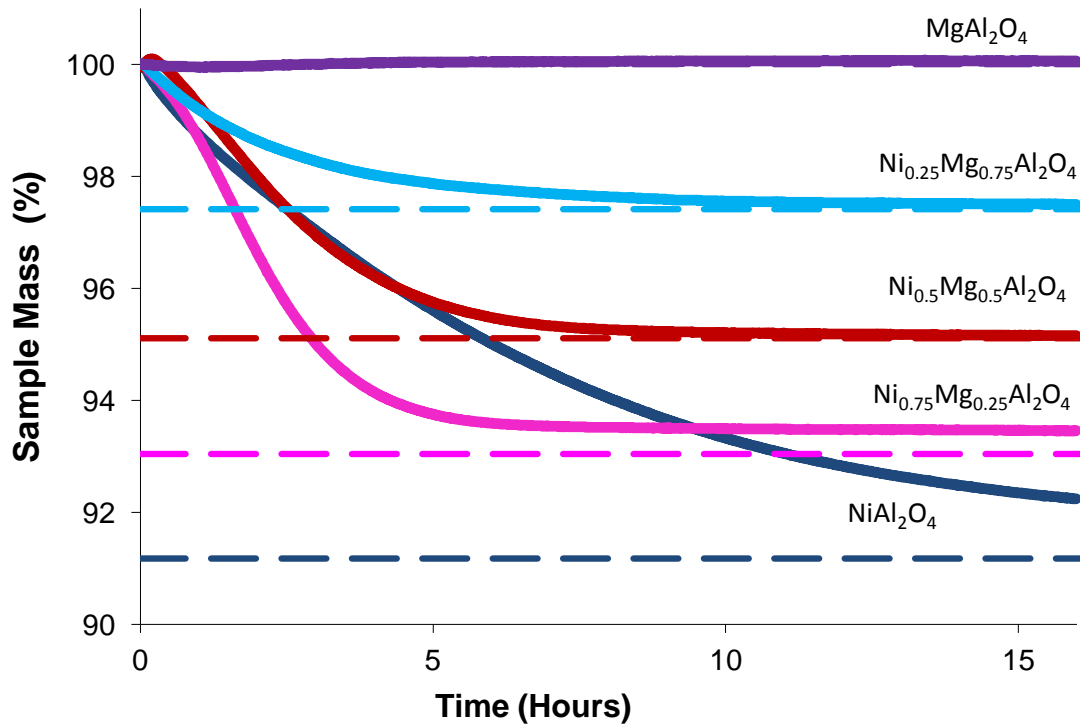


Figure 41. TGA at 1000 °C in 20 ml/min flowing 4% H<sub>2</sub>/Ar. All samples contained 2.5 wt% ZrO<sub>2</sub>.

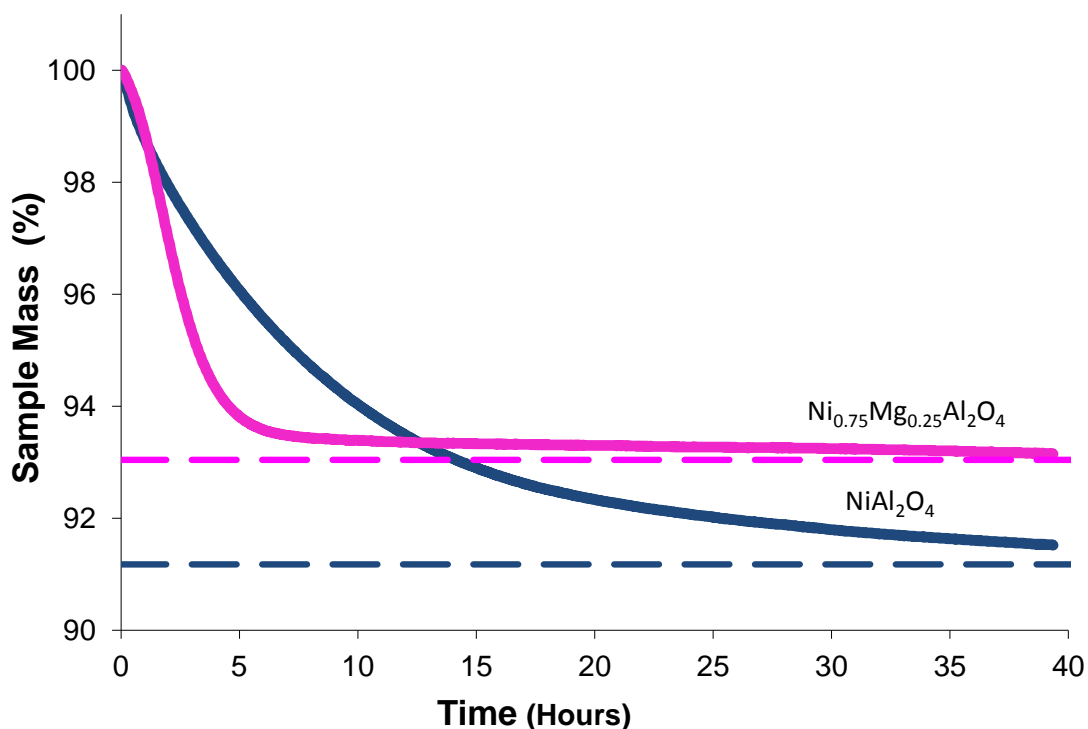


Figure 42. TGA at 1000 °C in 20 ml/min flowing 4% H<sub>2</sub>/Ar for an extended dwell for NiAl<sub>2</sub>O<sub>4</sub> and Ni<sub>0.75</sub>Mg<sub>0.25</sub>Al<sub>2</sub>O<sub>4</sub>. Both samples contained 2.5 wt% ZrO<sub>2</sub>.

The good agreement between the mass losses predicted by the stoichiometry of the compositions and the observed mass losses demonstrates that the spinels are of the targeted stoichiometries, which is always of concern when synthesizing spinels due to their ability to incorporate many different elements with only a small resultant lattice parameter change. In this particular instance, the volatilization of Ni would also affect the weight loss. One could argue that if the sample contained unreacted NiO, the observed weight losses would still agree with that of the stoichiometric spinels. This concern can be eliminated by examining the nonisothermal TGA experiments shown in Figure 46, where a 475 °C difference is seen in the onset temperature of reduction between NiO and the spinels. No weight loss is observed in the spinels at the onset temperature of reduction for NiO.

These results also show that Ni volatilization under these reaction conditions is insignificant, as the samples would lose more mass than that predicted by the defect

equation if Ni volatilization were to occur. Rather, a steady state is developed upon full reduction.

The DTA signal was small in magnitude compared to the DTA background due to the long time required to complete the reaction. The DTA signal was of little aid in sample characterization.

### **E. Nonisothermal TGA/DTA Experiments Motivation**

Early in the project, some reductions were performed with reducible masses greater than the controlled 3.30g of each composition used during later study. Upon examination of these powders after removing them from the furnace, there would sometimes be large differences in their appearance. Figure 43 shows the appearance of the spinels before reduction. A typical result of the preliminary reductions is shown in Figure 44. The  $x = 1$  and  $x = 0.75$  compositions were black, showing more than a small degree of reduction. The  $x = 0.5$  was a pale grayish color, and the  $x = 0.25$  composition remained the same shade of blue as before it was placed in the reduction furnace. This suggested that the final  $PO_2$  reached in the furnace was too high to reduce  $Ni_{0.25}Mg_{0.75}Al_2O_4$ , but was low enough to reduce the higher nickel compositions somewhat. X-ray diffraction patterns from the samples supported this, showing large nickel metal reflections for the  $x = 1$  and  $x = 0.75$  compositions, a small, broad peak just above background for the  $x = 0.5$  composition, and no nickel metal reflections from the  $x = 0.25$  composition. This suggests that the dissociation pressure necessary to form nickel metal decreases when MgO is substituted for NiO in  $Ni_xMg_{1-x}Al_2O_4$ .



Figure 43. Appearance of the spinel after calcination. From left to right:  $\text{Ni}_x\text{Mg}_{1-x}\text{Al}_2\text{O}_4$ ,  $x = 1, 0.75, 0.5, 0.25,$  and  $0$ .

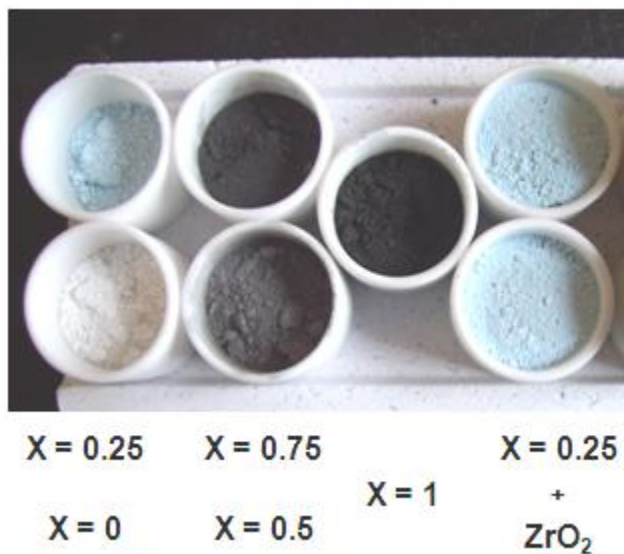


Figure 44. Common reduction result during early experiments when a larger reducible mass was used in the furnace.

In performing a nonisothermal (ramped) TGA experiment, the  $\text{PO}_2$  is varied with temperature at a constant atmospheric composition. The  $\text{PO}_2$  during the experiment is determined by the ratio of partial pressure of the flowing  $\text{H}_2$  purposefully introduced into the instrument, and the small level of contaminating water vapor present. If the partial pressure of  $\text{H}_2\text{O}$  is assumed to be constant for all temperatures, the  $\text{PH}_2\text{O}/\text{PH}_2$  ratio can be determined by measuring the temperature of the onset of reduction, as determined by the onset of weight loss, of one or more well characterized metal oxides. By determining

the  $\text{PH}_2\text{O}/\text{PH}_2$  ratio, the  $\text{PO}_2$  at any temperature for the system could be determined from phase equilibria calculations.

## **F. Nonisothermal TGA Experiments**

Unfortunately, using the reduction of NiO as a standard to determine the  $\text{H}_2/\text{H}_2\text{O}$  ratio in the furnace was unsuccessful, as it was necessary to use a very unrealistic value of  $\text{PH}_2\text{O}$  to match the  $\text{PO}_2$  to the temperature at which the NiO started to reduce. This could be due to a reaction with the amorphous carbon furnace tube, altering the  $\text{PO}_2$ , essentially meaning that the  $\text{H}_2/\text{H}_2\text{O}$  ratio is not solely responsible for the  $\text{PO}_2$  in the furnace. Alternatively, the observed temperature of reduction of the NiO could be due to kinetic effects preventing the reduction of NiO until a temperature significantly above the equilibrium point is reached. In the absence of a means to determine the  $\text{PO}_2$  dependence of the reduction of  $\text{Ni}_x\text{Mg}_{1-x}\text{Al}_2\text{O}_4$ , the temperature dependence will be examined instead, with the understanding that it is the combination of the temperature dependence of the  $\text{PO}_2$  and temperature which control the onset of reduction.

Figures 45 and 46 show the nonisothermal TGA measurements at a ramp rate of 2.5 and 1 K/min respectively. The gradual nature of the onset of reduction, even at the very slow ramp rates of 1 K/min and 2.5 K/min, also makes the determination of an exact onset of reduction temperature difficult. A stoichiometry dependent stability limit was demonstrated, but not as quantitatively as originally hoped. However, it can be noted that the onset of reduction temperature of  $\text{Ni}_{0.75}\text{Mg}_{0.25}\text{Al}_2\text{O}_4$ ,  $\text{Ni}_{0.5}\text{Mg}_{0.5}\text{Al}_2\text{O}_4$ , and  $\text{Ni}_{0.25}\text{Mg}_{0.75}\text{Al}_2\text{O}_4$  are much closer to each other than to that of  $\text{NiAl}_2\text{O}_4$ , which is noticeably lower.

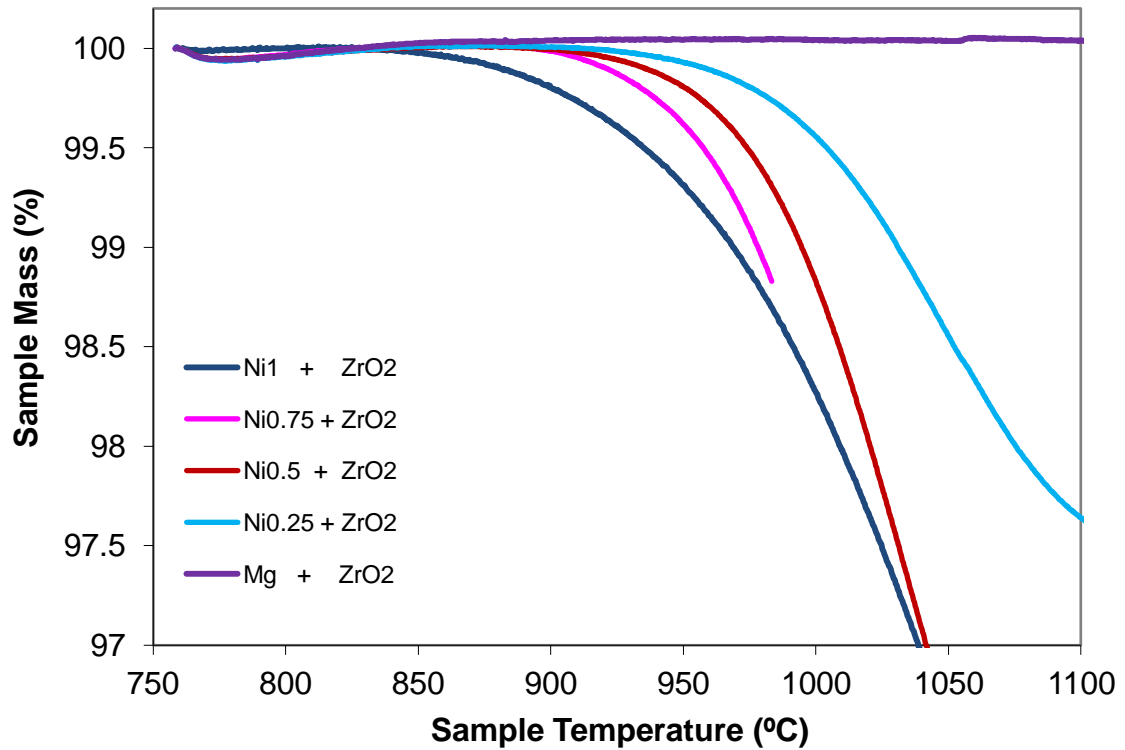


Figure 45. Non-isothermal TGA measurement began at 750 °C in 20 ml/min flowing 4% H<sub>2</sub>/Ar. Ramp rate was 1 K/min. Ni<sub>0.75</sub> measurement was ended early. The slight dip at the beginning of the measurement is a disturbance from the gas flow switching from He to 4% H<sub>2</sub>/N<sub>2</sub>.

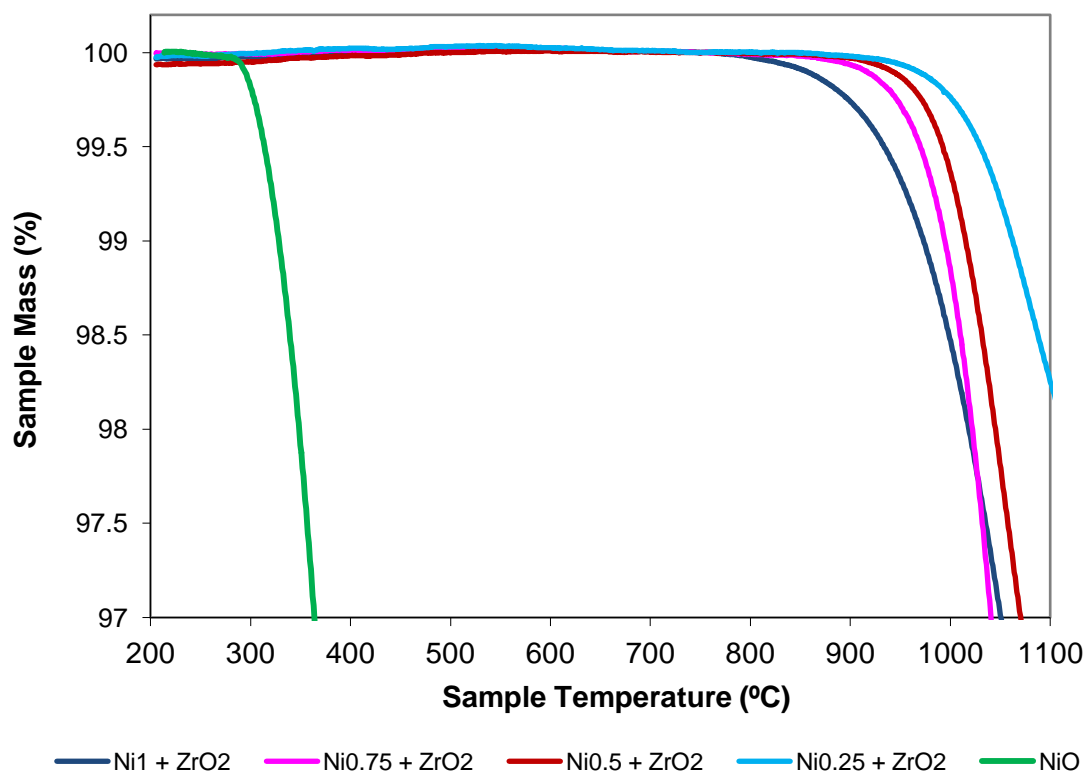


Figure 46. Non-isothermal TGA measurement began at 200 °C in 20 ml/min flowing 4% H<sub>2</sub>/Ar. The ramp rate was 2.5 K/min.

The much lower onset of reduction temperature of NiO should also be noted. NiO begins reduction at ~ 275 °C, whereas NiAl<sub>2</sub>O<sub>4</sub> does not begin to reduce until ~ 750 °C. This appears to conflict with the work of Elrefaie and Smeltzer<sup>35</sup> who determined the temperature and PO<sub>2</sub> dependence of the equilibria in the Ni-Al system by electrochemical means. They found that the PO<sub>2</sub> dependences of the Ni-NiO and NiAl<sub>2</sub>O<sub>4</sub> – Al<sub>2</sub>O<sub>3</sub> + Ni equilibria were very similar, i.e. within one order of magnitude. Given that electrochemical means should more accurately determine the thermodynamic equilibria than the method used here, the observed differences in the onset of reduction temperature are most likely due to kinetic effects.

Differences in the kinetics of reduction are also easily seen between NiAl<sub>2</sub>O<sub>4</sub> and the other compositions. The rate of reduction of Ni<sub>0.75</sub>Mg<sub>0.25</sub>Al<sub>2</sub>O<sub>4</sub> is very rapid compared to NiAl<sub>2</sub>O<sub>4</sub>. These kinetic differences are likely the result of differing rates of gas transport through their respective reaction layers. This is likely due to the differing

composition of their reaction layers, as similar microstructures form upon reduction for each microstructure, as observed by SEM.  $\text{NiAl}_2\text{O}_4$  appears to form  $\Theta\text{-Al}_2\text{O}_3$  more readily upon reduction, while  $\text{Ni}_{0.75}\text{Mg}_{0.25}\text{Al}_2\text{O}_4$  tends to retain metastable spinel phases.

### **G. Verification of Refined Nickel Phase Fraction by TGA**

In order to verify the nickel metal phase fractions determined by Rietveld refinement, samples of each composition reduced at 950 and 1100 °C were reduced in the Setaram SETSYS Evolution TGA in an isothermal hold at 1000 °C in 4%  $\text{H}_2/\text{Ar}$ , for 16 hours for  $\text{Ni}_{0.5}\text{Mg}_{0.5}\text{Al}_2\text{O}_4$  and  $\text{Ni}_{0.25}\text{Mg}_{0.75}\text{Al}_2\text{O}_4$ , and 40 hours for  $\text{NiAl}_2\text{O}_4$  and  $\text{Ni}_{0.75}\text{Mg}_{0.25}\text{Al}_2\text{O}_4$ . The weight loss that the already somewhat reduced samples underwent during the isothermal hold was compared to the total weight loss to calculate the nickel metal phase fraction. The comparison between the two methods of determination is shown in Figure 47. Very good agreement is seen for all samples - within ~ 2.5 wt%.

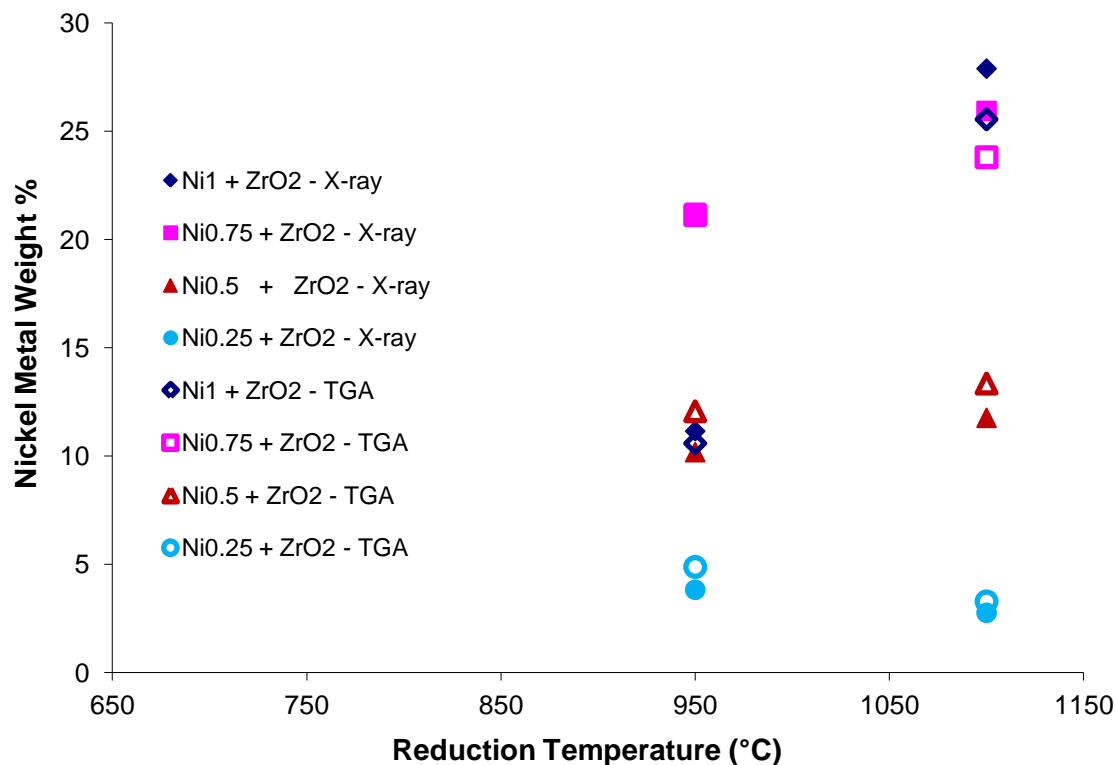


Figure 47. Comparison of nickel metal phase fraction as determined by Rietveld refinement of X-ray diffraction data and by an isothermal TGA run at 1000°C in 4% H<sub>2</sub>/Ar. The Ni<sub>0.75</sub>Mg<sub>0.25</sub>Al<sub>2</sub>O<sub>4</sub> reduced at 950 °C refinement and TGA data markers are on top of one another.

Volatilization of nickel from the reduced samples in the closed system furnace or the TGA would greatly complicate matters, but this was not expected to be a problem, as the vapor pressure of nickel metal at the highest temperature of reduction used, 1100 °C, is only  $6.7 \times 10^{-4}$  atm. Furthermore, no sign of nickel deposition onto the furnace tube was detected after reducing a total of 145 grams of spinel in the furnace.

## H. Spinel Density

As the reduction proceeds, the spinel density decreases due to the loss of the heavy Ni<sup>2+</sup> ion and the relative gain of the lighter Mg and Al. The lattice parameter decreases, decreasing the unit cell volume, but not enough to maintain its density. Despite the lowered density of the spinel, the composite increases in density due to the

gain of dense nickel metal. These trends are shown in Figure 48 for the various compositions. The composite density and the spinel density do not meet at the y-axis due to the 2.5 weight percent  $ZrO_2$  in the mixture.

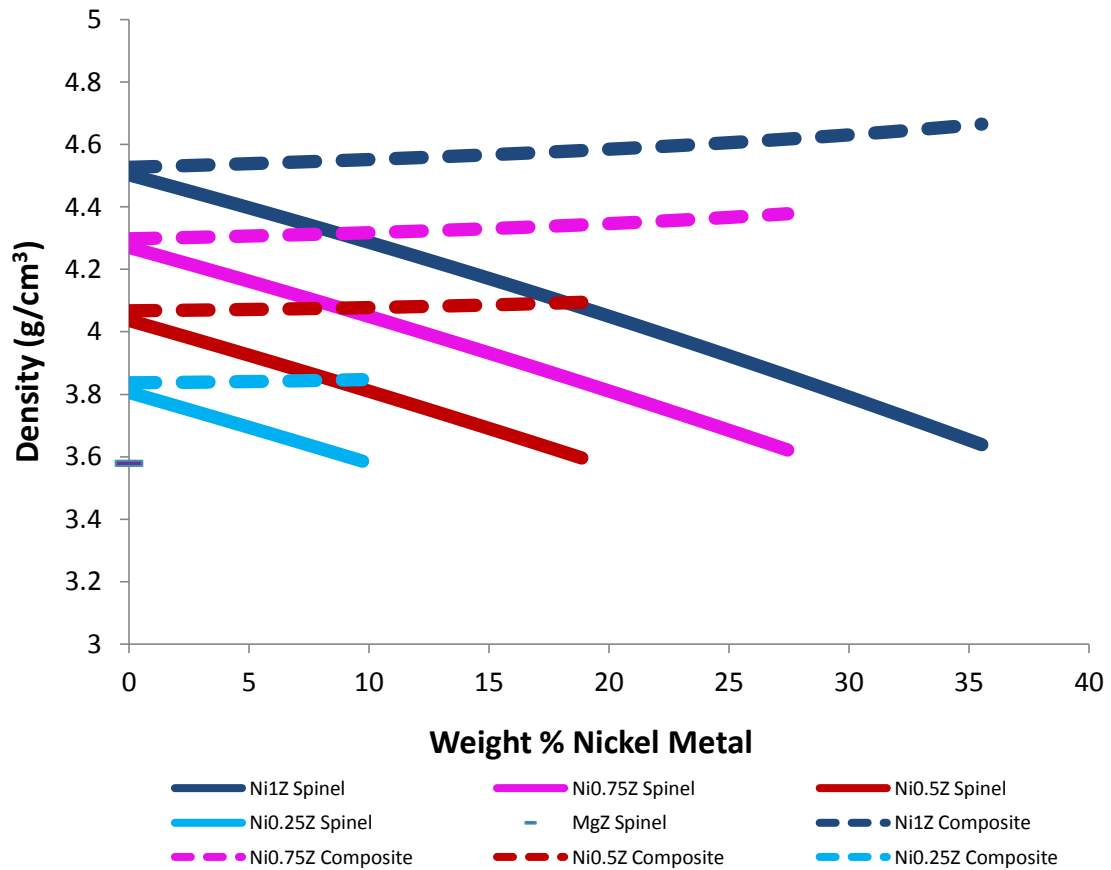


Figure 48. Composite and spinel density assuming the model of decreasing nickel, constant Mg/Al ratio, and full oxygen occupancy.

Figures 49 and 50 show the composite density of the closed-system reduced spinels, and the reduced in the TGA samples respectively, as measured by helium pycnometry. The nickel metal phase fraction for the ex-situ reduced samples was determined by Rietveld refinement. Weight loss in the TGA experiment was used to determine the nickel metal phase fraction for the reduced in the TGA samples. Agreement with the model is more satisfactory for the close-system reduced spinels than

for the reduced in the TGA spinels. This is due to the greater amount of sample available for the pycnometry measurement for the closed-system reduced spinels, 1g vs. ~ 0.1 g. Even when using a chamber insert to reduce the volume of the cell, measurement of the smaller sample mass was more sensitive to errors due to drift between the time the pycnometer was calibrated and the measurement was performed.

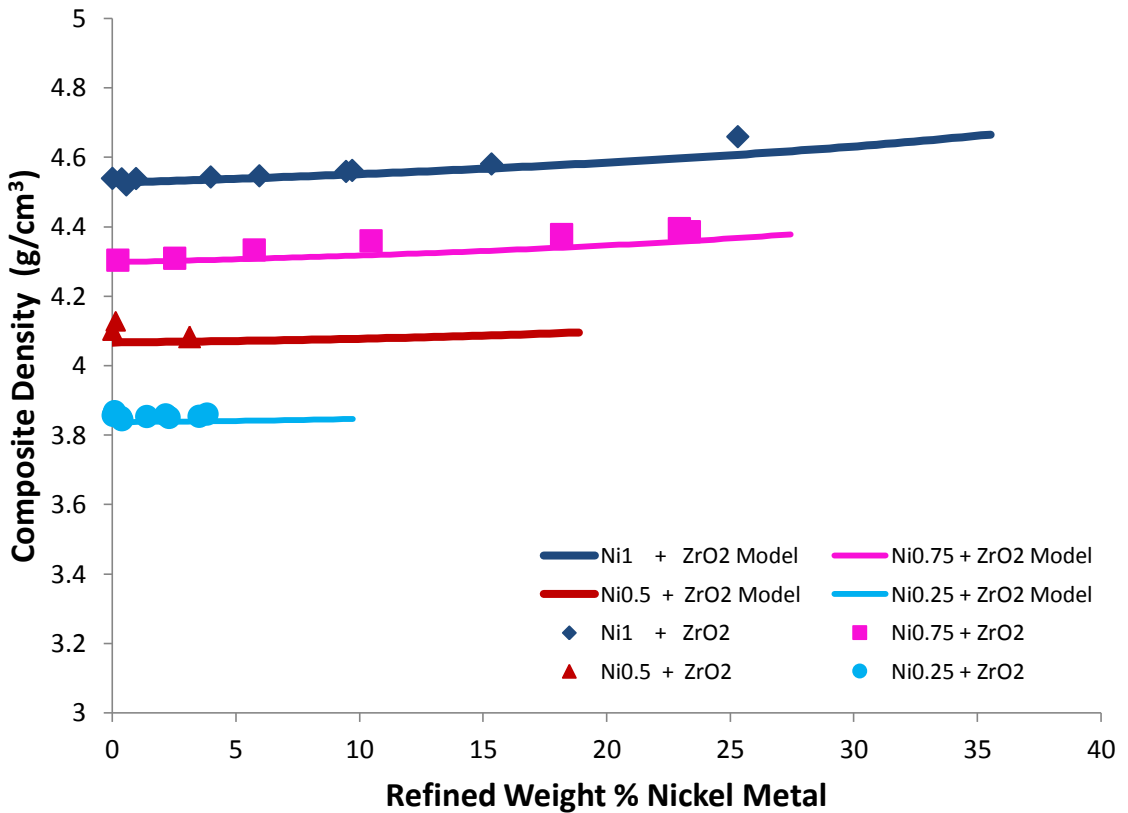


Figure 49. Composite density of spinels reduced in the closed system, plotted as a function of the refined weight percent nickel metal. Higher nickel metal content  $\text{Ni}_{0.5}\text{Mg}_{0.5}\text{Al}_2\text{O}_4$  compositions were produced, but not measured by pycnometry.

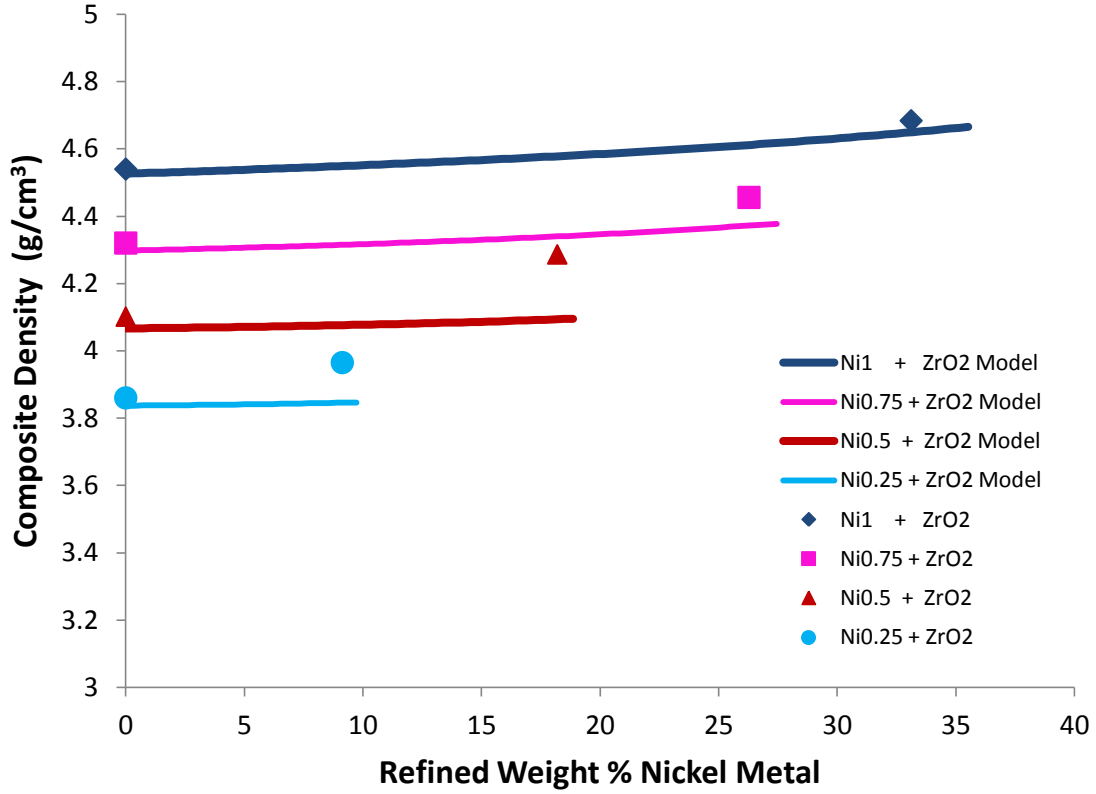


Figure 50. Unreduced mixture densities, and densities after reduction in the TGA as a function of nickel metal phase fraction as determined by weight loss. The  $\text{NiAl}_2\text{O}_4$  and  $\text{Ni}_{0.75}\text{Mg}_{0.25}\text{Al}_2\text{O}_4$  samples were reduced for 40 hours at 1000 °C in 4%  $\text{H}_2/\text{Ar}$ , the other compositions for 16 hours. Measured by helium pycnometry with a  $0.1 \text{ cm}^3$  chamber insert.

The density of the spinel can be extracted from the composite density via the rule of mixtures<sup>52</sup>.

$$\rho_c = \frac{1}{\frac{M_1}{\rho_1} + \frac{M_2}{\rho_2} + \frac{M_3}{\rho_3}} \quad (13)$$

Where  $\rho_c$  is the composite density,  $M_i$  is the mass fraction of the  $i$ th component, and  $\rho_i$  is the density of the  $i$ th component. Solving for the density of component 1:

$$\rho_1 = \frac{M_1}{\frac{1}{\rho_c} - \frac{M_2}{\rho_2} - \frac{M_3}{\rho_3}} \quad (14)$$

As the sample loses mass during the reduction, the mass fraction of  $\text{ZrO}_2$  increases from its starting 2.5 %. This varies in a predictable manner and can be accounted for. Thus

with a measured composite density, a nickel mass fraction from Rietveld refinement of X-ray diffraction data or weight loss in a TGA experiment, and the known densities of 8.908 g/cm<sup>3</sup> for nickel metal and 5.68 g/cm<sup>3</sup> for ZrO<sub>2</sub>, the remnant spinel density can be calculated.

Figure 51 shows the spinel densities extracted from the composite density as a function of nickel metal phase fraction. Very good agreement is seen between the calculated densities and that predicted by the Al and Mg rich, full oxygen occupancy spinel model, confirming the conclusions of the Rietveld refinements of the X-ray diffraction data.

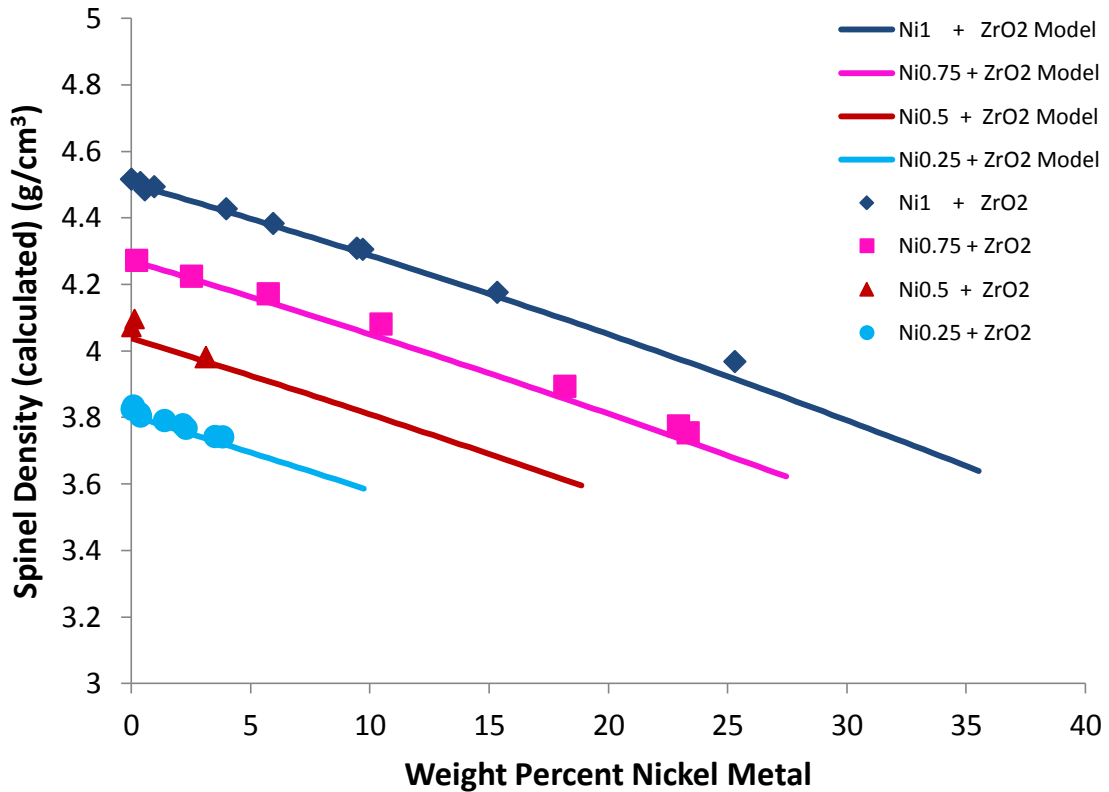


Figure 51. Remnant spinel density of samples reduced in the closed system, calculated from the composite density and the refined nickel metal phase fraction. Higher nickel metal content Ni<sub>0.5</sub>Mg<sub>0.5</sub>Al<sub>2</sub>O<sub>4</sub> compositions were produced but not measured by pycnometry.

Samples containing metastable spinel phases also show good agreement with the nonstoichiometric spinel model, which is indicative that the density of the metastable spinel phases is close to that of  $\text{Al}_2\text{O}_3$  rich spinels of the same composition, which is as expected.

Confirmation of the claim by Okuyama as to the presence of a small number of oxygen vacancies, one  $V_{\text{O}}^{\bullet\bullet}$  for every 17 excess  $\text{Al}_2\text{O}_3$  in  $\text{Al}_2\text{O}_3$ -rich  $\text{MgAl}_2\text{O}_4$ , cannot be made. Such a small difference cannot be detected by this method due to the uncertainty in the spinel density brought on by uncertainty in the phase fractions of nickel metal and  $\text{ZrO}_2$ .

### **I. X-Ray Diffraction of TGA-Reduced Samples**

Samples reduced in the TGA for 16 or 40 hours were examined by X-ray diffraction to determine their phase compositions, as shown in Figures 52 through 56.  $\text{MgAl}_2\text{O}_4 + 2.5 \text{ wt\% ZrO}_2$  reduced for 16 hours at 1000 °C contained only baddeleyite, tetragonal  $\text{ZrO}_2$ , and  $\text{MgAl}_2\text{O}_4$ , shown in Figure 52.  $\text{Ni}_{0.25}\text{Mg}_{0.75}\text{Al}_2\text{O}_4 + 2.5 \text{ wt\% ZrO}_2$  and  $\text{Ni}_{0.5}\text{Mg}_{0.5}\text{Al}_2\text{O}_4 + 2.5 \text{ wt\% ZrO}_2$  were found to contain only nickel metal, baddeleyite, tetragonal  $\text{ZrO}_2$ , and spinel, shown in Figures 53 and 54 respectively.

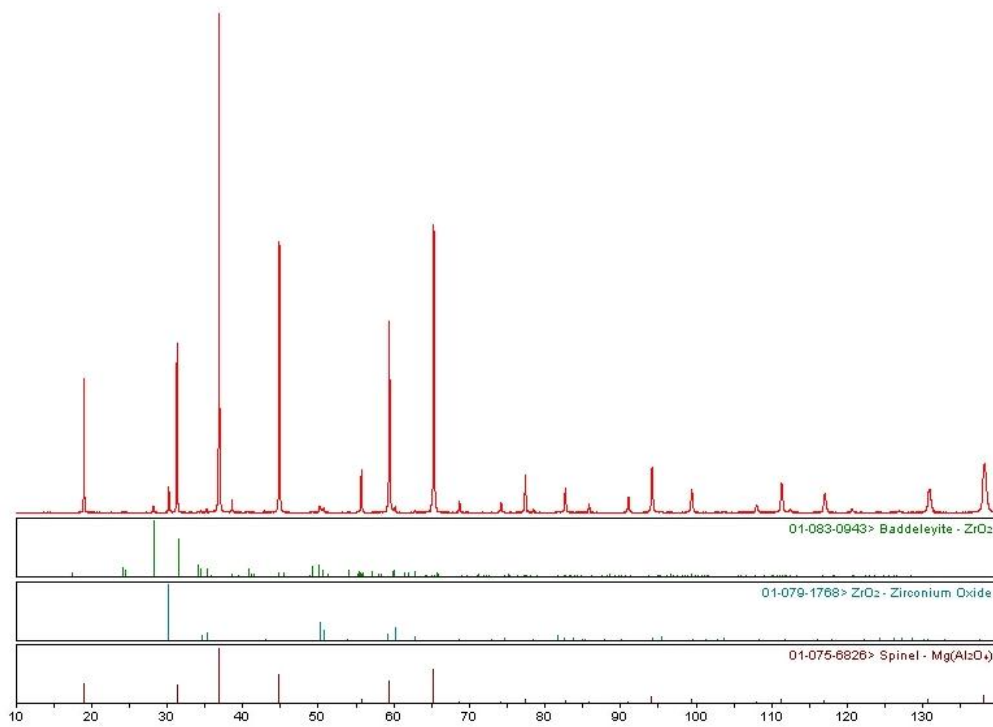


Figure 52. X-Ray diffraction pattern and phase identification of  $\text{MgAl}_2\text{O}_4 + 2.5 \text{ wt\% ZrO}_2$  after 16 hours at  $1000 \text{ }^\circ\text{C}$  in  $4\% \text{ H}_2/\text{Ar}$ . Reflections are shown for baddeleyite, tetragonal  $\text{ZrO}_2$ , and spinel

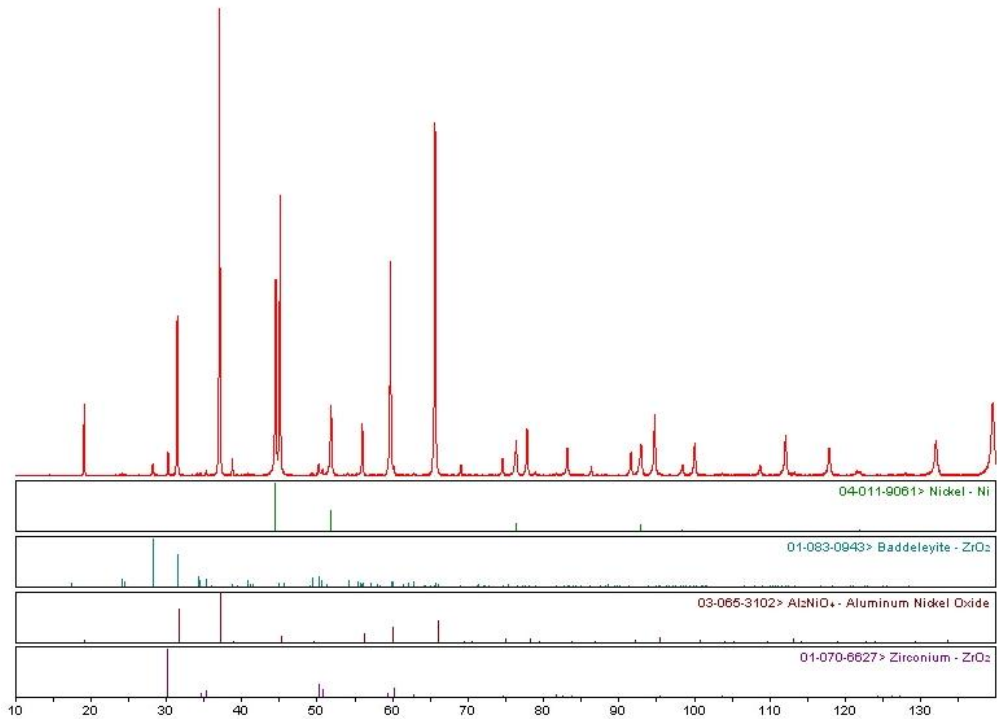


Figure 53. X-Ray diffraction pattern and phase identification of  $\text{Ni}_{0.25}\text{Mg}_{0.75}\text{Al}_2\text{O}_4 + 2.5 \text{ wt\% ZrO}_2$  after 16 hours at 1000 °C in 4%  $\text{H}_2/\text{Ar}$ . Reflections are shown for nickel metal baddeleyite, spinel and tetragonal  $\text{ZrO}_2$ .

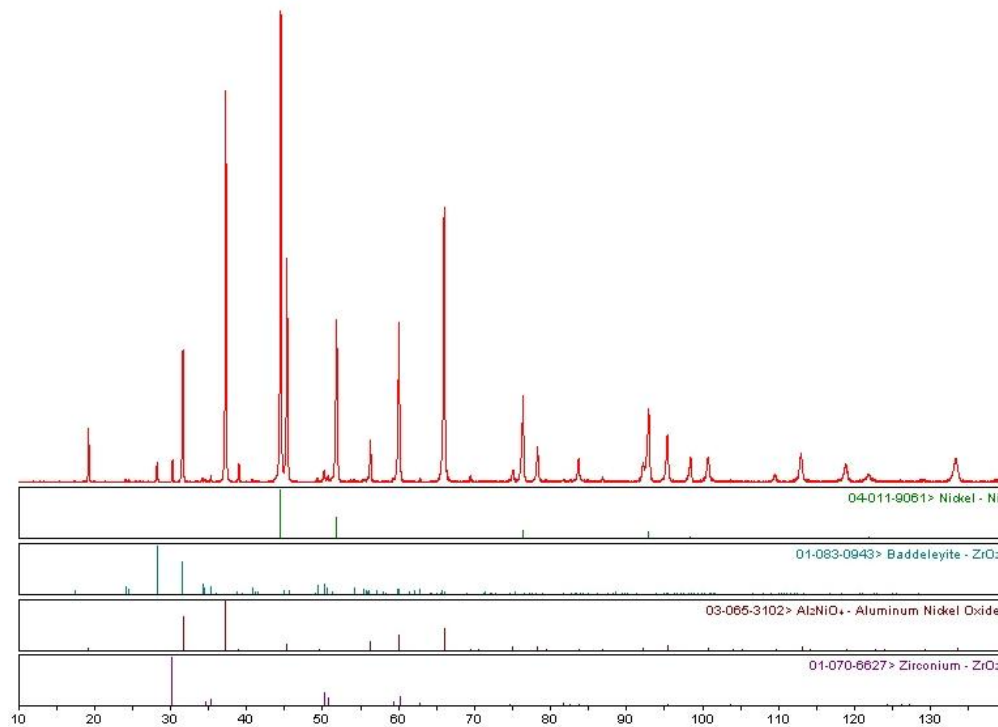


Figure 54. X-Ray diffraction pattern and phase identification of  $\text{Ni}_{0.5}\text{Mg}_{0.5}\text{Al}_2\text{O}_4 + 2.5 \text{ wt\% ZrO}_2$  after 16 hours at 1000 °C in 4%  $\text{H}_2/\text{Ar}$ . Reflections are shown for nickel metal, baddeleyite, spinel and tetragonal  $\text{ZrO}_2$ .

$\text{Ni}_{0.75}\text{Mg}_{0.25}\text{Al}_2\text{O}_4 + 2.5 \text{ wt\% ZrO}_2$  was found to contain nickel metal, baddeleyite, tetragonal  $\text{ZrO}_2$ , a very small amount of spinel, and either  $\text{NiAl}_{10}\text{O}_{16}$  or  $\text{NiAl}_{32}\text{O}_{49}$ , as shown in Figure 55. The specific defect spinel phase was present could not be distinguished by powder diffraction. Single crystal diffraction or in-depth TEM investigations are sometimes necessary to distinguish one metastable spinel phase from another<sup>41</sup>.

$\text{NiAl}_2\text{O}_4 + 2.5 \text{ wt\% ZrO}_2$  was found to contain nickel metal, baddeleyite, tetragonal  $\text{ZrO}_2$ ,  $\Theta\text{-Al}_2\text{O}_3$ , and  $\text{NiAl}_{32}\text{O}_{49}$ , as shown in Figure 56.

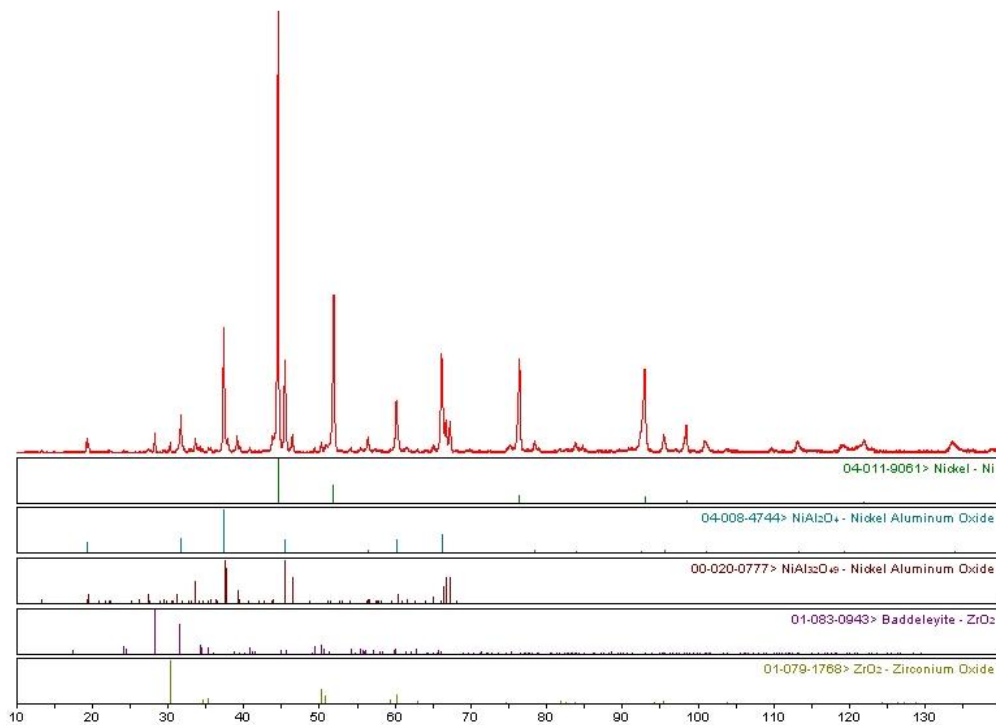


Figure 55. X-Ray diffraction pattern and phase identification of  $\text{Ni}_{0.75}\text{Mg}_{0.25}\text{Al}_2\text{O}_4 + 2.5 \text{ wt\% ZrO}_2$  after 40 hours at  $1000^\circ\text{C}$  in  $4\% \text{ H}_2/\text{Ar}$ . Reflections are shown for nickel metal, spinel,  $\text{NiAl}_{32}\text{O}_{49}$ , baddeleyite, and tetragonal  $\text{ZrO}_2$ .

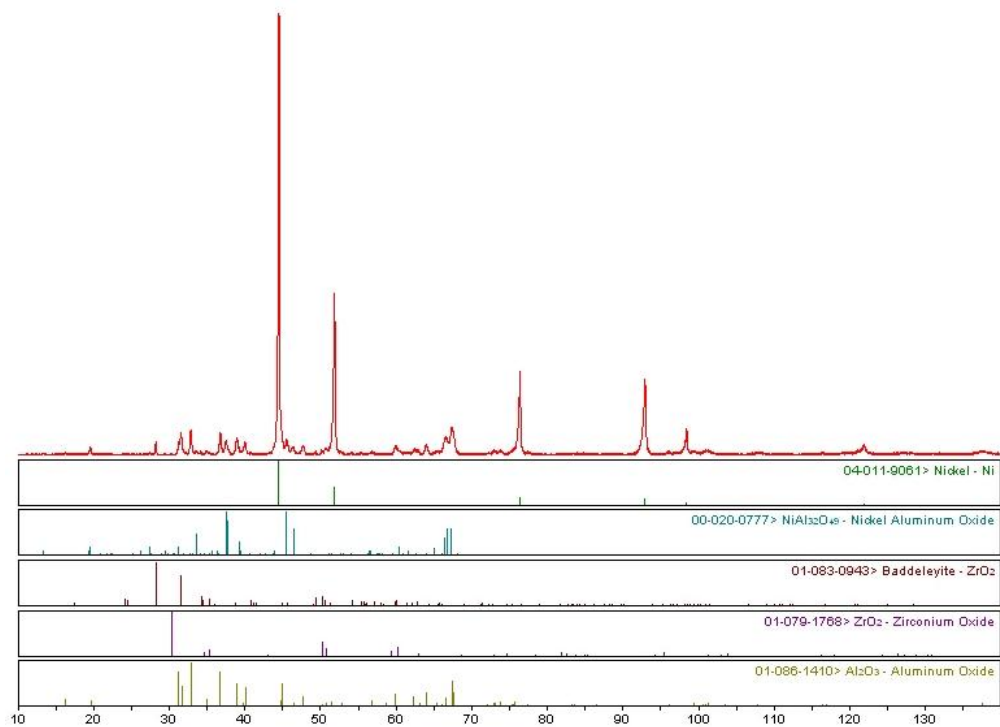


Figure 56. X-Ray diffraction pattern and phase identification of  $\text{NiAl}_2\text{O}_4 + 2.5$  wt%  $\text{ZrO}_2$  after 40 hours at 1000 °C in 4%  $\text{H}_2/\text{Ar}$ . Reflections are shown for nickel metal,  $\text{NiAl}_{32}\text{O}_{49}$ , baddeleyite, tetragonal  $\text{ZrO}_2$ , and theta alumina.

## J. $(\text{Ni},\text{Mg})\text{O} \cdot x\text{Al}_2\text{O}_3$ Phase Stability

A phase diagram for the  $\text{NiAl}_2\text{O}_4 - \text{MgAl}_2\text{O}_4 - \text{Al}_2\text{O}_3$  was constructed to provide information on the phase stability of the ternary system. Pseudo-binary phase diagrams are available for  $\text{NiAl}_2\text{O}_4 - \text{Al}_2\text{O}_3$  and  $\text{MgAl}_2\text{O}_4 - \text{Al}_2\text{O}_3$  in Phase Equilibria Diagrams,<sup>53,54</sup> numbers 2323 and 9908 respectively. The  $\text{Al}_2\text{O}_3$  solubility of the  $\text{NiAl}_2\text{O}_4 - \text{MgAl}_2\text{O}_4$  solid solution is not well determined. Figure 57 constructs the compositional space containing the compositions of interest. Blue tie lines show the path the composition of the remnant spinel takes as nickel is reduced from the spinel. Movement towards the  $\text{MgO} - \text{Al}_2\text{O}_3$  pseudo-binary along the tie line gives a constant Mg-Al ratio.

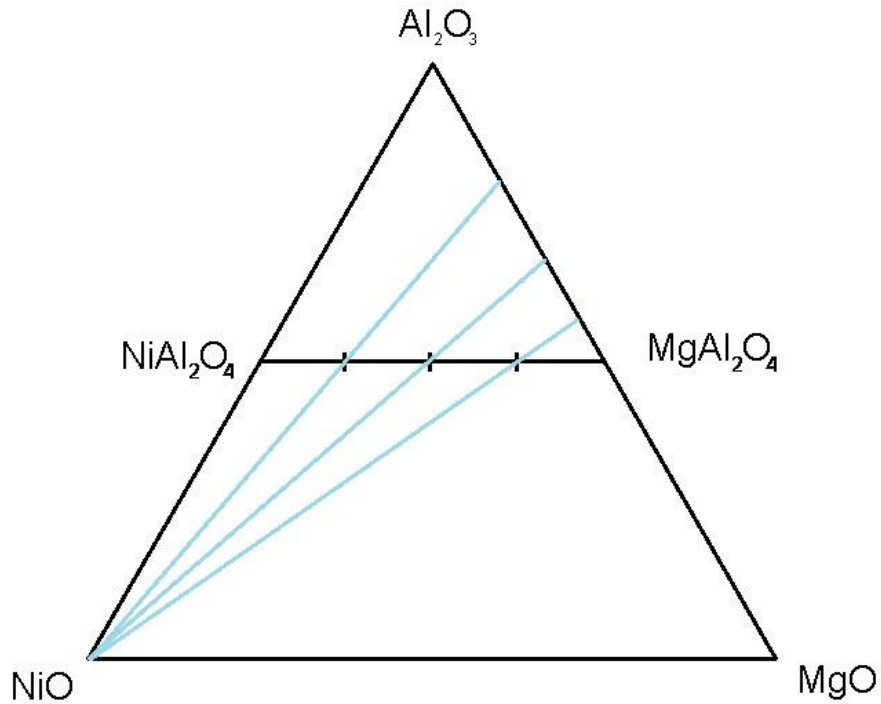


Figure 57.  $\text{Al}_2\text{O}_3 - \text{NiO} - \text{MgO}$  phase diagram showing the  $\text{Ni}_x\text{Mg}_{1-x}\text{Al}_2\text{O}_4$  compositions  $x = 0.75, 0.5,$  and  $0.25$  used in this study. Tie lines show the development of the remnant spinel composition as nickel ions in the spinel are reduced to nickel metal.

Figure 58 shows the  $\text{Al}_2\text{O}_3$  stability limits for the pseudo-binary systems; the  $\text{NiAl}_2\text{O}_4$  and  $\text{NiAl}_2\text{O}_4 + \text{Corundum}$  boundary being from Rotan et al.<sup>21</sup> The  $\text{MgAl}_2\text{O}_4 - \text{Al}_2\text{O}_3$  pseudo-binary system has been studied more extensively, and a temperature dependence of  $\text{Al}_2\text{O}_3$  solubility is available,<sup>19</sup> and is projected onto the 1-D phase diagram of Figure 58.

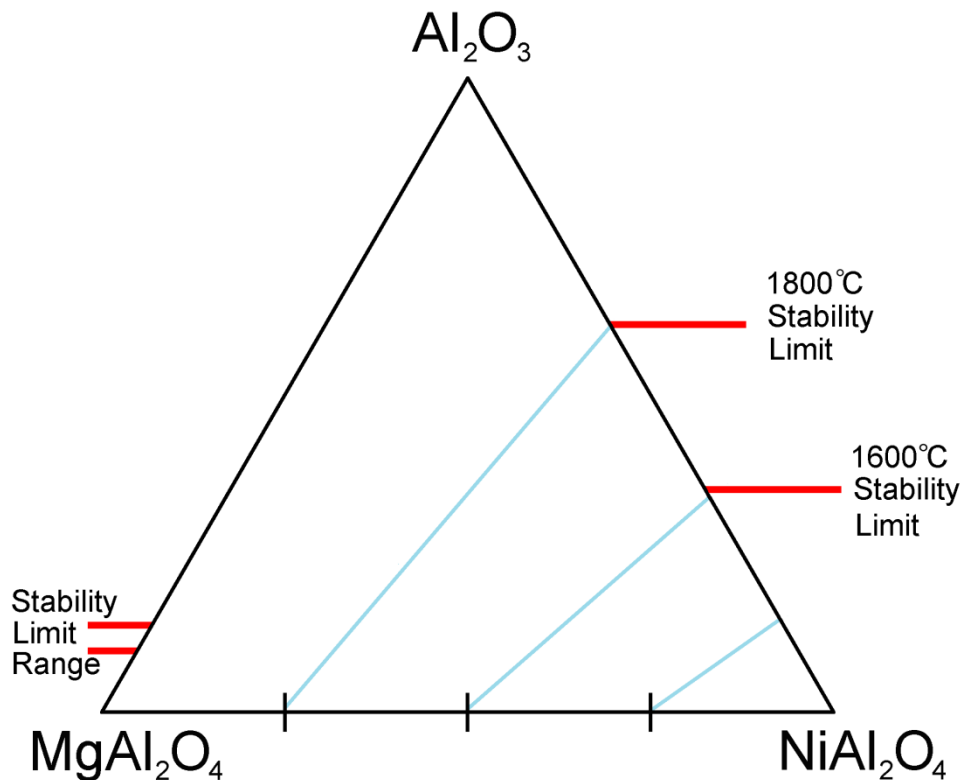


Figure 58.  $\text{NiAl}_2\text{O}_4 - \text{MgAl}_2\text{O}_4 - \text{Al}_2\text{O}_3$  phase stability diagram. Stability limit between  $\text{NiAl}_2\text{O}_4$  and  $\text{NiAl}_2\text{O}_4 + \text{Corundum}$  from Rotan et al. is shown<sup>21</sup>. The  $\text{MgAl}_2\text{O}_4 - \text{Al}_2\text{O}_3$  pseudo-binary system has been studied more extensively, and a temperature dependence is available.<sup>19</sup>

Figure 59 shows which calculated remnant spinel compositions contained only spinel, and which contained metastable spinel or transition aluminas. Samples produced by both closed system reduction and by TGA are included in the plot. Nickel metal content was determined by Rietveld refinement for the closed-system reduced samples and by weight loss for the reduced in the TGA samples.

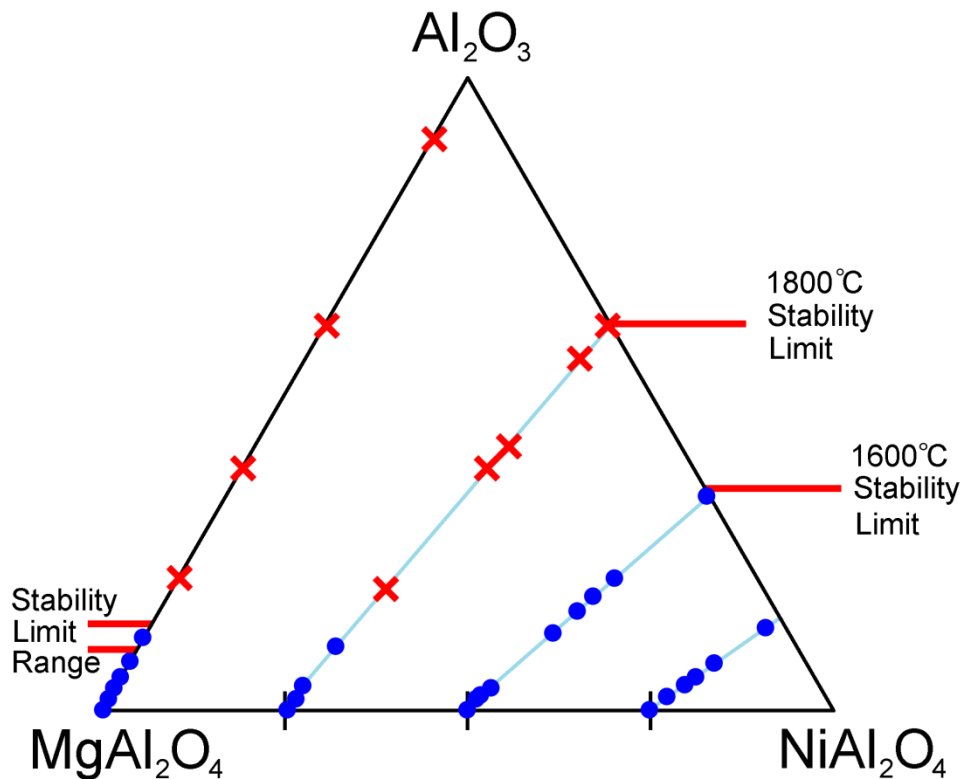


Figure 59. Derived phase stability diagram, showing the remnant spinel compositions which were stable after reduction as blue dots, and the unstable compositions as red X's.

The remnant spinel composition was calculated using the refined nickel metal content rather than the spinel stoichiometry, which was also refined. The nickel metal phase fraction is a more reliable measure, as confirmed by TGA analysis of the spinels reduced at 950 and 1000 °C. Refinement of the spinel stoichiometry is complicated by correlating variables such as the thermal parameters, inversion, and oxygen parameter. The calculated remnant spinel compositions are given in Appendix 2.

The emergence of lines belonging to a metastable spinel phase was taken as evidence that the remnant spinel composition was no longer in the spinel phase stability region, but instead in the spinel + corundum phase stability region, as given sufficient time to reach equilibrium, a metastable spinel phase will transform to corundum and spinel at the limiting composition.

Unfortunately, no temperature dependence can be deduced via this method.  $\text{Al}_2\text{O}_3$  solubility is known to increase with increasing temperature in both the  $\text{NiAl}_2\text{O}_4 - \text{Al}_2\text{O}_3$  and  $\text{MgAl}_2\text{O}_4 - \text{Al}_2\text{O}_3$  pseudobinary systems, and as such, the room temperature measurements should approximate a minimum in the  $\text{Al}_2\text{O}_3$  solubility. It is possible that some of the remnant spinel compositions were stable at the reduction temperature, but passed into the spinel + corundum region upon cooling and formed metastable spinel phases as a result. Uncertainties in composition are greater using this method than those typically used when determining a phase diagram, but this method does provide valuable information as to the shape of the spinel phase stability boundary line, which was not available previously.

## **K. Spinel Surfaces**

The morphology of the spinel phase undergoes drastic changes as the reduction proceeds. Figures 60 and 61 show the highly stepped, angular nature of the as-synthesized  $\text{NiAl}_2\text{O}_4$ .  $\text{ZrO}_2$  appears to be preferentially located at grain boundaries, and some  $\text{ZrO}_2$  can be seen on top of the grains. As the spinel is reduced, the stepped nature diminishes with higher treatment temperature, or extent of reduction, which are effectively linked in this study. Microstructures of reduced spinels can be seen in Figures 63 through 73, spanning reduction temperatures of 750 to 1100 °C.  $\text{NiAl}_2\text{O}_4$  reduced at 650 and 700 °C were previously shown as Figures 18 and 19. As can be seen in the LVSEM image of Figure 67, substantial amounts of material are missing in the vicinity of the steps, suggesting preferential mass transport from the steps. This cannot be seen by SEM at 900 or 950°C, but is apparent in Figure 70, which was reduced at 1000 °C. By 1000 °C, the stepped microstructure has largely disappeared, and there is no trace of it remaining at 1100 °C.

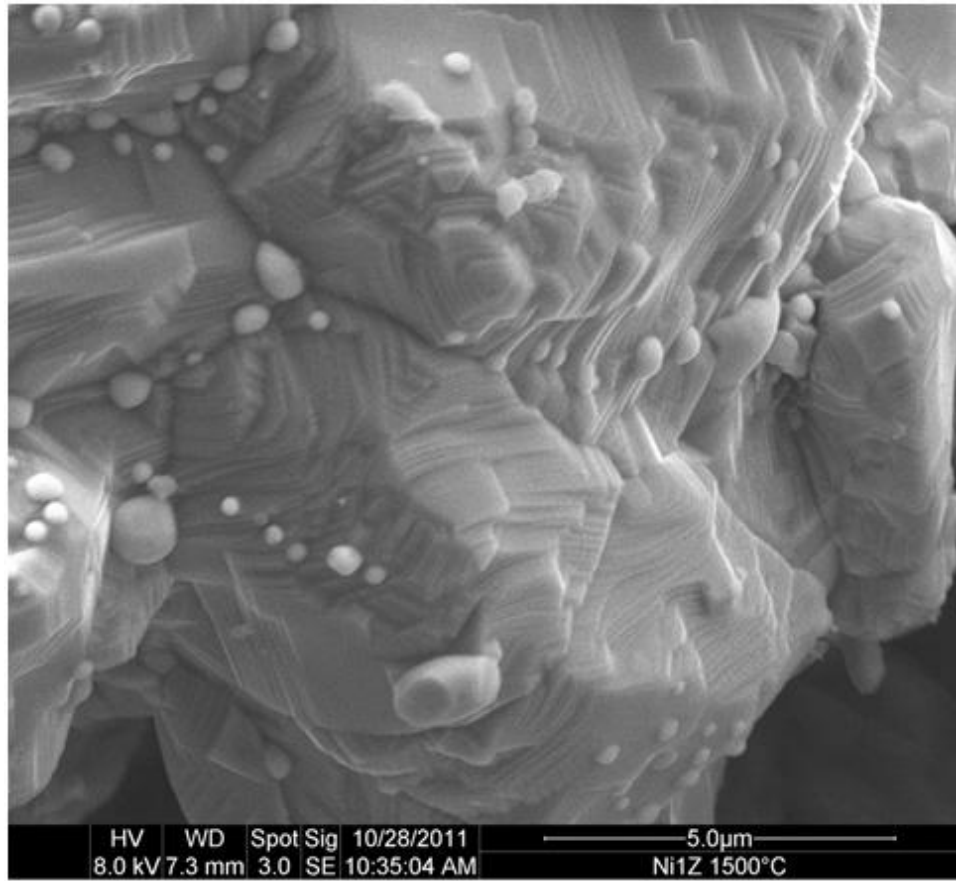


Figure 60. Secondary electron image of  $\text{NiAl}_2\text{O}_4 + 2.5 \text{ wt\% ZrO}_2$ , calcined for 8 hours at 1500 °C. 10 kX original magnification.

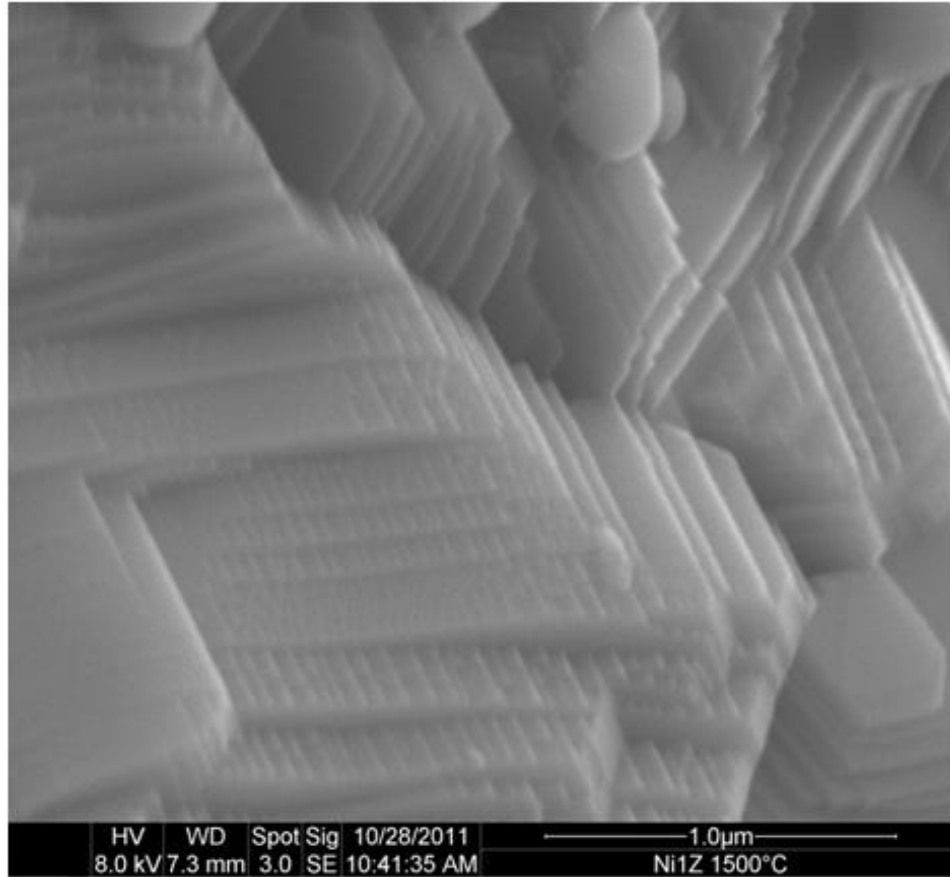


Figure 61. Secondary electron image of  $\text{NiAl}_2\text{O}_4 + 2.5 \text{ wt\% ZrO}_2$ , calcined for 8 hours at  $1500 \text{ }^\circ\text{C}$ . The highly stepped surface of the oxide is easily seen, which is lost as the oxide is reduced at higher temperatures. 50 kX original magnification.

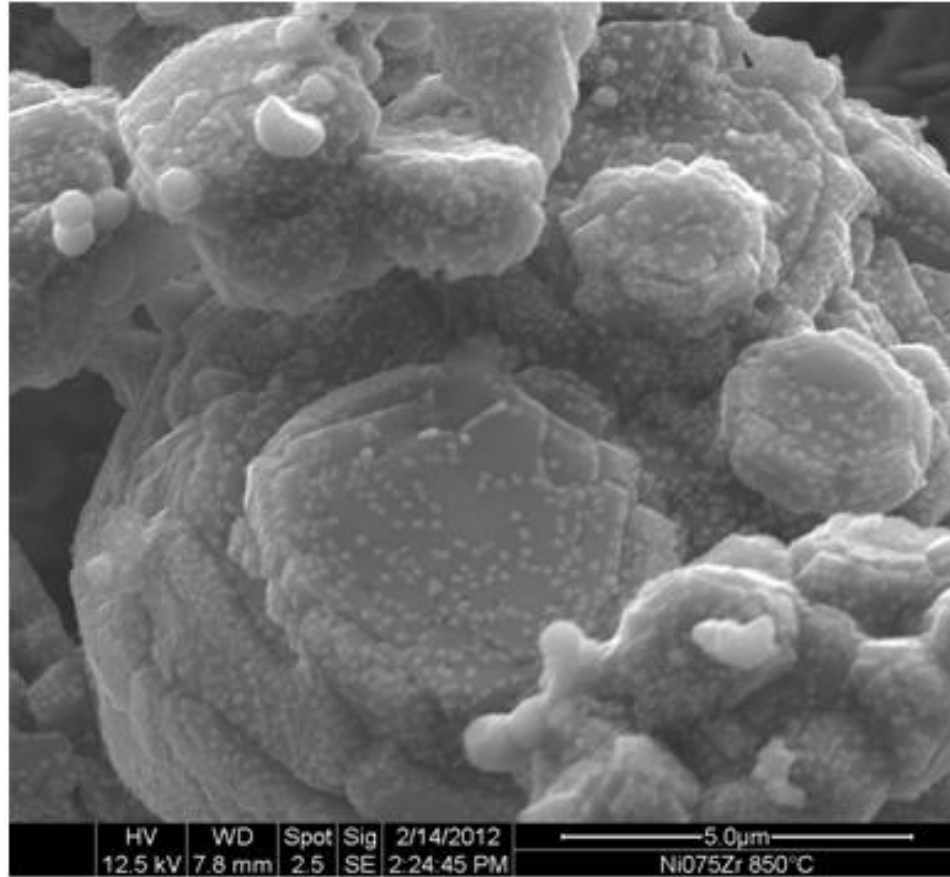


Figure 62. Secondary electron image of  $\text{Ni}_{0.75}\text{Mg}_{0.25}\text{Al}_2\text{O}_4 + 2.5 \text{ wt\% ZrO}_2$ , reduced at 850 °C in 300 Torr  $\text{H}_2$  for 24 hours. 10 kX original magnification.

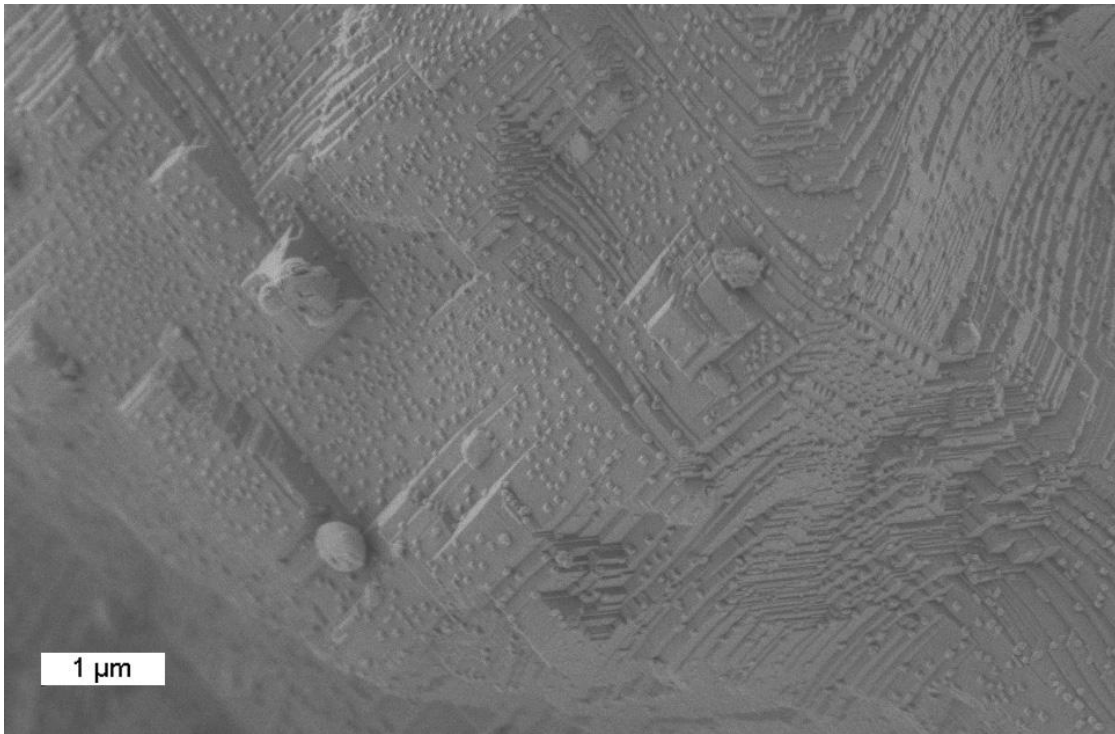


Figure 63. Low-voltage secondary electron image of  $\text{NiAl}_2\text{O}_4 + 2.5 \text{ wt\% ZrO}_2$ , reduced at  $750 \text{ }^\circ\text{C}$  in 300 Torr  $\text{H}_2$  for 29 hours. 0.45 kV, 30 kX original magnification.

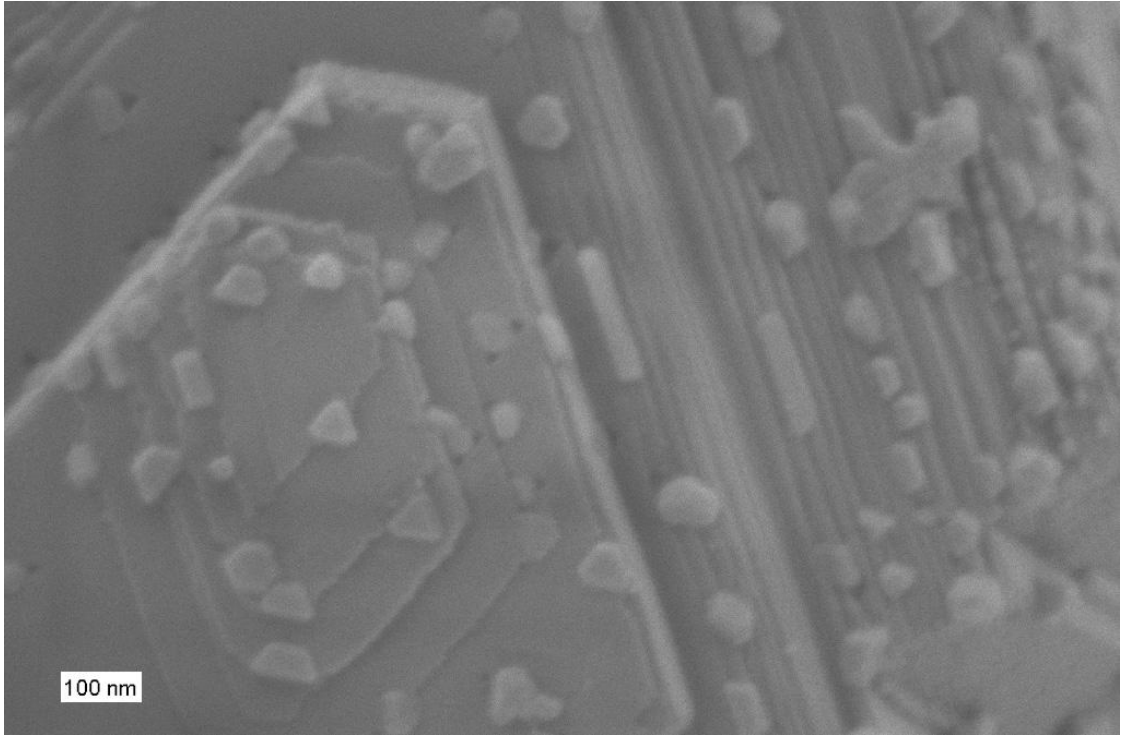


Figure 64. Low-voltage secondary electron image of  $\text{NiAl}_2\text{O}_4 + 2.5 \text{ wt\% ZrO}_2$ , reduced at  $750 \text{ }^\circ\text{C}$  in 300 Torr  $\text{H}_2$  for 29 hours. 0.45 kV, 200 kX original magnification.

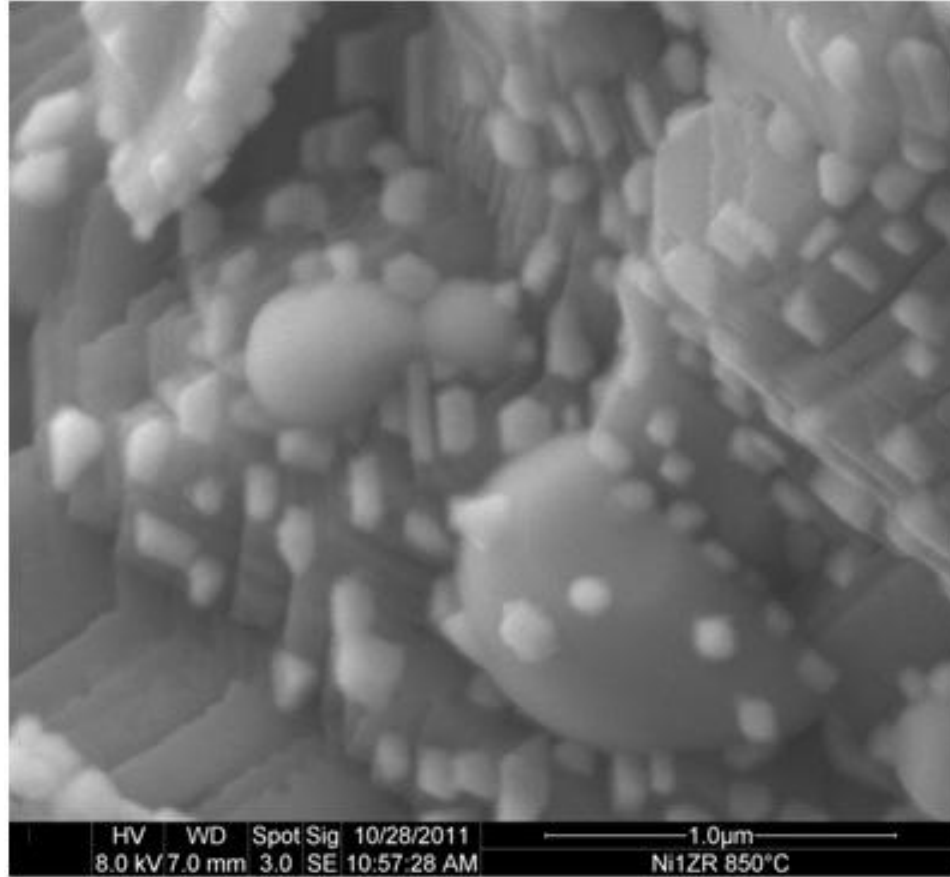


Figure 65. Secondary electron image of  $\text{NiAl}_2\text{O}_4 + 2.5 \text{ wt\% ZrO}_2$ , reduced at 850 °C in 300 Torr  $\text{H}_2$  for 24 hours. 50 kX original magnification.

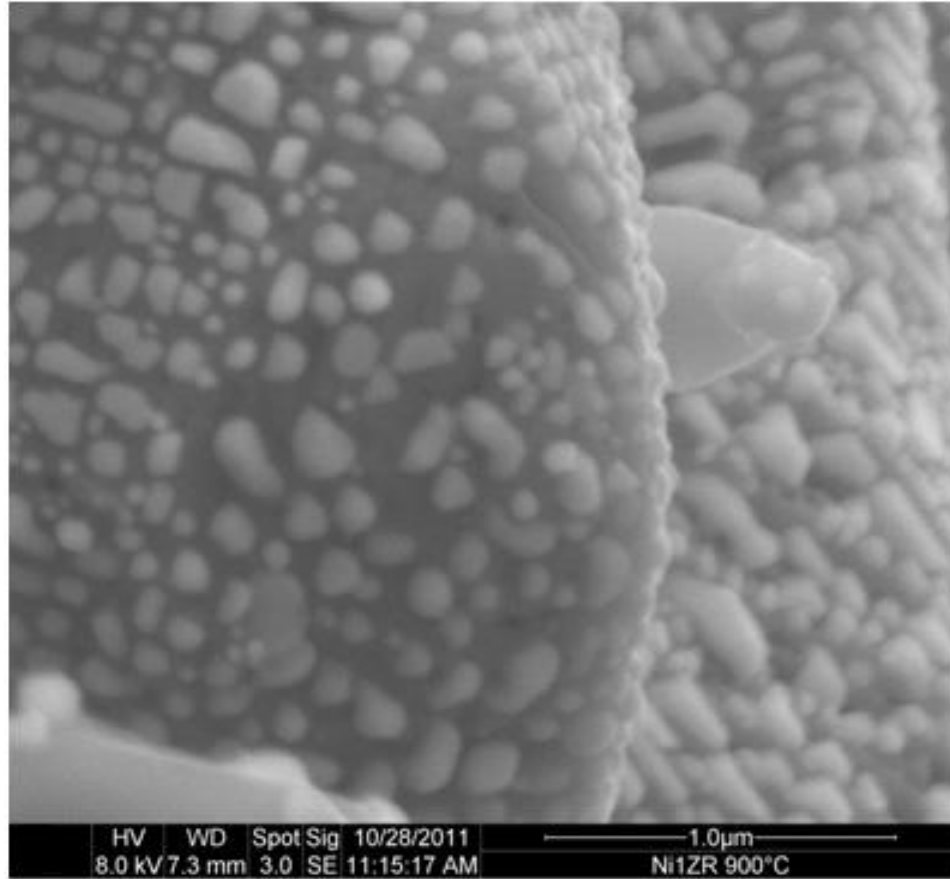


Figure 66. Secondary electron image of NiAl<sub>2</sub>O<sub>4</sub> + 2.5 wt% ZrO<sub>2</sub>, reduced at 900 °C in 300 Torr H<sub>2</sub> for 12 hours. 50 kX original magnification.

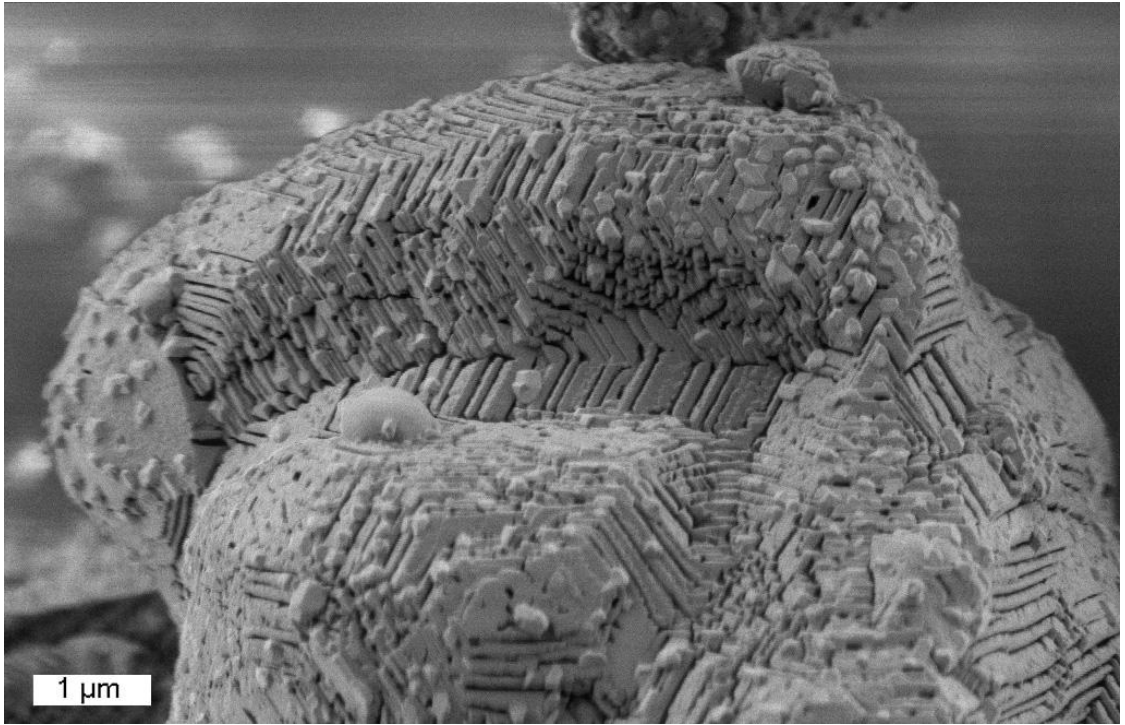


Figure 67. Low-voltage secondary electron image of  $\text{NiAl}_2\text{O}_4 + 2.5 \text{ wt}\% \text{ ZrO}_2$ , reduced at  $900 \text{ }^\circ\text{C}$  in 300 Torr  $\text{H}_2$  for 12 hours. 0.40 kV, 30 kX original magnification.

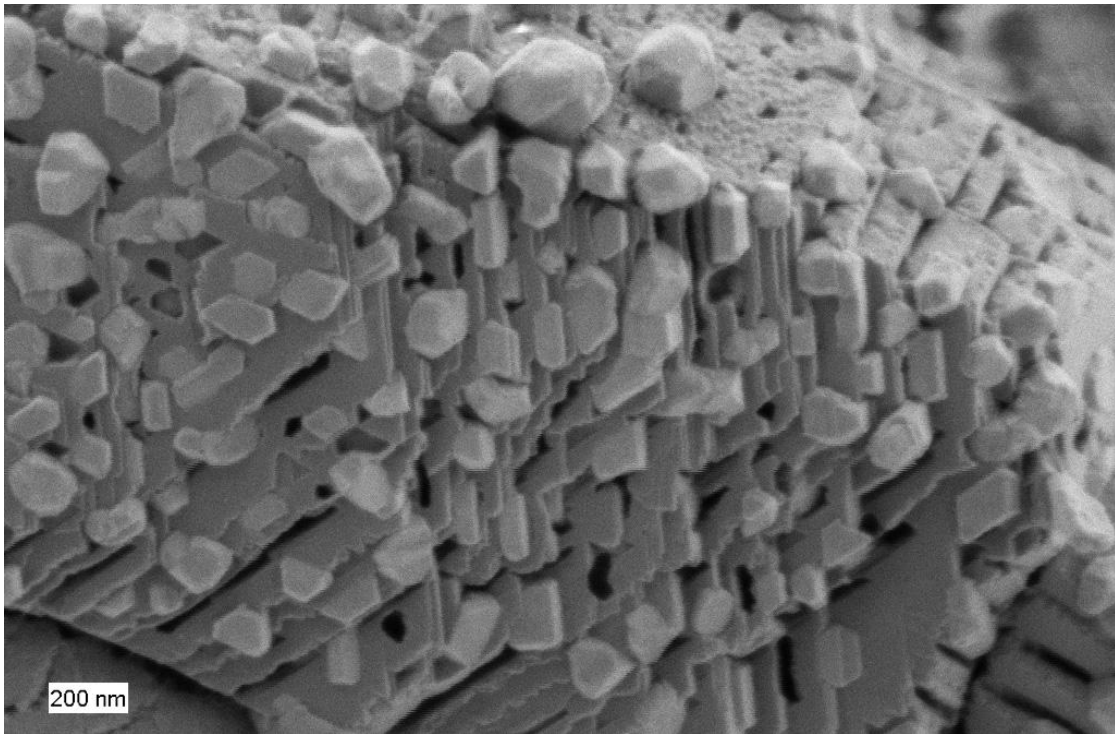


Figure 68. Low-voltage secondary electron image of  $\text{NiAl}_2\text{O}_4 + 2.5 \text{ wt\% ZrO}_2$ , reduced at  $900 \text{ }^\circ\text{C}$  in 300 Torr  $\text{H}_2$  for 12 hours. 0.40 kV, 100 kX original magnification.

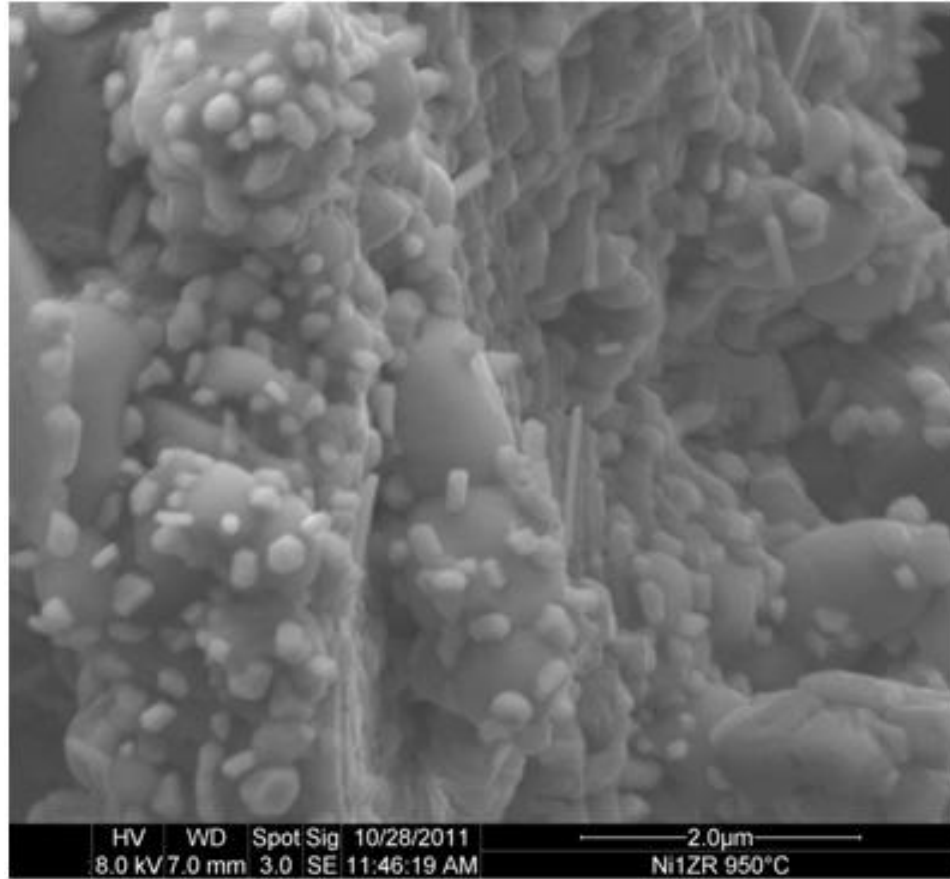


Figure 69. Secondary electron image of  $\text{NiAl}_2\text{O}_4 + 2.5 \text{ wt\% ZrO}_2$ , reduced at 950 °C in 300 Torr  $\text{H}_2$  for 12 hours. 20 kX original magnification.

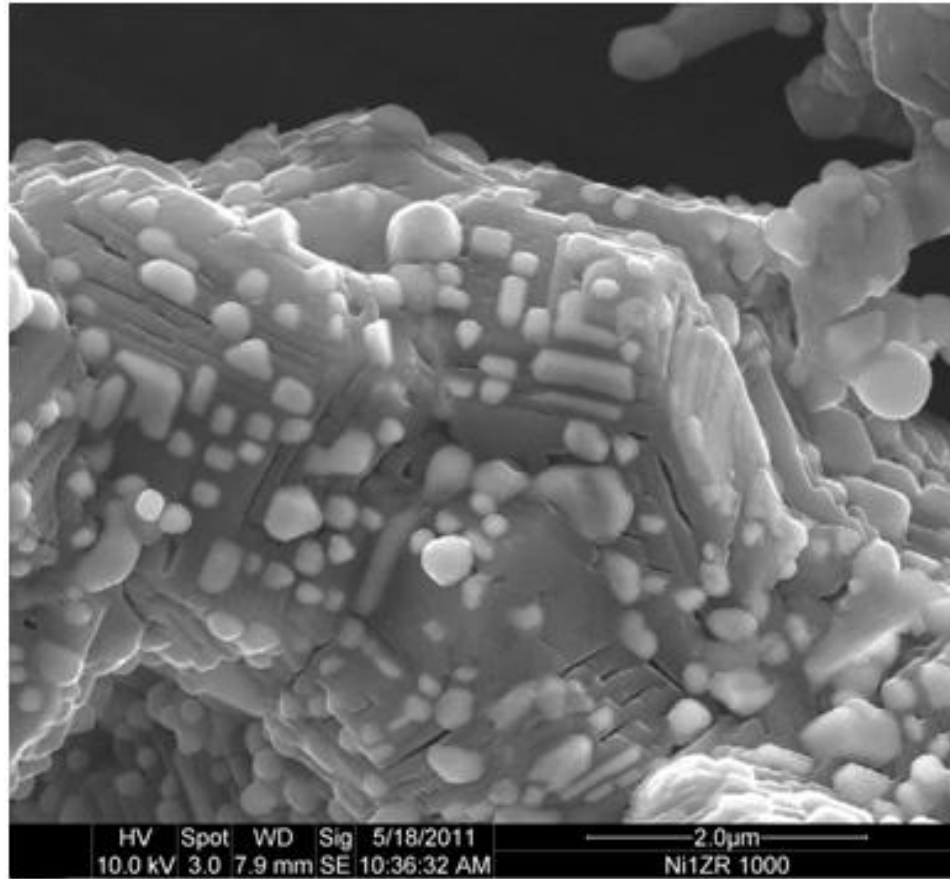


Figure 70. Secondary electron image of  $\text{NiAl}_2\text{O}_4 + 2.5 \text{ wt\% ZrO}_2$ , reduced at 1000 °C in 300 Torr  $\text{H}_2$  for 12 hours. 20 kX original magnification.

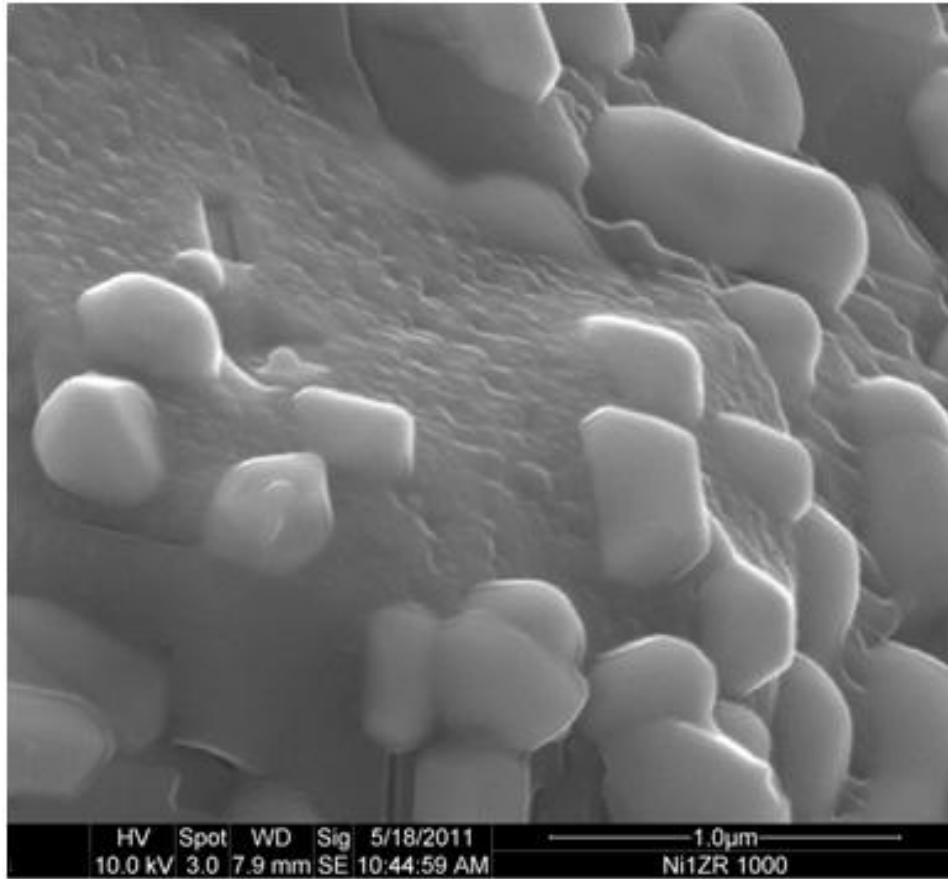


Figure 71. Secondary electron image of  $\text{NiAl}_2\text{O}_4 + 2.5 \text{ wt\% ZrO}_2$ , reduced at  $1000 \text{ }^\circ\text{C}$  in 300 Torr  $\text{H}_2$  for 12 hours. 50 kX original magnification.

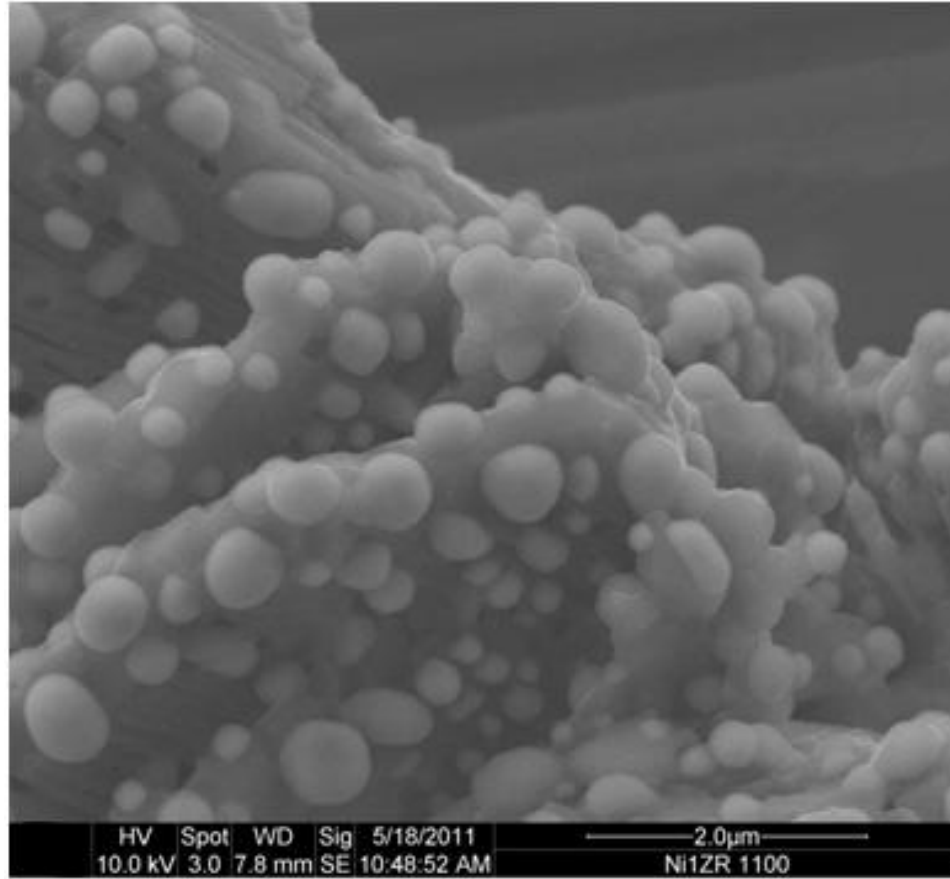


Figure 72. Secondary electron image of  $\text{NiAl}_2\text{O}_4 + 2.5 \text{ wt\% ZrO}_2$ , reduced at 1100 °C in 300 Torr  $\text{H}_2$  for 12 hours. 20 kX original magnification.

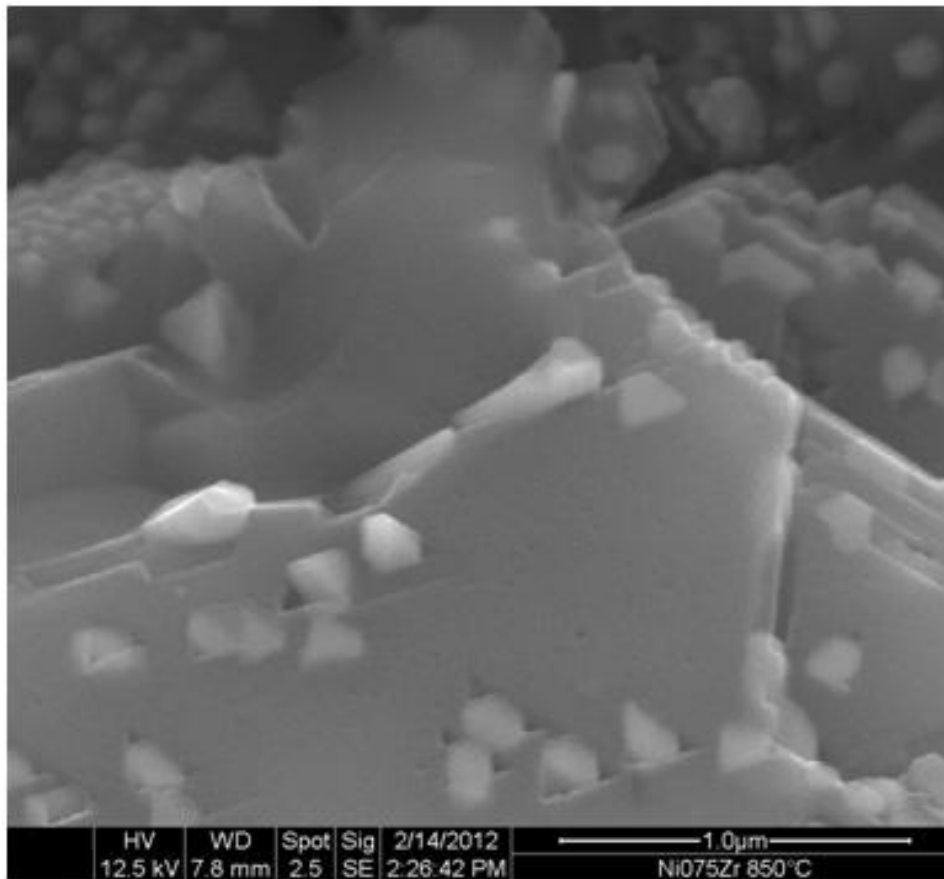


Figure 73. Secondary electron image of  $\text{Ni}_{0.75}\text{Mg}_{0.25}\text{Al}_2\text{O}_4 + 2.5 \text{ wt\% ZrO}_2$ , reduced at  $850 \text{ }^\circ\text{C}$  in 300 Torr  $\text{H}_2$  for 24 hours. 50 kX original magnification.

## L. Nickel Crystallite Size, Shape and Distribution

### 1. Nickel Particle Distribution

The relative distribution of nickel metal on the surface of the spinel, or inside the grains is important to many potential applications, such as catalysis. Ni metal crystallites are observed on both the spinel and the  $\text{ZrO}_2$  particles, as shown in Figure 74, which is not particularly surprising.  $\text{Y}_2\text{O}_3$  stabilized cubic  $\text{ZrO}_2$  has been shown to dissolve up to 2 mole percent Ni, so it is quite possible that the monoclinic and tetragonal  $\text{ZrO}_2$  phases present in these samples are also capable of dissolving some amount of Ni. The Ni metal crystallites on the surface of the  $\text{ZrO}_2$  particles upon reduction are likely reducing from the  $\text{ZrO}_2$ .

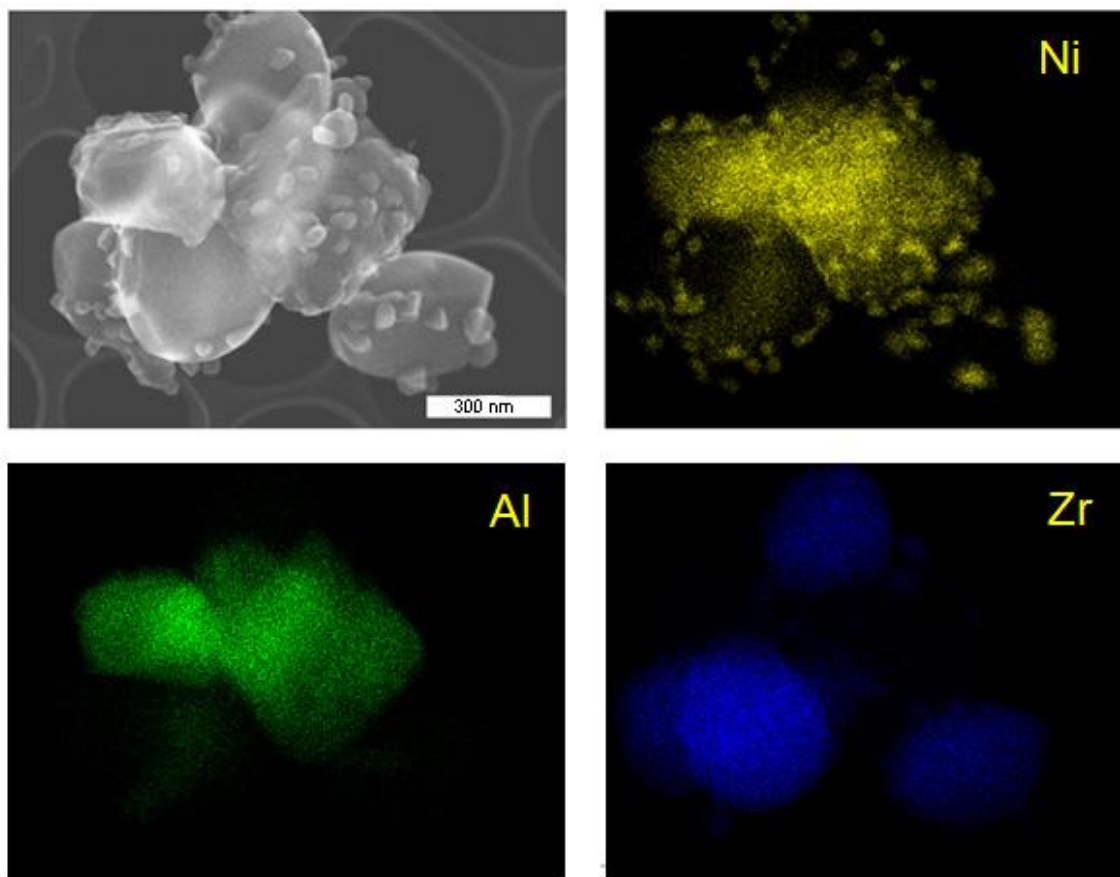


Figure 74. STEM EDS maps of an agglomerate of spinel and  $\text{ZrO}_2$  particles,  $\text{NiAl}_2\text{O}_4 + 2.5 \text{ wt}\% \text{ ZrO}_2$  reduced at  $850 \text{ }^\circ\text{C}$  for 24 hours in 300 Torr  $\text{H}_2$ . An abnormally high number of  $\text{ZrO}_2$  particles happen to be in this agglomerate. Nickel metal crystallites can be seen on both  $\text{ZrO}_2$  and spinel grains.

Quenard et al.<sup>55</sup> performed work on  $\text{Co}_x\text{Mg}_{1-x}\text{Al}_2\text{O}_4$  and  $\text{Ni}_x\text{Mg}_{1-x}\text{Al}_2\text{O}_4$  at low Co and Ni stoichiometries such that the fully reduced oxide would contain 4 wt% Ni or Co. They performed TGA measurements in an oxidizing atmosphere on their reduced powders and noted discrete weight gains at  $\sim 340 \text{ }^\circ\text{C}$  and  $\sim 950 \text{ }^\circ\text{C}$ , which they attributed to the oxidation of metal particles on the surface and in the interior, respectively. They also performed measurements where the powders were boiled in 1 molar HCl prior to the measurement to remove any Co or Ni on the surface. These powders lacked the weight gain at  $\sim 340 \text{ }^\circ\text{C}$  seen in the unboiled samples. By analysis of the relative weight gains of the HCl-boiled and unboiled powders, they determined that  $\sim 66\%$  of the metal particles were in the interior of the particles. Their powders were reduced at  $700 - 1000 \text{ }^\circ\text{C}$  in dry

hydrogen for one hour, and the reduced powders had a surface area of  $1 \text{ m}^2/\text{g}$  as measured by nitrogen adsorption.

As can be seen from the FIB TEM specimens and the SEM powder cross section images, Figure 75 and Figures 77 through 81, the percentage of nickel in the grains of the samples produced in this work is certainly much lower than 66%, more likely  $\sim 5\%$ . The temperatures used by Quenard et al. were similar to those used in this study, though their treatment duration was much shorter. Quenard used only one nickel stoichiometry, sufficient to yield 4 wt% Ni in the fully reduced composite. The lowest nickel containing composition used in this study,  $\text{Ni}_{0.25}\text{Mg}_{0.75}\text{Al}_2\text{O}_4 + 2.5 \text{ wt\% ZrO}_2$ , yields 9.73 wt% nickel upon full reduction. Quenard's powders had an unusually small particle size, at a surface area of  $16 \text{ m}^2/\text{g}$ , whereas the surface area of the solid state synthesis derived powder in this work is likely  $\sim 0.5 - 1 \text{ m}^2/\text{g}$  given the high  $1500 \text{ }^\circ\text{C}$  calcination temperature used. Any of the factors of stoichiometry, particle size, or the presence of  $\text{ZrO}_2$  could be the cause of the differences in observed behavior.

The high concentration of nickel metal crystallites on the surface is supported by gas adsorption data. When measured by  $\text{N}_2$ ,  $\text{Ni}_{0.75}\text{Mg}_{0.25}\text{Al}_2\text{O}_4 + 2.5 \text{ wt\% ZrO}_2$  reduced at  $900 \text{ }^\circ\text{C}$  for 12 hours in 300 Torr  $\text{H}_2$  showed a surface area of  $1.19 \text{ m}^2/\text{g}$ , as calculated by the BET method. When measured by  $\text{H}_2$  adsorption, which would be specific to the Ni metal surfaces, the sample showed a surface area of  $0.37 \text{ m}^2/\text{g}$ , showing that 31% of the sample surface area is due to the nickel metal.

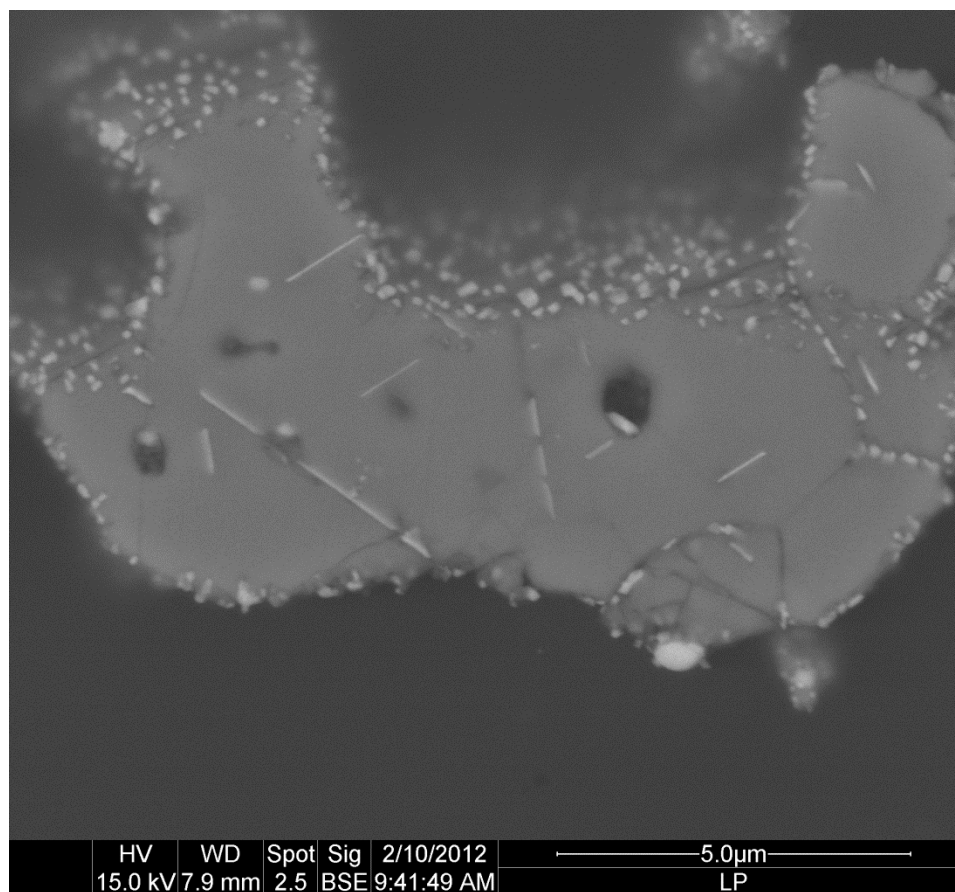


Figure 75. Back scatter SEM image of a cross section of  $\text{NiAl}_2\text{O}_4 + 2.5 \text{ wt\% ZrO}_2$  reduced at  $900 \text{ }^\circ\text{C}$  for 12 hours in 300 Torr  $\text{H}_2$ . The high concentration of nickel metal crystallites on the surface of the particle can be viewed through the epoxy.

## 2. Refined and Observed Nickel Crystallite Sizes, and Crystallite Shape

Figure 76 shows a comparison between the nickel metal crystallite sizes, as determined by Rietveld refinement, and as measured from SEM images. The very good agreement between the two strongly suggests that the nickel metal crystallites are monocrystals. If the nickel metal crystallites were twinned or made up of multiple grains, the refined crystallite sizes would be a fraction of the observed sizes. The data is tabulated in Table VII, including the range of sizes observed in the SEM.

As is best shown in Figure 64, the (111) faces of the nickel and spinel appear to be coplanar, as suggested by the triangle on triangle morphology.

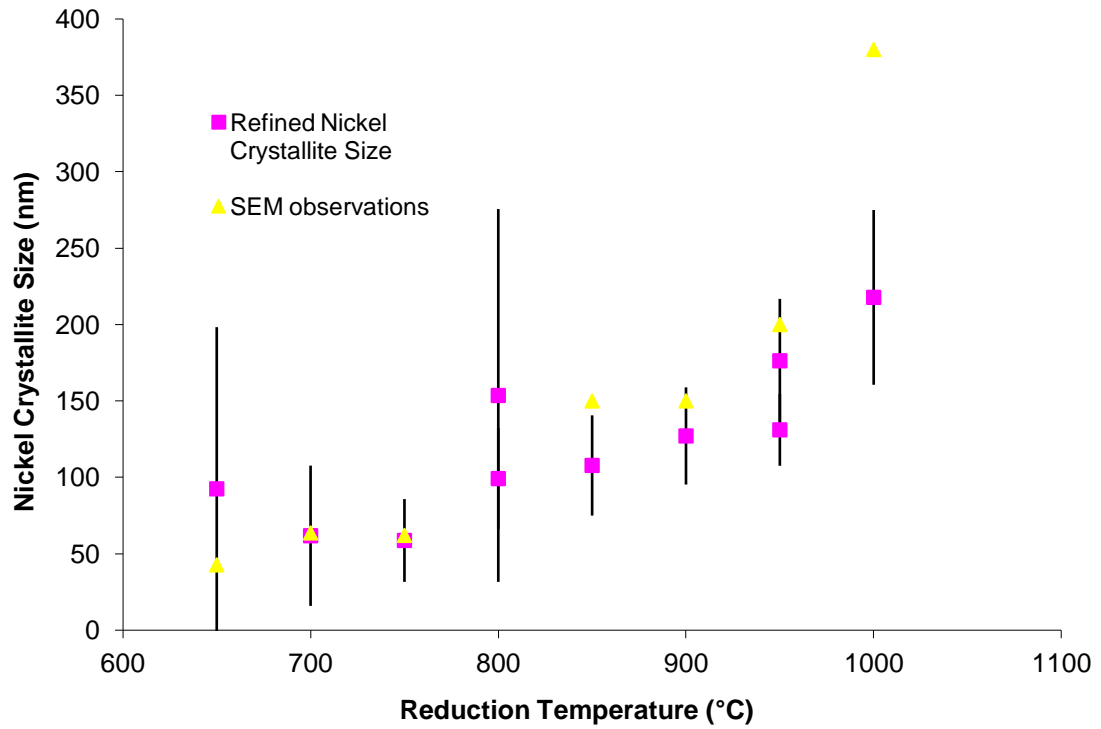


Figure 76. Comparison of refined nickel crystallite sizes to those observed in the SEM for  $\text{NiAl}_2\text{O}_4 + 2.5 \text{ wt\% ZrO}_2$ . Error bars show one standard deviation in the refined values. Error bars are not shown for the measurements from SEM images, but ranges are given in Table VII. SEM of the 800 °C reduced sample is not included as it was sent for neutron diffraction. The 1100 °C sample is not included as it is difficult to distinguish the  $\text{ZrO}_2$  crystallites from the Ni crystallites in that sample.

Table VII. Comparison of Observed and Refined Nickel Crystallite Sizes

Reduction Temperature (°C)	Refined Crystallite Size (nm)	Refined Error (nm)	Observed Size (nm)	Observed Range (nm)
650	92.5	105.8	43	20-60
700	61.8	45.9	64	50-70
750	58.7	27.1	62	45-70
800	153.6	122.0	†	†
800 #2	99.2	33.1	†	†
850	107.8	32.8	150	100-260
900	127.1	31.8	150	100-250
950	176.3	40.5	200	140-300
950 #2	131.1	23.5	*	*
1000	217.8	57.2	380	200-840
1100	1615.8	2176.7	Ψ	Ψ

† - Sent for neutron diffraction before SEM could be performed.

\* - Only one 950 °C sample was analyzed by SEM

Ψ - ZrO<sub>2</sub> and Ni particles could not be distinguished from one another.

### 3. Needle-Like Particles in the Interior of Grains

Needle-like metallic nickel crystallites (likely plate-like in three dimensions) are observed in both the SEM images of the polished powder cross sections and the FIB'ed TEM specimens, Figure 75, Figure 77, and Figures 79 through 81. These particle shapes are most likely the result of short circuit diffusion.<sup>36</sup> Reduction temperatures used in this study are given in Table VIII as a fraction of the 2110 °C homologous melting temperature of NiAl<sub>2</sub>O<sub>4</sub>.

Table VIII. Reduction Temperatures as a Fraction of the Homologous Melting Temperature of NiAl<sub>2</sub>O<sub>4</sub>.

Reduction Temperature (°C)	650	700	750	800	850	900	950	1000	1100
Fraction of Homologous Melting Temperature of NiAl <sub>2</sub> O <sub>4</sub>	0.39	0.41	0.43	0.45	0.47	0.49	0.51	0.53	0.58

The samples examined in the TEM investigation which were cut with a focused ion beam were  $\text{NiAl}_2\text{O}_4 + 2.5 \text{ wt\% ZrO}_2$  reduced at 850 °C for 24 hours, and 900, and 950 °C for 12 hours. Needle like nickel crystallites were observed in the FIB slices of the 850 and 950 °C reduced samples, Figures 77 and 79, but not in the 900 °C reduced sample, Figure 78, which was mostly a near surface region.

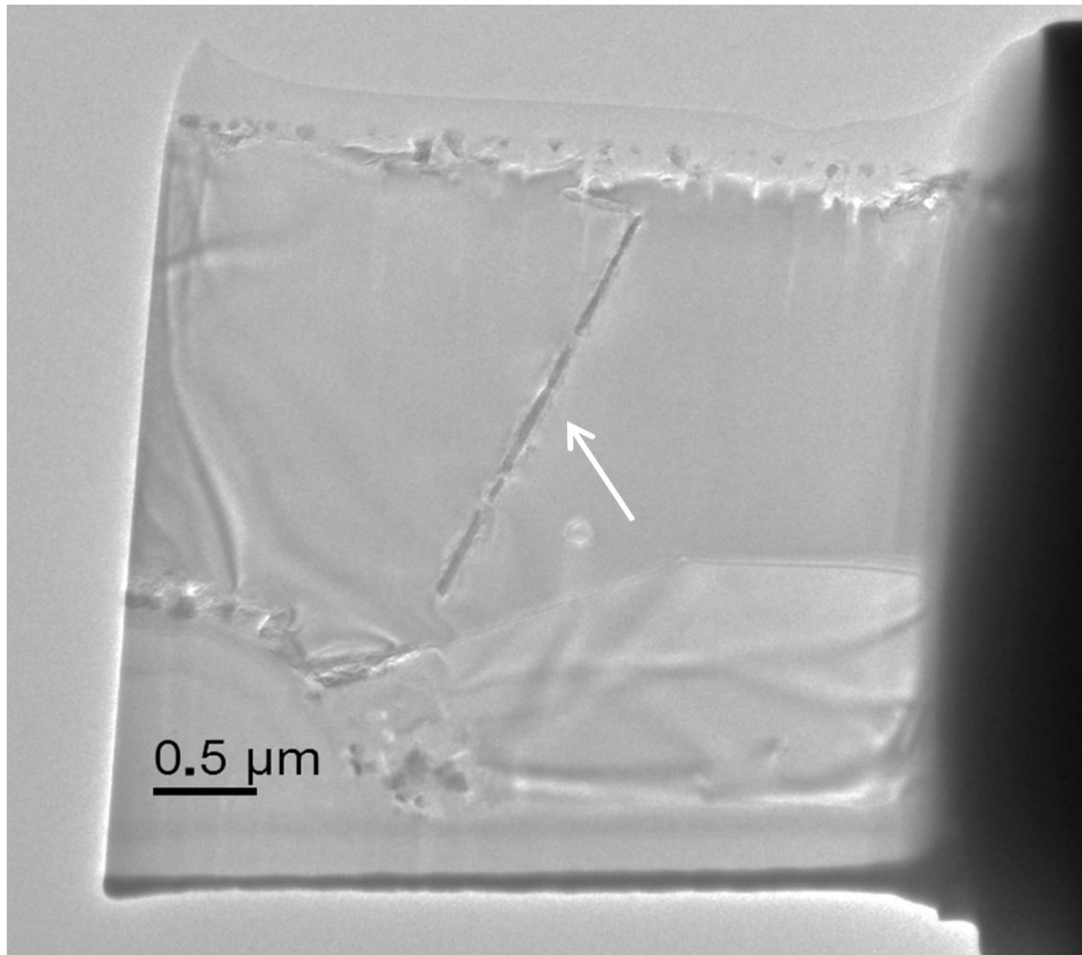


Figure 77. TEM image of a specimen cut from  $\text{NiAl}_2\text{O}_4 + 2.5 \text{ wt\% ZrO}_2$  reduced at 850 °C for 24 hours in 300 Torr  $\text{H}_2$  with a FIB. A needle-like nickel crystallite is visible at the center of the specimen.

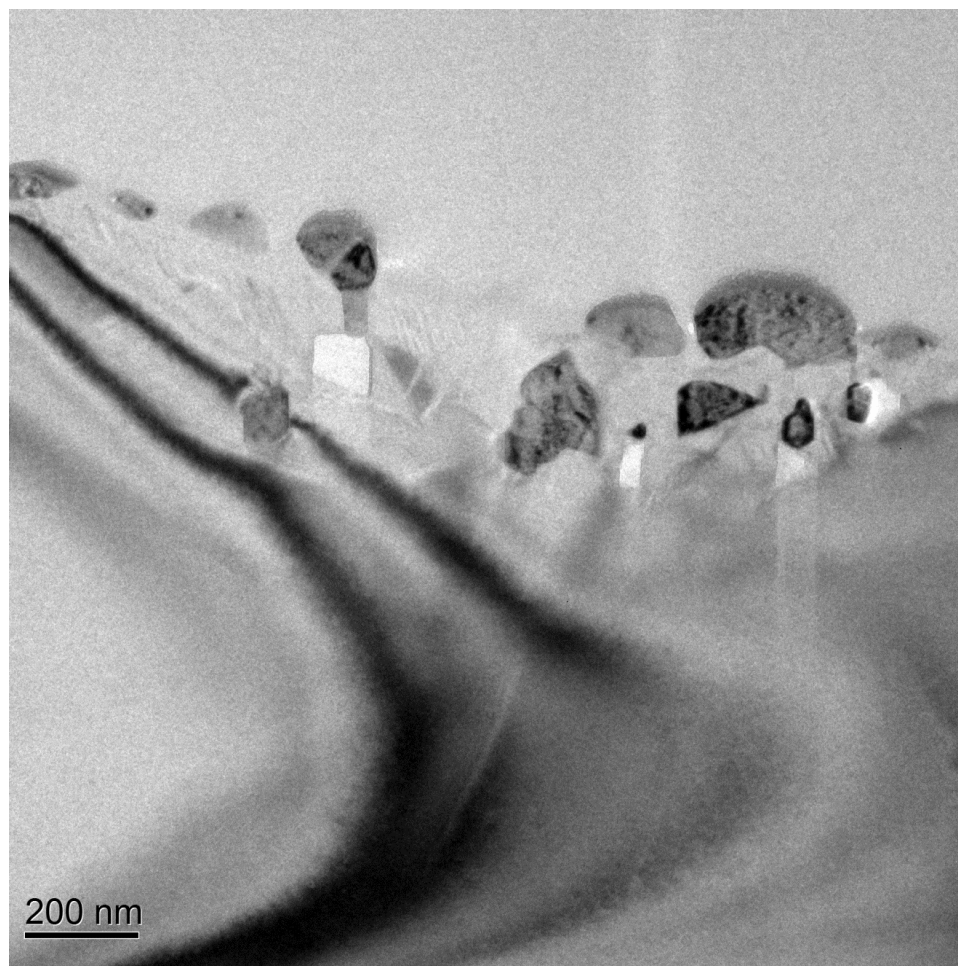


Figure 78. TEM image of a specimen cut from NiAl<sub>2</sub>O<sub>4</sub> + 2.5 wt% ZrO<sub>2</sub> reduced at 900 °C for 12 hours in 300 Torr H<sub>2</sub> with a FIB. No needle-like nickel crystallites are visible in the specimen.

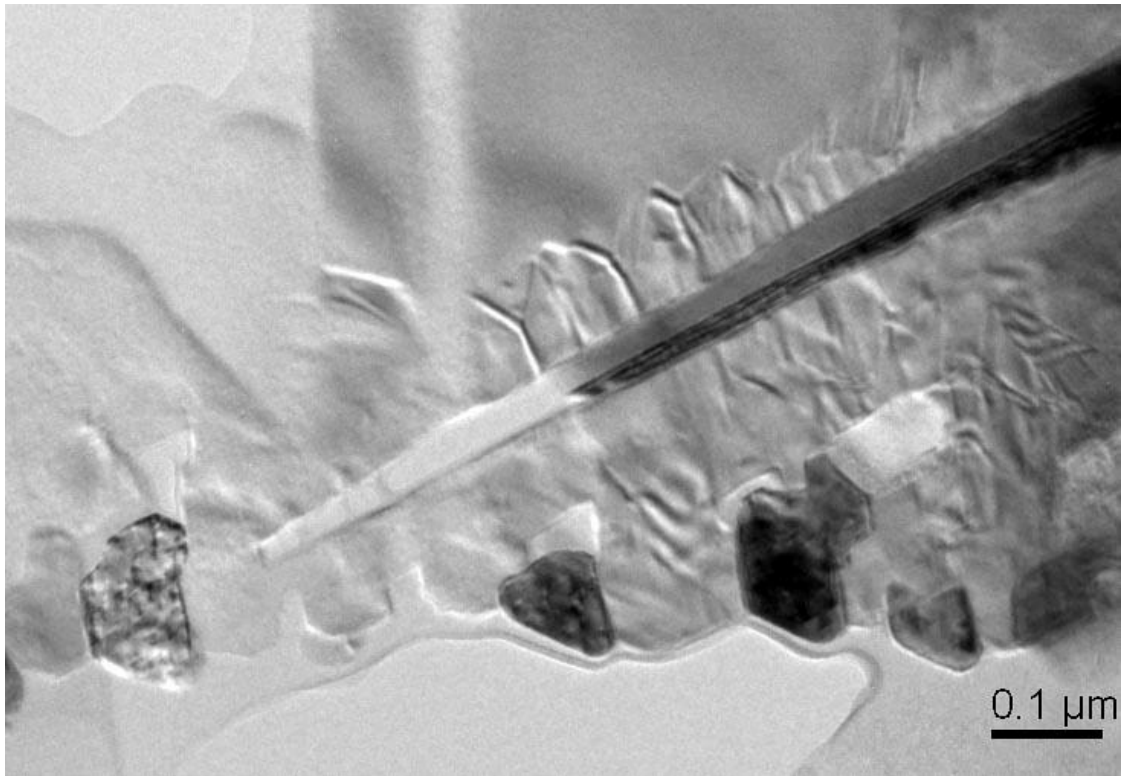


Figure 79. TEM image of a specimen cut from  $\text{NiAl}_2\text{O}_4 + 2.5 \text{ wt\% ZrO}_2$  reduced at  $950 \text{ }^\circ\text{C}$  for 12 hours in 300 Torr  $\text{H}_2$  with a FIB. A needle-like nickel crystallite is visible at the center of the sample. The light vertical streak is an artifact from the FIB process. The tip of the crystallite has fallen out of the specimen.

Powder cross-sections were made from the  $\text{NiAl}_2\text{O}_4 + 2.5 \text{ wt\% ZrO}_2$  samples reduced at 900 and  $950 \text{ }^\circ\text{C}$ . These powder cross sections were examined in the SEM, as shown in Figures 80 and 81, and both samples contained numerous needle-like nickel particles.

All samples examined were reduced at a temperature near or below half of the homologous melting temperature of  $\text{NiAl}_2\text{O}_4$ , with  $950 \text{ }^\circ\text{C}$  being 0.51 of the  $2110 \text{ }^\circ\text{C}$  homologous melting temperature of  $\text{NiAl}_2\text{O}_4$ . Observation of needle-like nickel metal crystallites in all observed specimens agrees with the rule of thumb proposed by Rogers and Trumble.<sup>36</sup> The intragrain inhomogeneous crystallites seen in Figure 81 are parallel to one another. This was seen in many particles in the cross sections of the reduced powders. The parallel nature of the crystallites strongly suggests a crystalline orientation relationship with the spinel matrix.

Üstündag et al.<sup>31</sup> reduced monolithic  $\text{NiAl}_2\text{O}_4$  samples without  $\text{ZrO}_2$ , and with various  $\text{ZrO}_2$  loadings, at 1100, 1300, and 1350 °C. In both  $\text{ZrO}_2$  containing and  $\text{ZrO}_2$  free samples, needle-like particles were observed at 1100 °C, but none at 1300 or 1350 °C. This agrees with the principles set forth by Trumble and Ross, although at 0.58 of the homologous melting temperature, 1100 °C is a bit high. However, monolithic samples were used, which would likely increase the transition temperature of the behavior, as monolithic samples increase the diffusion distance to the surface.

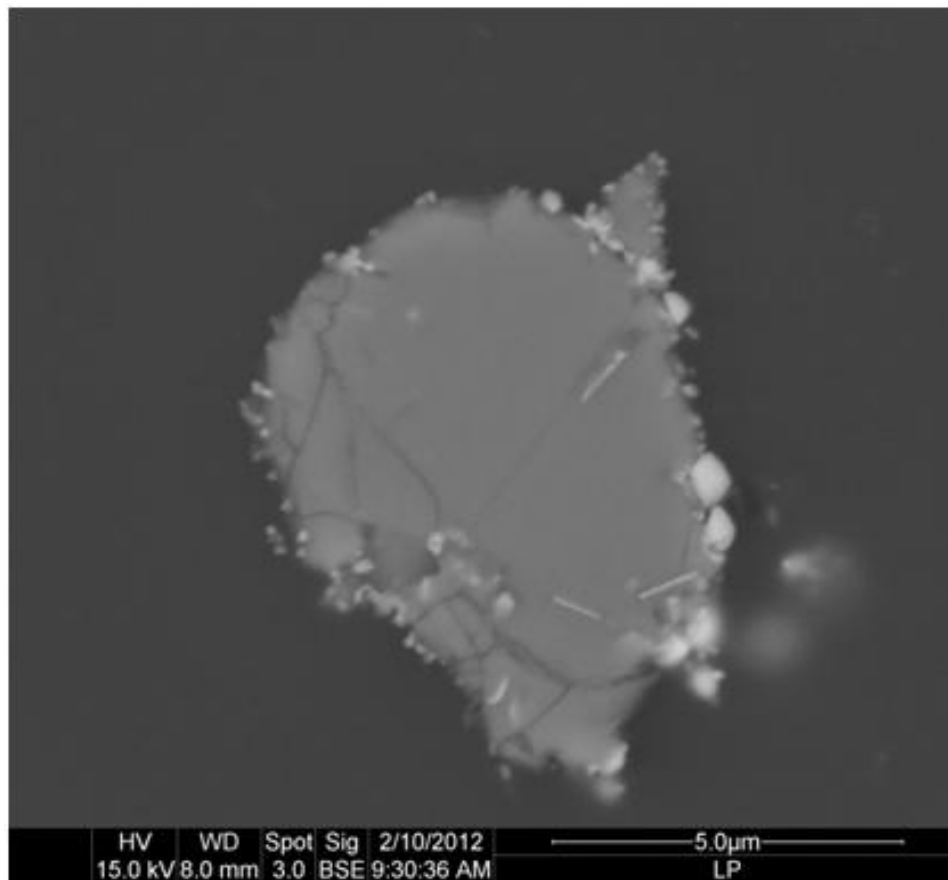


Figure 80. Back scatter SEM image of a cross section of  $\text{NiAl}_2\text{O}_4 + 2.5 \text{ wt\% ZrO}_2$  reduced at 900 °C for 12 hours in 300 Torr  $\text{H}_2$ . Many needle-like nickel crystallites are visible in the sample.

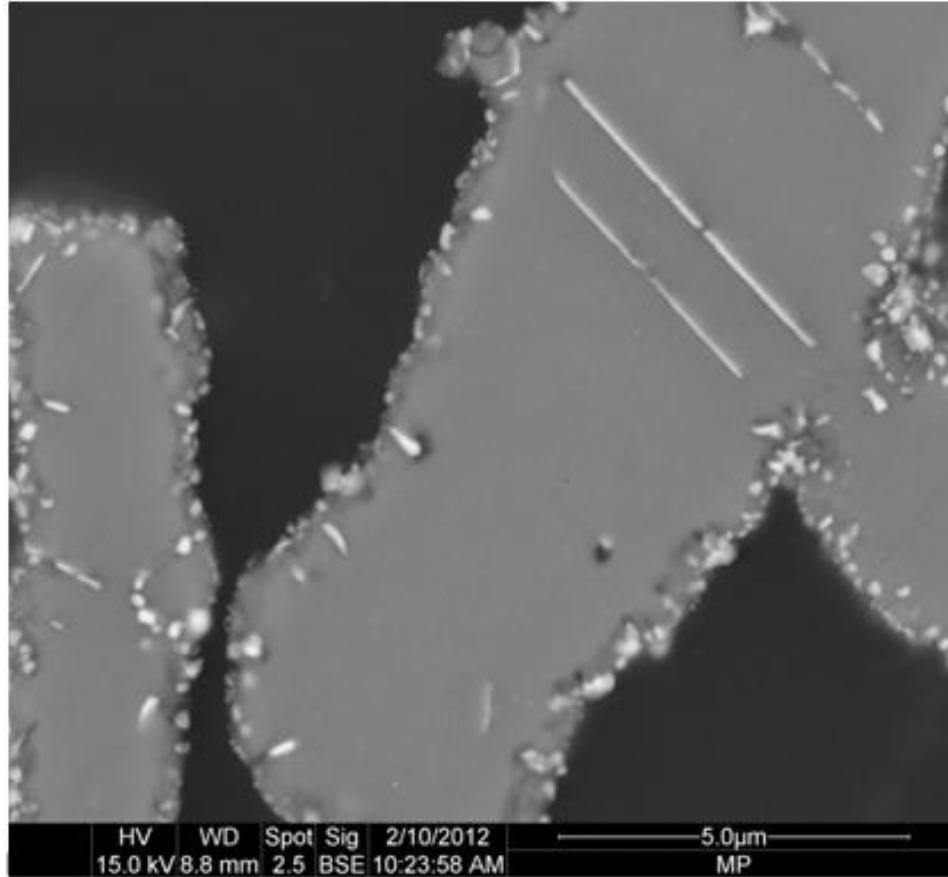


Figure 81. Back scatter SEM image of a cross section of  $\text{NiAl}_2\text{O}_4 + 2.5 \text{ wt\% ZrO}_2$  reduced at  $950 \text{ }^\circ\text{C}$  for 12 hours in 300 Torr  $\text{H}_2$ . Needle-like nickel crystallites are visible in the sample.

### M. Suggestions for Assessing Extent of Reduction

The long durations necessary to completely reduce the spinels shows the importance of accurately assessing and reporting the extent of reduction in any study examining the catalytic properties, microstructure, or crystal structure of any reducible spinel. Controlling factors for the extent of reduction of a given composition include the treatment time,  $\text{PO}_2$ , and temperature. For reductions in a closed system, the system volume and sample mass also contribute, as the  $\text{PO}_2$  in the atmosphere will increase as the reduction proceeds. At a given reducible sample mass, a larger system volume would experience a smaller rise in  $\text{PO}_2$  than would a system of a smaller volume.

While performing the reduction in the TGA and using that sample for subsequent analyses works well for some techniques, this method is not feasible with the amount of sample necessary for some experiments, particularly catalysis testing, chemisorptions measurements, and surface area analysis. If a TGA is used to produce samples at degrees of reduction less than complete, the mass signal must be monitored during cooling, as reduction will continue to occur if the reducing atmosphere is not removed from the sample.

Simply weighing the mass of powder before and after reduction to obtain a mass loss is a poor choice because powder can sometimes be lost from the crucibles during loading, pumping down, and unloading, although a porous crucible lid could possibly avoid those problems. Reducing an easily weighted solid pellet and crushing it afterward is also problematic. The resulting powder would not be homogeneously reduced unless the reduction were complete, since the reduction proceeds from the outer surface inward. Also, the SEM images of reduced powder and cross-sectioned reduced powder, Figures 63 to 81, show very high metal concentrations on the powder surfaces, a catalytically important feature that would be lost by reducing a pellet and subsequently crushing it.

The recommended procedure is to use TGA experiments to identify a reaction time, temperature, and atmosphere capable of fully reducing the desired composition at the synthesized particle size distribution. Reductions can then be performed either in a closed or flowing gas system at the desired reaction parameters. Representative samples of the same mass previously run in the TGA can then be taken from the reduced powder and reduced in the TGA, using the reaction parameters previously found able to completely reduce the parent powder. By comparing the weight loss of the unreduced powder to the weight loss of the powder reduced in the closed system, the extent of reaction can be accurately assessed, and reduction methods more amenable to large volumes can be used. Conversely, a weight gain upon oxidation of a reduced powder could also be used to assess the extent of reduction.

## SUMMARY AND CONCLUSIONS

The reduction of  $\text{Ni}_x\text{Mg}_{1-x}\text{Al}_2\text{O}_4 + 2.5 \text{ wt\% ZrO}_2$  in  $\text{H}_2$  was characterized by room temperature X-ray diffraction, high temperature X-ray diffraction, thermogravimetric analysis, pycnometry, TEM, and SEM. Upon full reduction, all samples lost a percentage of their mass corresponding to one  $\text{O}^{2-}$  for every  $\text{Ni}^{2+}$  in the starting composition.  $\text{Ni}_{0.25}\text{Mg}_{0.75}\text{Al}_2\text{O}_4 + 2.5 \text{ wt\% ZrO}_2$  and  $\text{Ni}_{0.5}\text{Mg}_{0.5}\text{Al}_2\text{O}_4 + 2.5 \text{ wt\% ZrO}_2$  were shown to form Ni metal and a non-stoichiometric spinel of the same Mg-Al ratio as the starting composition.

The spinel phases of  $\text{NiAl}_2\text{O}_4 + 2.5 \text{ wt\% ZrO}_2$  and  $\text{Ni}_{0.75}\text{Mg}_{0.25}\text{Al}_2\text{O}_4 + 2.5 \text{ wt\% ZrO}_2$  were found to be unstable as full reduction was approached, and metastable spinel phases,  $\Theta\text{-Al}_2\text{O}_3$ , and  $\alpha\text{-Al}_2\text{O}_3$  formed sequentially given enough time at temperature. From the data a phase diagram was constructed in a previously uninvestigated region of the  $\text{NiAl}_2\text{O}_4 - \text{MgAl}_2\text{O}_4\text{-Al}_2\text{O}_3$  ternary phase diagram, using the phase stability of the remnant spinel as an indication of the edge of the spinel stability phase field, shown in Figure 59. The constructed phase diagram shows excellent agreement with the pseudobinary diagrams where a comparison is possible.

The formation of a non-stoichiometric spinel upon reduction was confirmed by density measurements of the reduced specimens using helium pycnometry. Very good agreement with the model was seen for the samples produced in the closed system reduction.

The onset of reduction temperature was shown to vary with composition in flowing 4%  $\text{H}_2/\text{Ar}$ , with  $\text{NiAl}_2\text{O}_4$  beginning to reduce at  $\sim 780 \text{ }^\circ\text{C}$ . The onset of reduction temperatures of the other compositions were much closer to each other than to that of  $\text{NiAl}_2\text{O}_4$ , but were consistently different from one another, beginning at  $\sim 900 \text{ }^\circ\text{C}$  for  $\text{Ni}_{0.75}\text{Mg}_{0.25}\text{Al}_2\text{O}_4$ . The reduction kinetics of  $\text{Ni}_{0.75}\text{Mg}_{0.25}\text{Al}_2\text{O}_4$  were the fastest on a mass percent loss basis at  $1000 \text{ }^\circ\text{C}$ , which explains results seen in the closed system reductions where at several temperatures, the  $\text{Ni}_{0.75}\text{Mg}_{0.25}\text{Al}_2\text{O}_4$  samples contain more nickel metal than do the reduced  $\text{NiAl}_2\text{O}_4$  samples. The kinetics of  $\text{NiAl}_2\text{O}_4$  and  $\text{Ni}_{0.5}\text{Mg}_{0.5}\text{Al}_2\text{O}_4$  were very similar, with  $\text{Ni}_{0.25}\text{Mg}_{0.75}\text{Al}_2\text{O}_4$  being the slowest, shown in Figures 41 and 42.

The lattice parameter of the spinel decreases as nickel is reduced from all compositions, and microstrain in the spinel increases. A distorted nickel metal peak shape was observed in the X-ray diffraction patterns for all compositions. The magnitude of the distortion increased with temperature for all compositions, except in  $\text{Ni}_{0.25}\text{Mg}_{0.75}\text{Al}_2\text{O}_4$ , in which it decreased with increasing temperature. The cause of this peak shape distortion is likely a mismatch of coefficient of thermal expansion between the nickel and the remnant spinel, but exact determination of the root cause of the distortion is difficult given the dynamics of the system. The presence of a small amount of Ni-Al alloy is also a possible cause of the distortion.

Comparison of the refined nickel metal crystallite size and the particle diameters observed in the SEM indicate that the crystallites are likely predominantly monocrystals. A very high portion of the nickel metal crystallites are on the spinel surfaces, comprising 31% of the sample surface area in one sample measured by both  $\text{N}_2$  and  $\text{H}_2$  adsorption.

Significant progress was made towards understanding the dynamics of a catalytically important system, including the reduced spinel stability limits, kinetics, and crystallite size dependencies. Subsequent studies can use the phase stability and kinetic results of this work to identify additives to stabilize the metastable spinel structures. Good candidates were identified in  $\text{ZrO}_2$  and  $\text{Nb}_2\text{O}_5$ . In addition  $\text{TiO}_2$  was found to promote the formation of corundum. This will be of aid in the development of a highly active fuel cell anode which can be regenerated after coking.

## FUTURE WORK

Now that the stability limit of the spinel has been defined, more detailed studies to investigate the effects of additives on the rate of decomposition of the metastable phases can be conducted. Spinel reduced to near their stability limit can be used for HTXRD experiments in flowing 4% H<sub>2</sub> at a temperature where the reduction kinetics are sufficiently slow to allow the phase changes to be monitored, ~ 900 to 950 °C. The rate of phase change through the metastable defect spinels to transition alumina to corundum could then be quantified in the undoped spinels and in the presence of different additives.

The possibility of the formation of a Ni-Al alloy could be explored by performing reductions in flowing pure H<sub>2</sub> to further investigate the root cause of the nickel metal peak shape distortion seen in XRD. Flowing pure H<sub>2</sub> would maintain throughout the reduction the PO<sub>2</sub> which was seen by the furnace reduced samples at the start of the reduction. According to the phase diagram by Elfrefaie and Smeltzer,<sup>35</sup> if this PO<sub>2</sub> is in fact low enough to form a Ni-Al alloy, all metal reduced would be of this composition. This would result in an observable shift in the lattice parameter that could be easily quantified.

In the closed system reductions as currently configured, the moles of H<sub>2</sub> applied to the furnace vary with the reduction temperature employed when one pressure is applied for all temperatures used. A method to ensure that a constant number of moles of H<sub>2</sub> were applied to the system for every temperature would be to add a reservoir of a given volume to the gas manifold, and add a valve separating the gas manifold from the furnace. When the H<sub>2</sub> is applied, the valve to the furnace would be closed after it had been pumped down to vacuum, and a given pressure of H<sub>2</sub> would be added to the manifold. The valve to the furnace would then be opened. The pressure in the system would vary with reduction temperature employed, but the number of moles of H<sub>2</sub> would be consistent.

An additional means of characterizing the reduction of the system would be to use flowing hydrogen at a range of temperatures to achieve full reduction at each temperature. The dependence of nickel metal crystallite size could then be determined as

a function of temperature only, with the extent of reduction a constant. In the current work, reduction temperature and extent of reduction are correlated, preventing the determination of a true dependency on reduction temperature.

## REFERENCES

1. P. Porta, F.S. Stone, and R.G. Turner, "The distribution of nickel ions among octahedral and tetrahedral sites in  $\text{NiAl}_2\text{O}_4$ - $\text{MgAl}_2\text{O}_4$  solid solutions," *J. Solid State Chem.*, **11** [2] 135-47 (1974).
2. E. Ryshkewitch, *Oxide Ceramics*. pp. 257-274, Academic Press, New York, 1960.
3. Y.S. Han, J.B. Li, X.S. Ning, and B. Chi, "Temperature dependence of the cation distribution in nickel aluminate spinel from thermodynamics and X-rays," *J. Am. Ceram. Soc.*, **88** [12] 3455-7 (2005).
4. J.A. Azurdia, J. Marchal, P. Shea, H. Sun, X.Q. Pan, and R.M. Laine, "Liquid-feed flame spray pyrolysis as a method of producing mixed-metal oxide nanopowders of potential interest as catalytic materials. Nanopowders along the  $\text{NiO}$ - $\text{Al}_2\text{O}_3$  tie line including  $(\text{NiO})_{0.22}(\text{Al}_2\text{O}_3)_{0.78}$ , a new inverse spinel composition," *Chem. Mater.*, **18** [3] 731-9 (2006).
5. N. Sahli, C. Petit, A.C. Roger, A. Kiennemann, S. Libs, and M.M. Bettahar, "Ni catalysts from  $\text{NiAl}_2\text{O}_4$  spinel for  $\text{CO}_2$  reforming of methane," *Catal. Today*, **113** [3-4] 187-93 (2006).
6. D. Dhak and P. Pramanik, "Particle size comparison of soft-chemically prepared transition metal (Co, Ni, Cu, Zn) aluminate spinels," *J. Am. Ceram. Soc.*, **89** [3] 1014-21 (2006).
7. Y.S. Han, J.B. Li, X.S. Ning, X.Z. Yang, and B. Chi, "Study on NiO excess in preparing  $\text{NiAl}_2\text{O}_4$ ," *Materials Science and Engineering A*, **369** [1-2] 241-4 (2004).
8. K.E. Sickafus, J.M. Wills, and N.W. Grimes, "Structure of spinel," *J. Am. Ceram. Soc.*, **82** [12] 3279-92 (1999).
9. N.W. Grimes, "The spinels: versatile materials," *Physics in Technology*, **6** [1] 22 (1975).
10. H.S.C. O'Neill and A. Navrotsky, "Simple spinels: crystallographic parameters, cation radii, lattice energies, and cation distribution," *Am. Mineral.*, **68** 181-94 (1983).
11. J.A. Ball, M. Pirzada, R.W. Grimes, M.O. Zacate, D.W. Price, and B.P. Uberuaga, "Predicting lattice parameter as a function of cation disorder in  $\text{MgAl}_2\text{O}_4$  spinel," *J. Phys.: Condens. Matter*, **17** [48] 7621 (2005).
12. R.J. Hill, J.R. Craig, and G.V. Gibbs, "Systematics of the spinel structure type," *Physics and Chemistry of Minerals*, **4** 317-40 (1979).

13. K. Mocala and A. Navrotsky, "Structural and thermodynamic variation in nickel aluminate spinel," *J. Am. Ceram. Soc.*, **72** [5] 826-32 (1989).
14. J.A. Ball, S.T. Murphy, R.W. Grimes, D. Bacorisen, R. Smith, B.P. Uberuaga, and K.E. Sickafus, "Defect processes in MgAl<sub>2</sub>O<sub>4</sub> spinel," *Solid State Sciences*, **10** [6] 717-24 (2008).
15. R.K. Datta and R. Roy, "Equilibrium order-disorder in spinels," *J. Am. Ceram. Soc.*, **50** [11] 578-83 (1967).
16. H. Furuhashi, M. Inagaki, and S. Naka, "Determination of cation distribution in spinels by X-ray diffraction method," *J. Inorg. Nucl. Chem.*, **35** [8] 3009-14 (1973).
17. R.I. Sheldon, T. Hartmann, K.E. Sickafus, A. Ibarra, B.L. Scott, D.N. Argyriou, A.C. Larson, and R.B. Von Dreele, "Cation disorder and vacancy distribution in nonstoichiometric magnesium aluminate spinel, MgO·xAl<sub>2</sub>O<sub>3</sub>," *J. Am. Ceram. Soc.*, **82** [12] 3293-8 (1999).
18. Y. Okuyama, N. Kurita, and N. Fukatsu, "Defect structure of alumina-rich nonstoichiometric magnesium aluminate spinel," *Solid State Ionics*, **177** [1-2] 59-64 (2006).
19. D.M. Roy, R. Roy, and E.F. Osborn, "The system MgO-Al<sub>2</sub>O<sub>3</sub>-H<sub>2</sub>O and influence of carbonate and nitrate ions on the phase equilibria," *Am. J. Sci.*, **251** [5] 337-61 (1953).
20. A.D. Mazzoni, M.A. Sainz, A. Caballero, and E.F. Aglietti, "Formation and sintering of spinels (MgAl<sub>2</sub>O<sub>4</sub>) in reducing atmospheres," *Mater. Chem. Phys.*, **78** [1] 30-7 (2003).
21. M. Rotan, J. Tolchard, E. Rytter, M.-A. Einarsrud, and T. Grande, "On the solid solution of the spinel phase in the system NiO-Al<sub>2</sub>O<sub>3</sub>," *J. Solid State Chem.*, **182** [12] 3412-5 (2009).
22. K.P.R. Reddy and A.R. Cooper, "Oxygen diffusion in magnesium aluminate spinel," *J. Am. Ceram. Soc.*, **64** [6] 368-71 (1981).
23. R. Subramanian, E. Üstündag, S.L. Sass, and R. Dieckmann, "In-situ formation of metal-ceramic microstructures by partial reduction reactions," *Solid State Ionics*, **75** [0] 241-55 (1995).
24. E. Üstündag, J.C. Hanan, B. Clausen, M.A.M. Bourke, S.L. Sass, and T.J. Barbieri, "Investigation of the reduction of NiAl<sub>2</sub>O<sub>4</sub> - I: Neutron diffraction studies," pp. 549-56 in *22nd Annual Conference on Composites, Advanced*

*Ceramics, Materials, and Structures: A: Ceramic Engineering and Science Proceedings*. John Wiley & Sons, Inc., 2008.

25. B. Clausen, E. Üstündag, P. Rangaswamy, M.A.M. Bourke, S.L. Sass, and T.J. Barbieri, "Investigations of the reduction of  $\text{NiAl}_2\text{O}_4$  - II: X-ray diffraction studies," pp. 557-64 in *22nd Annual Conference on Composites, Advanced Ceramics, Materials, and Structures: A: Ceramic Engineering and Science Proceedings*. John Wiley & Sons, Inc., 2008.
26. B. Clausen, E. Üstündag, and M.A.M. Bourke, "Investigation of the Reduction of  $\text{NiAl}_2\text{O}_4$ ," *Adv. X-Ray Anal.*, **44** 32-7 (2001).
27. R. Kolhe, C.Y. Hui, E. Üstündag, and S.L. Sass, "Residual thermal stresses and calculation of the critical metal particle size for interfacial crack extension in metal-ceramic matrix composites," *Acta Mater.*, **44** [1] 279-87 (1996).
28. E. Üstündag, B. Clausen, and M.A.M. Bourke, "Neutron diffraction study of the reduction of  $\text{NiAl}_2\text{O}_4$ ," *Appl. Phys. Lett.*, **76** [6] 694-6 (2000).
29. E. Üstündag, R. Subramanian, R. Vaia, R. Dieckmann, and S.L. Sass, "In situ formation of metal-ceramic microstructures, including metal-ceramic composites, using reduction reactions," *Acta Metall. Mater.*, **41** [7] 2153-61 (1993).
30. E. Üstündag, R. Subramanian, R. Dieckmann, and S.L. Sass, "In situ formation of metal-ceramic microstructures in the Ni-Al-O system by partial reduction reactions," *Acta Metall. Mater.*, **43** [1] 383-9 (1995).
31. E. Üstündag, P. Ret, R. Subramanian, R. Dieckmann, and S.L. Sass, "In situ metal-ceramic microstructures by partial reduction reactions in the Ni-Al-O system and the role of  $\text{ZrO}_2$ ," *Materials Science and Engineering A*, **A195** [1-2] 39-50 (1995).
32. E. Üstündag, Z. Zhang, M.L. Stocker, P. Rangaswamy, M.A.M. Bourke, S. Subramanian, K.E. Sickafus, J.A. Roberts, and S.L. Sass, "Influence of residual stresses on the evolution of micro-structure during the partial reduction of  $\text{NiAl}_2\text{O}_4$ ," *Materials Science and Engineering: A*, **238** [1] 50-65 (1997).
33. T. Isobe, K. Daimon, K. Ito, T. Matsubara, Y. Hikichi, and T. Ota, "Preparation and properties of  $\text{Al}_2\text{O}_3/\text{Ni}$  composite from  $\text{NiAl}_2\text{O}_4$  spinel by in situ reaction sintering method," *Ceram. Int.*, **33** [7] 1211-5 (2007).
34. M. Miller, "Nanoporous glass-ceramics for gas separation"; Ph.D Thesis. Alfred University, Alfred, 2008.

35. F.A. Elrefaie and W.W. Smeltzer, "Thermodynamics of Nickel-Aluminum-Oxygen System Between 900 and 1400 K," *J. Electrochem. Soc.*, **128** [10] 2237-42 (1981).
36. K.A. Rogers and K.P. Trumble, "Effect of reduction temperature on internal reduction microstructures," *Scripta Materialia*, **39** [1] 103-8 (1998).
37. M.N. Rahaman, *Ceramic Processing and Sintering*, 2nd ed. pp. 85, Taylor and Francis Group, Boca Raton, FL, 2003.
38. E.E. Kiss, M.M. Lazi, and G.C. Boškovi, "Catalyst component interactions in nickel/alumina catalyst," *Acta Periodica Technologica*, **2007** [38] 61-8 (2007).
39. S. Rossignol and C. Kappenstein, "Effect of doping elements on the thermal stability of transition alumina," *International Journal of Inorganic Materials*, **3** [1] 51-8 (2001).
40. P. Bassoul and J.C. Gilles, "Structure and Microstructure of the Metastable B Phase ( $\text{NiAl}_{10}\text{O}_{16}$ ) II. An Electron Microscopic Investigation of the Microstructure," *J. Solid State Chem.*, **58** [3] 389-97 (1985).
41. P. Bassoul and J.C. Gilles, "Structure and microstructure of the metastable B phase ( $\text{NiAl}_{10}\text{O}_{16}$ ): I. Preparation and structural study by X-ray diffraction," *J. Solid State Chem.*, **58** [3] 383-8 (1985).
42. A.-M. Lejus, "Sur la formation a haute temperature de spineless non stoechiometriques et de phases derivees," *Revue internationale des hautes temperatures et des refractaires*, **1** 53-95 (1964).
43. F. Colin, "Des Phases Formees au Cours de la Reduction de Certains Oxydes Mixtes  $n\text{Al}_2\text{O}_3 - \text{MO}$ ," *Revue Internationale des Hautes Temperatures et des Refractaires*, **5** 167-85 (1968).
44. H. Jagodzinski, "Die Bestimmung einer bei der Entmischung  $\text{Al}_2\text{O}_3$ -übersättigter Mg-Al-Spinelle auftretenden Zwischenstruktur," *Zeitschrift für Kristallographie*, **109** [1-6] 388-409 (1957).
45. R.-S. Zhou and R.L. Snyder, "Structures and transformation mechanisms of the [eta], [gamma] and [theta] transition aluminas," *Acta Crystallographica Section B*, **47** [5] 617-30 (1991).
46. I. Levin and D. Brandon, "Metastable alumina polymorphs: Crystal structures and transition sequences," *Journal of the American Ceramic Society*, **81** [8] 1995-2012 (1998).

47. C. Wolverton and K.C. Hass, "Phase stability and structure of spinel-based transition aluminas," *Physical Review B*, **63** [2] 024102 (2000).
48. S.-H. Cai, S.N. Rashkeev, S.T. Pantelides, and K. Sohlberg, "Phase transformation mechanism between  $\gamma$ - and  $\theta$ -alumina," *Physical Review B*, **67** [22] 224104 (2003).
49. H. Meltzman, D. Chatain, D. Avizemer, T.M. Besmann, and W.D. Kaplan, "The equilibrium crystal shape of nickel," *Acta Mater.*, **59** [9] 3473-83 (2011).
50. S.T. Misture, "Large-Volume Atmosphere-Controlled High Temperature X-Ray Diffraction Furnace," *Meas. Sci. Technol.*, **14** [7] 1091-8 (2003).
51. Bruker, *Topas Technical Reference*. pp. 37, Bruker AXS, Karlsruhe, Germany, 2009.
52. K.K. Chawla, *Composite Materials: Science and Engineering*, 2nd ed. pp. 303-305, Springer Science and Business Media, New York, 1998.
53. A.E. McHale and R.S. Roth, *Phase Diagrams for Ceramists, Volume 12*. pp. 86, The American Ceramic Society, Columbus, Ohio, 1996.
54. E.M. Levin and L.P. Cook, *Phase Diagrams for Ceramists: 1969 Supplement*. pp. 90, American Ceramic Society, Columbus, Ohio, 1969.
55. O. Quénard, C. Laurent, M. Brieu, and A. Rousset, "Synthesis, microstructure and oxidation of Co-MgAl<sub>2</sub>O<sub>4</sub> and Ni-MgAl<sub>2</sub>O<sub>4</sub> nanocomposite powders," *Nanostructured Materials*, **7** [5] 497-507 (1996).

## APPENDIX 1 – REFINED STRUCTURAL PARAMETERS

### Spinel

x	Reduction Temperature (°C)	Crystallite Size (nm)	Microstrain	Refined Weight %	a (Å)	Oxygen Positional Parameter
1	-	442(9)	0.044(1)	97.7(4)	8.04766(1)	0.25688(8)
1	650	277(5)	0.020(1)	97.83(7)	8.04636(2)	0.25685(9)
1	700	389(6)	0.0229(9)	97.7(6)	8.04614(1)	0.25701(8)
1	750	378(6)	0.0309(9)	97.3(6)	8.04610(2)	0.25681(7)
1	800	385(8)	0.061(1)	96.23(7)	8.04529(2)	0.25597(8)
1	800	480(16)	0.089(2)	95.27(8)	8.04483(3)	0.25546(1)
1	850	945(79)	0.137(2)	93.8(1)	8.04326(4)	0.2556(1)
1	900	1400(230)	0.182(3)	91.5(1)	8.04029(5)	0.2551(1)
1	950	2000(620)	0.217(4)	87.2(2)	8.03439(7)	0.2548(2)
1	950	1050(180)	0.208(4)	86.90(4)	8.03308(7)	0.2546(2)
1	1000	391(51)	0.232(8)	80.0(5)	8.0284(1)	0.2538(3)
1	1100	47(6)	.99(7)	70(1)	7.9673(5)	0.2511(5)
0.75	-	500(14)	0.080(1)	97.5(1)	8.05544(2)	0.25721(8)
0.75	650	450(11)	0.084(1)	96.4(1)	8.05544(2)	0.25768(8)
0.75	700	395(11)	0.087(2)	97.9(1)	8.05593(3)	0.25704(9)
0.75	750	480(14)	0.095(1)	95.9(1)	8.05533(2)	0.25743(7)
0.75	800	560(16)	0.124(1)	96.27(5)	8.05421(2)	0.25732(8)
0.75	800	471(17)	0.146(2)	94.93(7)	8.05429(3)	0.25732(8)
0.75	850	780(100)	0.248(4)	90.9(2)	8.05033(8)	0.2577(1)
0.75	900	2000(1400)	0.46(1)	86.6(4)	8.0390(2)	0.2576(2)
0.75	950	1400(930)	0.63(1)	76.8(4)	8.0070(2)	0.2566(2)
0.75	950	490(94)	0.54(1)	77.5(3)	8.0102(2)	0.2563(2)
0.75	1000	430(74)	0.33(1)	70.9(4)	8.0006(2)	0.2567(2)
0.75	1100	400(45)	0.220(7)	71.9(4)	7.9992(1)	0.2566(2)

## Spinel - continued

x	Reduction Temperature (°C)	Crystallite Size (nm)	Microstrain	Refined Weight %	a (Å)	Oxygen Positional Parameter
0.5	-	540(20)	0.100(2)	97.5(3)	8.06550(3)	0.25874(8)
0.5	650	500(15)	0.091(2)	97.1(1)	8.06536(3)	0.25869(8)
0.5	700	500(15)	0.092(2)	96.4(2)	8.06578(3)	0.25855(8)
0.5	750	460(15)	0.095(2)	95.0(3)	8.06589(3)	0.25873(8)
0.5	800	450(13)	0.096(2)	95.9(1)	8.06464(3)	0.25879(8)
0.5	800	485(17)	0.097(2)	97.24(7)	8.06583(3)	0.25860(8)
0.5	850	450(12)	0.113(1)	96.6(6)	8.06403(3)	0.25895(6)
0.5	900	770(60)	0.193(2)	94.26(9)	8.06039(5)	0.25887(8)
0.5	950	2000(1000)	0.376(6)	87.4(2)	8.0353(1)	0.2592(1)
0.5	950	2000(740)	0.308(5)	89.2(2)	8.04246(9)	0.2592(1)
0.5	1000	1200(200)	0.251(4)	84.7(2)	8.02535(7)	0.2598(1)
0.5	1100	950(120)	0.207(3)	85.9(1)	8.02975(6)	0.25907(9)
0.25	-	250(5)	0.041(2)	97.77(6)	8.07633(3)	0.26125(8)
0.25	650	290(6)	0.052(1)	97.39(6)	8.07646(3)	0.26103(8)
0.25	700	325(7)	0.058(1)	97.79(5)	8.07637(3)	0.26107(7)
0.25	750	320(7)	0.055(1)	97.79(5)	8.07617(3)	0.26092(7)
0.25	800	300(6)	0.059(2)	97.49(6)	8.07441(3)	0.26068(7)
0.25	800	240(5)	0.054(2)	97.53(6)	8.07582(3)	0.26087(8)
0.25	850	350(8)	0.084(1)	96.40(5)	8.07333(3)	0.26083(6)
0.25	900	430(15)	0.121(2)	95.48(5)	8.07160(4)	0.26079(7)
0.25	950	550(35)	0.151(3)	93.90(6)	8.06478(6)	0.26116(9)
0.25	950	380(14)	0.106(2)	95.70(6)	8.07027(4)	0.26091(9)
0.25	1000	240(5)	0.066(2)	94.27(6)	8.06450(4)	0.26096(8)
0.25	1100	280(6)	0.046(2)	95.10(6)	8.0680(3)	0.26104(8)
0	-	630(32)	0.111(2)	97.66(4)	8.08309(3)	0.26255(7)

## Nickel

x	Reduction Temperature (°C)	Crystallite Size (nm)	Microstrain	Refined Weight %	a (Å)
1	650	93(105)	0.03(30)	0.47(5)	3.5260(5)
1	700	62(46)	0.04(26)	0.58(5)	3.5259(5)
1	750	59(27)	0.07(17)	1.00(5)	3.5263(3)
1	800	154(122)	0.24(12)	2.00(5)	3.5275(2)
1	800	99(33)	0.11(8)	2.91(6)	3.5282(1)
1	850	108(83)	0.13(7)	4.42(7)	3.5283(1)
1	900	127(31)	0.10(5)	6.8(1)	3.52879(8)
1	950	176(40)	0.07(3)	11.1(2)	3.52924(6)
1	950	131(24)	0.06(3)	11.5(2)	3.52993(6)
1	1000	218(57)	0.07(3)	18.4(5)	3.52989(7)
1	1100	1600(2200)	0.12(2)	28(1)	3.5302(2)
0.75	650	2000(650000)	0(4)	1.4(1)	3.536(6)
0.75	700	150(121000)	1(126)	0.006(90)	3.5(2)
0.75	750	2000(260000)	0(2)	1.8(1)	3.718(3)
0.75	800	57(14)	0.06(11)	1.58(4)	3.5291(2)
0.75	800	97(30)	0.17(7)	2.90(5)	3.5296(1)
0.75	850	190(70)	0.12(4)	6.5(1)	3.52909(8)
0.75	900	300(126)	0.13(3)	11.4(3)	3.52905(8)
0.75	950	2000(2400)	0.16(1)	21.2(3)	3.52959(7)
0.75	950	380(81)	0.11(1)	20.5(3)	3.53156(6)
0.75	1000	2000(2200)	0.14(1)	26.7(4)	3.53087(6)
0.75	1100	1100(590)	0.11(1)	25.9(3)	3.53112(5)

## Nickel – continued

x	Reduction Temperature (°C)	Crystallite Size (nm)	Microstrain	Refined Weight %	a (Å)
0.5	650	1800(770000)	0(5)	0.5(1)	3.631(8)
0.5	700	420(56000)	0(8)	1.3(1)	3.65(1)
0.5	750	700(84000)	0(4)	2.6(3)	3.598(5)
0.5	800	2000(50000)	0(3)	1.7(1)	3.660(4)
0.5	800	2000(280000)	0(2)	0.42(5)	3.557(3)
0.5	850	400(1000)	0.2(1)	1.12(4)	3.5283(2)
0.5	900	500(390)	0.13(4)	3.43(5)	3.52859(7)
0.5	950	120(1400)	0.15(2)	10.1(2)	3.52897(6)
0.5	950	800(730)	0.16(3)	8.4(1)	3.52995(6)
0.5	1000	2000(2800)	0.14(2)	12.8(1)	3.52863(3)
0.5	1100	400(100)	0.09(1)	11.8(1)	3.52913(4)
0.25	650	1900(1000000)	0.4(6.0)	0.03(3)	3.399(8)
0.25	700	2000(60000)	0.05(30)	0.07(2)	3.5124(6)
0.25	750	2000(71000)	0.08(38)	0.09(2)	3.5128(7)
0.25	800	2000(100000)	0.49(57)	0.38(4)	3.5229(9)
0.25	800	1800(90000)	0.54(65)	0.34(4)	3.526(1)
0.25	850	140(73)	0.21(8)	1.39(3)	3.5266(2)
0.25	900	170(63)	0.20(5)	2.29(3)	3.5271(1)
0.25	950	385(300)	0.28(4)	3.83(4)	3.52696(9)
0.25	950	210(140)	0.26(7)	2.16(4)	3.5279(1)
0.25	1000	500(500)	0.27(4)	3.51(4)	3.52640(8)
0.25	1100	380(250)	0.18(4)	2.76(3)	3.52630(7)

## Baddeleyite

x	Reduction Temperature (°C)	Refined Weight %	a (Å)	b (Å)	c (Å)	$\beta$ (°)
1	-	1.34(4)	5.149(1)	5.212(1)	5.318(1)	99.13(1)
1	650	1.48(5)	5.151(2)	5.213(2)	5.317(1)	99.14(2)
1	700	1.46(4)	5.153(1)	5.210(1)	5.318(1)	99.16(1)
1	750	1.50(4)	5.153(1)	5.208(1)	5.320(1)	99.18(1)
1	800	1.50(4)	5.152(9)	5.206(1)	5.3218(9)	99.20(1)
1	800	1.75(5)	5.151(1)	5.207(1)	5.3232(9)	99.25(1)
1	850	1.65(5)	5.154(1)	5.197(1)	5.326(1)	99.30(1)
1	900	1.54(6)	5.152(1)	5.204(2)	5.327(1)	99.19(1)
1	950	1.53(6)	5.152(1)	5.201(1)	5.328(1)	99.19(1)
1	950	1.54(6)	5.150(1)	5.200(2)	5.330(1)	99.19(1)
1	1000	1.40(9)	5.148(3)	5.134(2)	5.405(2)	99.37(2)
1	1100	1.8(1)	5.146(2)	5.131(3)	5.405(3)	99.37(2)
0.75	-	2.06(5)	5.150(1)	5.217(1)	5.317(1)	99.09(1)
0.75	650	2.04(5)	5.152(1)	5.216(1)	5.318(1)	99.10(1)
0.75	700	1.86(5)	5.151(1)	5.218(1)	5.318(1)	99.12(1)
0.75	750	2.07(4)	5.1529(9)	5.213(1)	5.3188(8)	99.128(9)
0.75	800	1.98(3)	5.1539(6)	5.205(7)	5.3208(6)	99.241(7)
0.75	800	2.16(4)	5.1543(7)	5.2027(8)	5.3227(7)	99.328(8)
0.75	850	2.31(7)	5.150(1)	5.195(1)	5.323(1)	99.50(1)
0.75	900	2.0(1)	5.139(2)	5.190(2)	5.323(2)	99.61(2)
0.75	950	1.85(6)	5.150(1)	5.204(1)	5.317(1)	99.22(1)
0.75	950	1.90(6)	5.1514(9)	5.205(1)	5.3194(9)	99.23(1)
0.75	1000	2.08(6)	5.150(1)	5.203(1)	5.321(1)	99.27(1)
0.75	1100	1.90(6)	5.150(1)	5.204(1)	5.322(1)	99.27(1)

## Baddeleyite - continued

x	Reduction Temperature (°C)	Refined Weight %	a (Å)	b (Å)	c (Å)	β (°)
0.5	-	2.08(5)	5.151(1)	5.218(2)	5.318(1)	99.04(1)
0.5	650	2.17(5)	5.152(1)	5.216(1)	5.320(1)	99.10(1)
0.5	700	2.06(5)	5.151(1)	5.221(1)	5.319(1)	99.05(1)
0.5	750	2.07(5)	5.153(1)	5.219(1)	5.319(1)	99.06(1)
0.5	800	2.13(5)	5.153(1)	5.215(1)	5.320(1)	99.08(1)
0.5	800	2.09(5)	5.152(1)	5.215(1)	5.3205(9)	99.10(1)
0.5	850	2.12(4)	5.1532(8)	5.2103(9)	5.3196(7)	99.180(9)
0.5	900	2.11(5)	5.1557(8)	5.2037(9)	5.3208(8)	99.304(9)
0.5	950	2.16(6)	5.155(1)	5.197(1)	5.319(1)	99.39(1)
0.5	950	2.15(6)	5.1542(9)	5.201(1)	5.3191(9)	99.35(1)
0.5	1000	2.18(5)	5.1561(9)	5.201(1)	5.3190(9)	99.23(1)
0.5	1100	2.03(4)	5.1561(9)	5.205(1)	5.3191(9)	99.18(1)
0.25	-	1.68(5)	5.152(2)	5.205(3)	5.322(2)	99.06(2)
0.25	650	1.47(5)	5.152(2)	5.205(2)	5.322(2)	99.10(2)
0.25	700	1.53(4)	5.152(1)	5.205(2)	5.322(2)	99.16(2)
0.25	750	1.47(4)	5.152(2)	5.203(2)	5.322(2)	99.14(2)
0.25	800	1.35(4)	5.153(2)	5.203(2)	5.321(2)	99.12(2)
0.25	800	1.44(4)	5.149(2)	5.218(2)	5.321(2)	99.07(2)
0.25	850	1.40(3)	5.153(2)	5.206(2)	5.321(1)	99.11(2)
0.25	900	1.44(4)	5.152(2)	5.209(2)	5.322(1)	99.11(2)
0.25	950	1.54(5)	5.151(2)	5.209(2)	5.321(2)	99.05(2)
0.25	950	1.38(5)	5.144(2)	5.228(2)	5.319(2)	98.99(2)
0.25	1000	1.42(4)	5.153(2)	5.206(2)	5.323(2)	99.03(2)
0.25	1100	1.35(4)	5.154(2)	5.205(2)	5.323(2)	99.06(2)
0	-	1.25(3)	5.150(2)	5.213(2)	5.323(2)	99.08(2)

## Tetragonal ZrO<sub>2</sub>

x	Reduction Temperature (°C)	Refined Weight %	a (Å)	c (Å)
1	-	0.28(2)	3.5988(9)	5.196(2)
1	650	0.22(2)	3.599(1)	5.197(3)
1	700	0.23(2)	3.5994(7)	5.192(2)
1	750	0.20(2)	3.601(1)	5.192(3)
1	800	0.25(2)	3.599(1)	5.196(3)
1	800	0.06(2)	3.601(3)	5.201(8)
1	850	0.14(2)	3.595(2)	5.211(4)
1	900	0.16(2)	3.595(2)	5.206(5)
1	950	0.16(3)	3.581(2)	5.239(6)
1	950	0.10(3)	3.580(3)	5.240(7)
1	1000	0.21(4)	3.594(1)	5.202(3)
1	1100	0.23(5)	3.607(3)	5.177(7)
0.75	-	0.18(2)	3.599(1)	5.187(3)
0.75	650	0.18(2)	3.597(1)	5.192(4)
0.75	700	0.26(2)	3.5987(8)	5.185(2)
0.75	750	0.24(2)	3.5977(9)	5.190(2)
0.75	800	0.16(1)	3.600(1)	5.184(3)
0.75	800	0.00(2)	-	-
0.75	850	0.20(3)	3.595(1)	5.212(4)
0.75	900	0.07(3)	3.594(5)	5.22(1)
0.75	950	0.08(2)	3.630(4)	5.089(9)
0.75	950	0.13(2)	3.631(3)	5.090(7)
0.75	1000	0.23(3)	3.597(2)	5.188(6)
0.75	1100	0.19(3)	3.551(3)	5.34(1)

## Tetragonal ZrO<sub>2</sub> - continued

x	Reduction Temperature (°C)	Refined Weight %	a (Å)	c (Å)
0.5	-	0.20(2)	3.598(1)	5.188(3)
0.5	650	0.25(2)	3.598(1)	5.188(3)
0.5	700	0.19(2)	3.598(1)	5.188(4)
0.5	750	0.22(2)	3.598(1)	5.188(3)
0.5	800	0.31(2)	3.5979(8)	5.188(2)
0.5	800	0.24(2)	3.5971(8)	5.190(2)
0.5	850	0.15(1)	3.599(1)	5.186(4)
0.5	900	0.19(2)	3.616(2)	5.138(6)
0.5	950	0.22(3)	3.611(2)	5.156(5)
0.5	950	0.22(2)	3.612(1)	5.155(3)
0.5	1000	0.31(2)	3.634(2)	5.089(4)
0.5	1100	0.24(2)	3.618(1)	5.140(3)
0.25	-	0.83(2)	3.638(1)	5.083(2)
0.25	650	0.68(2)	3.6363(9)	5.083(2)
0.25	700	0.61(2)	3.6361(9)	5.082(2)
0.25	750	0.65(2)	3.6360(9)	5.082(2)
0.25	800	0.78(2)	3.6361(9)	5.082(2)
0.25	800	0.68(2)	3.5994(4)	5.186(1)
0.25	850	0.80(2)	3.6367(5)	5.083(1)
0.25	900	0.78(2)	3.6366(6)	5.082(1)
0.25	950	0.72(2)	3.6397(9)	5.072(2)
0.25	950	0.76(2)	3.5986(3)	5.1890(9)
0.25	1000	0.79(2)	3.6386(8)	5.076(2)
0.25	1100	0.79(2)	3.6392(8)	5.079(2)
0	-	1.09(2)	3.6017(3)	5.1803(8)

## APPENDIX 2 - REMNANT SPINEL COMPOSITIONS USED IN FIGURE 59

Remnant Spinel Composition in Terms of Formula Unit

Reduction Temperature (°C)	NiAl <sub>2</sub> O <sub>4</sub> + ZrO <sub>2</sub>			Ni <sub>0.75</sub> Mg <sub>0.25</sub> Al <sub>2</sub> O <sub>4</sub> + ZrO <sub>2</sub>				Ni <sub>0.5</sub> Mg <sub>0.5</sub> Al <sub>2</sub> O <sub>4</sub> + ZrO <sub>2</sub>				Ni <sub>0.25</sub> Mg <sub>0.75</sub> Al <sub>2</sub> O <sub>4</sub> + ZrO <sub>2</sub>			
	Weight % Nickel	Ni	Al	Weight % Nickel	Ni	Mg	Al	Weight % Nickel	Ni	Mg	Al	Weight % Nickel	Ni	Mg	Al
30	0.12	1.00	2.00	0.27	0.74	0.25	2.00	0.18	0.49	0.50	2.00	0.10	0.25	0.75	2.00
650	0.47	0.99	2.01	1.43	0.72	0.25	2.02	0.50	0.49	0.50	2.01	0.03	0.25	0.75	2.00
700	0.58	0.99	2.01	0.01	0.75	0.25	2.00	1.34	0.47	0.50	2.02	0.07	0.25	0.75	2.00
750	1.00	0.98	2.02	1.76	0.71	0.25	2.03	2.68	0.43	0.51	2.04	0.09	0.25	0.75	2.00
800	2.01	0.95	2.03	1.59	0.71	0.25	2.02	1.67	0.46	0.51	2.02	0.38	0.24	0.75	2.01
800	2.91	0.93	2.05	2.90	0.68	0.26	2.04	0.42	0.49	0.50	2.01	0.34	0.24	0.75	2.00
850	4.42	0.89	2.07	6.50	0.59	0.26	2.10	1.12	0.47	0.50	2.02	1.39	0.22	0.76	2.02
900	6.85	0.83	2.11	11.41	0.46	0.27	2.18	3.43	0.41	0.51	2.05	2.29	0.19	0.76	2.03
950	11.15	0.73	2.18	21.23	0.18	0.29	2.35	10.18	0.23	0.54	2.15	3.83	0.15	0.77	2.05
950	11.46	0.72	2.19	20.50	0.20	0.29	2.34	8.42	0.28	0.53	2.12	2.16	0.20	0.76	2.03
1000	18.39	0.53	2.32	26.75	0.01	0.31	2.46	12.82	0.16	0.55	2.20	3.51	0.16	0.77	2.05
1100	27.89	0.23	2.51	25.93	0.03	0.31	2.44	11.76	0.19	0.54	2.18	2.76	0.18	0.76	2.04
TGA - 1000	33.12	0.06	2.63	26.28	0.02	0.31	2.45	18.20	0.00	0.57	2.28	9.13	0.02	0.80	2.12

Remnant Spinel Composition in Mole Percent

Reduction Temperature (°C)	NiAl <sub>2</sub> O <sub>4</sub> + ZrO <sub>2</sub>			Ni <sub>0.75</sub> Mg <sub>0.25</sub> Al <sub>2</sub> O <sub>4</sub> + ZrO <sub>2</sub>				Ni <sub>0.5</sub> Mg <sub>0.5</sub> Al <sub>2</sub> O <sub>4</sub> + ZrO <sub>2</sub>				Ni <sub>0.25</sub> Mg <sub>0.75</sub> Al <sub>2</sub> O <sub>4</sub> + ZrO <sub>2</sub>			
	Weight % Nickel	Ni	Al	Weight % Nickel	Ni	Mg	Al	Weight % Nickel	Ni	Mg	Al	Weight % Nickel	Ni	Mg	Al
30	0.12	0.33	0.67	0.27	0.25	0.08	0.67	0.18	0.16	0.17	0.67	0.10	0.08	0.25	0.67
650	0.47	0.33	0.67	1.43	0.24	0.08	0.68	0.50	0.16	0.17	0.67	0.03	0.08	0.25	0.67
700	0.58	0.33	0.67	0.01	0.25	0.08	0.67	1.34	0.16	0.17	0.68	0.07	0.08	0.25	0.67
750	1.00	0.33	0.67	1.76	0.24	0.08	0.68	2.68	0.15	0.17	0.68	0.09	0.08	0.25	0.67
800	2.01	0.32	0.68	1.59	0.24	0.08	0.68	1.67	0.15	0.17	0.68	0.38	0.08	0.25	0.67
800	2.91	0.31	0.69	2.90	0.23	0.09	0.69	0.42	0.16	0.17	0.67	0.34	0.08	0.25	0.67
850	4.42	0.30	0.70	6.50	0.20	0.09	0.71	1.12	0.16	0.17	0.67	1.39	0.07	0.25	0.67
900	6.85	0.28	0.72	11.41	0.16	0.09	0.75	3.43	0.14	0.17	0.69	2.29	0.06	0.26	0.68
950	11.15	0.25	0.75	21.23	0.06	0.10	0.83	10.18	0.08	0.18	0.74	3.83	0.05	0.26	0.69
950	11.46	0.25	0.75	20.50	0.07	0.10	0.83	8.42	0.10	0.18	0.72	2.16	0.07	0.25	0.68
1000	18.39	0.19	0.81	26.75	0.00	0.11	0.89	12.82	0.05	0.19	0.76	3.51	0.05	0.26	0.69
1100	27.89	0.08	0.92	25.93	0.01	0.11	0.88	11.76	0.06	0.19	0.75	2.76	0.06	0.26	0.68
TGA - 1000	33.12	0.02	0.98	26.28	0.01	0.11	0.88	18.20	0.00	0.20	0.80	9.13	0.01	0.27	0.72